

Jordan Journal of P H Y S I C S

An International Peer-Reviewed Research Journal

Volume 12, No. 3, December 2019, Jumada 1 1441 H

Jordan Journal of Physics (JJP): An International Peer-Reviewed Research Journal funded by the Scientific Research Support Fund, Jordan, and published biannually by the Deanship of Research and Graduate Studies, Yarmouk University, Irbid, Jordan.

EDITOR-IN-CHIEF:

Ibrahim O. Abu Al-Jarayesh

Department of Physics, Yarmouk University, Irbid, Jordan.

ijaraysh@yu.edu.jo

EDITORIAL BOARD:	ASSOCIATE EDITORIAL BOARD
<p>Prof. Nabil Y. Ayoub <i>President, American University of Madaba, Madaba, Jordan.</i> nabil.ayoub@gju.edu.jo</p> <p>Prof. Jamil M. Khalifeh <i>Department of Physics, University of Jordan, Amman, Jordan.</i> jkalifa@ju.edu.jo</p> <p>Prof. Sami H. Mahmood <i>Department of Physics, University of Jordan, Amman, Jordan.</i> s.mahmood@ju.edu.jo</p> <p>Prof. Marwan S. Mousa <i>Department of Physics, Mu'tah University, Al-Karak, Jordan.</i> mmousa@mutah.edu.jo</p> <p>Prof. Mohammad Al-Sugheir <i>Department of Physics, The Hashemite University, Zarqa, Jordan.</i> msugh@hu.edu.jo</p> <p>Prof. Abdalmajeid M. Alyassin <i>Department of Physics, Yarmouk University, Irbid, Jordan.</i> alyassin@yu.edu.jo</p> <p>Prof. M-Ali H. Al-Akhras (AL-Omari) <i>Department of Physics, Jordan University of Science & Technology, Irbid, Jordan.</i> alakhmoh@just.edu.jo</p> <p>Prof. Ibrahim A. Bsoul <i>Department of Physics, Al al-Bayt University, Mafraq, Jordan.</i> Ibrahimbsoul@yahoo.com</p>	<p>Prof. Mark Haggmann <i>Desert Electronics Research Corporation, 762 Lacey Way, North Salt Lake 84064, Utah, U. S. A.</i> MHaggmann@NewPathResearch.Com</p> <p>Dr. Richard G. Forbes <i>Dept. of Electrical and Electronic Engineering, University of Surrey, Advanced Technology Institute and Guildford, Surrey GU2 7XH, UK.</i> r.forbes@surrey.ac.uk</p> <p>Prof. Roy Chantrell <i>Physics Department, The University of York, York, YO10 5DD, UK.</i> roy.chantrell@york.ac.uk</p> <p>Prof. Susamu Taketomi <i>2-35-8 Higashisakamoto, Kagoshima City, 892-0861, Japan.</i> staketomi@hotmail.com</p>

Editorial Secretary: Majdi Al-Shannaq.

Languages Editor: Haider Al-Momani

Manuscripts should be submitted to:

Prof. Ibrahim O. Abu Al-Jarayesh
Editor-in-Chief, Jordan Journal of Physics
Deanship of Research and Graduate Studies
Yarmouk University-Irbid-Jordan
Tel. 00 962 2 7211111 Ext. 2075
E-mail: jjp@yu.edu.jo
Website: <http://Journals.yu.edu.jo/jjp>

Jordan Journal of PHYSICS

An International Peer-Reviewed Research Journal

Volume 12, No. 3, December 2019, Jumada 1 1441 H

INTERNATIONAL ADVISORY BOARD

Prof. Dr. Ahmad Saleh

Department of Physics, Yarmouk University, Irbid, Jordan.
salema@yu.edu.jo

Prof. Dr. Aurore Savoy-Navarro

LPNHE Université de Paris 6/IN2P3-CNRS, Tour 33, RdC 4,
Place Jussieu, F 75252, Paris Cedex 05, France.
auore@lfnhep.in2p3.fr

Prof. Dr. Bernard Barbara

Laboratoire Louis Neel, Salle/Room: D 108, 25, Avenue des
Martyrs BP 166, 38042-Grenoble Cedex 9, France.
Barbara@grenoble.cnrs.fr

Prof. Dr. Bruno Guiderdoni

Observatoire Astronomique de Lyon, g, avenue Ch. Antre-F-69561,
Saint Genis Laval Cedex, France.
Bruno.guiderdoni@olos.univ-lyon1.fr

Prof. Dr. Buford Price

Physics Department, University of California, Berkeley, CA 94720,
U. S. A.
bprice@berkeley.edu

Prof. Dr. Colin Cough

School of Physics and Astronomy, University of Birmingham, B15
2TT, U. K.
c.gough@bham.ac.uk

Prof. Dr. Desmond Cook

Department of Physics, Condensed Matter and Materials Physics
Research Group, Old Dominion University, Norfolk, Virginia
23529, U. S. A.
Dcook@physics.odu.edu

Prof. Dr. Evgeny Sheshin

MIPT, Institutskij per. 9, Dogoprudnyi 141700, Russia.
sheshin@lafeet.mipt.ru

Prof. Dr. Hans Ott

Laboratorium fuer Festkorperphysik, ETH Honggerberg, CH-
8093 Zurich, Switzerland.
ott@solid.phys.ethz.ch

Prof. Dr. Herwig Schopper

President SESAME Council, Chairman Scientific Board UNESCO
IBSP Programme, CERN, 1211 Geneva, Switzerland.
Herwig.Schopper@cern.ch

Prof. Dr. Humam Ghassib

Department of Physics, The University of Jordan, Amman 11942,
Jordan.
humamg@ju.edu.jo

Prof. Dr. Khalid Tougan

Chairman of Jordan Atomic Energy Commission, Amman, Jordan.

Prof. Dr. Nasr Zubeidev

President: Al-Zaytoonah University of Jordan, Amman, Jordan.
President@alzaytoonah.edu.jo

Prof. Dr. Patrick Roudeau

Laboratoire de l'Accelérateur, Lineaire (LAL), Université Paris-
Sud 11, Batiment 200, 91898 Orsay Cedex, France.
roudeau@mail.cern.ch

Prof. Dr. Paul Chu

Department of Physics, University of Houston, Houston, Texas
77204-5005, U. S. A.
Ching-Wu.Chu@mail.uh.edu

Prof. Dr. Peter Dowben

Nebraska Center for Materials and Nanoscience, Department of
Physics and Astronomy, 255 Behlen Laboratory (10th and R
Streets), 116 Brace Lab., P. O. Box 880111, Lincoln, NE 68588-
0111, U. S. A.
pdowben@unl.edu

Prof. Dr. Peter Mulser

Institute fuer Physik, T.U. Darmstadt, Hochschulstr. 4a, 64289
Darmstadt, Germany.
Peter.mulser@physik.tu-darmstadt.de

Prof. Dr. Rasheed Azzam

Department of Electrical Engineering, University of New Orleans
New Orleans, Louisiana 70148, U. S. A.
razzam@uno.edu

Prof. Dr. Shawqi Al-Dallal

Department of Physics, Faculty of Science, University of Bahrain,
Manamah, Kingdom of Bahrain.

Prof. Dr. Wolfgang Nolting

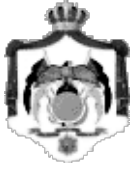
Institute of Physics / Chair: Solid State Theory, Humboldt-
University at Berlin, Newtonstr. 15 D-12489 Berlin, Germany
Wolfgang.nolting@physik.hu-berlin.de

Prof. Dr. Ingo Hofmann

GSI Darmstadt, Planckstr. 1, 64291, Darmstadt, Germany.
i.hofmann@gsi.de

Prof. Dr. Jozef Lipka

Department of Nuclear Physics and Technology, Slovak University
of Technology, Bratislava, Ilkovicova 3, 812 19 Bratislava,
Slovakia.
Lipka@elf.stuba.sk



The Hashemite Kingdom of Jordan



Yarmouk University

Jordan Journal of
PHYSICS

An International Peer-Reviewed Research Journal
Funded by the Scientific Research Support Fund

Volume 12, No. 3, December 2019, Jumada 1 1441 H

Instructions to Authors

Instructions to authors concerning manuscript organization and format apply to hardcopy submission by mail, and also to electronic online submission via the Journal homepage website (<http://jjp.yu.edu.jo>).

Manuscript Submission

1- **E-mail to** : jjp@yu.edu.jo

2- **Online**: Follow the instructions at the journal homepage website.

Original *Research Articles*, *Communications* and *Technical Notes* are subject to critical review by minimum of two competent referees. Authors are encouraged to suggest names of competent reviewers. *Feature Articles* in active Physics research fields, in which the author's own contribution and its relationship to other work in the field constitute the main body of the article, appear as a result of an invitation from the Editorial Board, and will be so designated. The author of a *Feature Article* will be asked to provide a clear, concise and critical status report of the field as an introduction to the article. *Review Articles* on active and rapidly changing Physics research fields will also be published. Authors of *Review Articles* are encouraged to submit two-page proposals to the Editor-in-Chief for approval. Manuscripts submitted in *Arabic* should be accompanied by an Abstract and Keywords in English.

Organization of the Manuscript

Manuscripts should be typed double spaced on one side of A4 sheets (21.6 x 27.9 cm) with 3.71 cm margins, using Microsoft Word 2000 or a later version thereof. The author should adhere to the following order of presentation: Article Title, Author(s), Full Address and E-mail, Abstract, PACS and Keywords, Main Text, Acknowledgment. Only the first letters of words in the Title, Headings and Subheadings are capitalized. Headings should be in **bold** while subheadings in *italic* fonts.

Title Page: Includes the title of the article, authors' first names, middle initials and surnames and affiliations. The affiliation should comprise the department, institution (university or company), city, zip code and state and should be typed as a footnote to the author's name. The name and complete mailing address, telephone and fax numbers, and e-mail address of the author responsible for correspondence (designated with an asterisk) should also be included for official use. The title should be carefully, concisely and clearly constructed to highlight the emphasis and content of the manuscript, which is very important for information retrieval.

Abstract: A one paragraph abstract not exceeding 200 words is required, which should be arranged to highlight the purpose, methods used, results and major findings.

Keywords: A list of 4-6 keywords, which expresses the precise content of the manuscript for indexing purposes, should follow the abstract.

PACS: Authors should supply one or more relevant PACS-2006 classification codes, (available at <http://www.aip.org/pacs/pacs06/pacs06-toc.html>)

Introduction: Should present the purpose of the submitted work and its relationship to earlier work in the field, but it should not be an extensive review of the literature (e.g., should not exceed 1 ½ typed pages).

Experimental Methods: Should be sufficiently informative to allow competent reproduction of the experimental procedures presented; yet concise enough not to be repetitive of earlier published procedures.

Results: should present the results clearly and concisely.

Discussion: Should be concise and focus on the interpretation of the results.

Conclusion: Should be a brief account of the major findings of the study not exceeding one typed page.

Acknowledgments: Including those for grant and financial support if any, should be typed in one paragraph directly preceding the References.

References: References should be typed double spaced and numbered sequentially in the order in which they are cited in the text. References should be cited in the text by the appropriate Arabic numerals, enclosed in square brackets. Titles of journals are abbreviated according to list of scientific periodicals. The style and punctuation should conform to the following examples:

1. Journal Article:

- a) Heisenberg, W., Z. Phys. 49 (1928) 619.
- b) Bednorz, J. G. and Müller, K. A., Z. Phys. B64 (1986) 189
- c) Bardeen, J., Cooper, L.N. and Schrieffer, J. R., Phys. Rev. 106 (1957) 162.
- d) Asad, J. H., Hijjawi, R. S., Sakaji, A. and Khalifeh, J. M., Int. J. Theor. Phys. 44(4) (2005), 3977.

2. Books with Authors, but no Editors:

- a) Kittel, C., "Introduction to Solid State Physics", 8th Ed. (John Wiley and Sons, New York, 2005), chapter 16.
- b) Chikazumi, S., C. D. Graham, JR, "Physics of Ferromagnetism", 2nd Ed. (Oxford University Press, Oxford, 1997).

3. Books with Authors and Editors:

- a) Allen, P. B. "Dynamical Properties of Solids", Ed. (1), G. K. Horton and A. A. Maradudin (North-Holland, Amsterdam, 1980), p137.
- b) Chantrell, R. W. and O'Grady, K., "Magnetic Properties of Fine Particles" Eds. J. L. Dormann and D. Fiorani (North-Holland, Amsterdam, 1992), p103.

4. Technical Report:

Purcell, J. "The Superconducting Magnet System for the 12-Foot Bubble Chamber", report ANL/HEP6813, Argonne Natl. Lab., Argonne, III, (1968).

5. Patent:

Bigham, C. B., Schneider, H. R., US patent 3 925 676 (1975).

6. Thesis:

Mahmood, S. H., Ph.D. Thesis, Michigan State University, (1986), USA (Unpublished).

7. Conference or Symposium Proceedings:

Blandin, A. and Lederer, P. Proc. Intern. Conf. on Magnetism, Nottingham (1964), P.71.

8. Internet Source:

Should include authors' names (if any), title, internet website, URL, and date of access.

9. Prepublication online articles (already accepted for publication):

Should include authors' names (if any), title of digital database, database website, URL, and date of access.

For other types of referenced works, provide sufficient information to enable readers to access them.

Tables: Tables should be numbered with Arabic numerals and referred to by number in the Text (e.g., Table 1). Each table should be typed on a separate page with the legend above the table, while explanatory footnotes, which are indicated by superscript lowercase letters, should be typed below the table.

Illustrations: Figures, drawings, diagrams, charts and photographs are to be numbered in a consecutive series of Arabic numerals in the order in which they are cited in the text. Computer-generated illustrations and good-quality digital photographic prints are accepted. They should be black and white originals (not photocopies) provided on separate pages and identified with their corresponding numbers. Actual size graphics should be provided, which need no further manipulation, with lettering (Arial or Helvetica) not smaller than 8 points, lines no thinner than 0.5 point, and each of uniform density. All colors should be removed from graphics except for those graphics to be considered for publication in color. If graphics are to be submitted digitally, they should conform to the following minimum resolution requirements: 1200 dpi for black and white line art, 600 dpi for grayscale art, and 300 dpi for color art. All graphic files must be saved as TIFF images, and all illustrations must be submitted in the actual size at which they should appear in the journal. Note that good quality hardcopy original illustrations are required for both online and mail submissions of manuscripts.

Text Footnotes: The use of text footnotes is to be avoided. When their use is absolutely necessary, they should be typed at the bottom of the page to which they refer, and should be cited in the text by a superscript asterisk or multiples thereof. Place a line above the footnote, so that it is set off from the text.

Supplementary Material: Authors are encouraged to provide all supplementary materials that may facilitate the review process, including any detailed mathematical derivations that may not appear in whole in the manuscript.

Revised Manuscript and Computer Disks

Following the acceptance of a manuscript for publication and the incorporation of all required revisions, authors should submit an original and one more copy of the final disk containing the complete manuscript typed double spaced in Microsoft Word for Windows 2000 or a later version thereof. All graphic files must be saved as PDF, JPG, or TIFF images.

Allen, P.B., “.....”, in: Horton, G.K., and Muradudin, A. A., (eds.), “Dynamical.....”, (North.....), pp....

Reprints

Twenty (20) reprints free of charge are provided to the corresponding author. For orders of more reprints, a reprint order form and prices will be sent with the article proofs, which should be returned directly to the Editor for processing.

Copyright

Submission is an admission by the authors that the manuscript has neither been previously published nor is being considered for publication elsewhere. A statement transferring copyright from the authors to Yarmouk University is required before the manuscript can be accepted for publication. The necessary form for such transfer is supplied by the Editor-in-Chief. Reproduction of any part of the contents of a published work is forbidden without a written permission by the Editor-in-Chief.

Disclaimer

Opinions expressed in this Journal are those of the authors and neither necessarily reflects the opinions of the Editorial Board or the University, nor the policy of the Higher Scientific Research Committee or the Ministry of Higher Education and Scientific Research. The publisher shoulders no responsibility or liability whatsoever for the use or misuse of the information published by JJP.

Indexing

JJP is currently indexing in:

	Emerging Sources Citation Index (ESCI)	 ULRICHSWEB™ GLOBAL SERIALS DIRECTORY
---	---	--

Jordan Journal of
P H Y S I C S

An International Peer-Reviewed Research Journal

Volume 12, No. 3, December 2019, Jumada 1 1441 H

Table of Contents:

English Articles	Pages
Effect of Substrate Temperature on Optical Properties of Spray Pyrolytic Cadmium Sulphide Thin Films	191-200
I. S. Akinsola, A. B. Alabi, A. A. Ajayi, K. S. Adedayo and O. A. Babalola	
Density and Surface Tension of Propanol and Propanol-Water Mixtures Using Molecular Dynamic Simulations	201-207
K. A. Khasawneh , M. M. Al-Ali, R.M. Al-Salman, H. A. Abu-Ghazleh and A. A. Obeidat	
Simulation-Assisted Environment-Mapping Using Unidirectional Ultrasonic Pulses	209-221
M. Al-Shorman, M. Al-Kofahi and Q. I. Mohaidat	
The Collision-Induced Absorption Spectra of Hydrogen Complexes in the Second Overtone Band	223-236
M. Abu-Kharma, Mahmoud H. Saleh, Z. M. Elimat and W. J. Kadhem	
Estimation of Radionuclide Concentrations and Average Effective Dose from Some Selected Imported Foodstuff	237-240
A. B. Ogunremi and K. A. Adewoyin	
Study of Lattice Parameter and Nanoparticle Size in Lead Chalcogenides (PbX, X = S, Se & Te)	241-245
D. R. Adhikari, S. K. Adhikari and H. P. Lamichhane	
Magnetization and Magnetic Susceptibility of GaAs Quantum Dot with Gaussian Confinement in Applied Magnetic Field	247-254
M. Ali, M. Elsaid and A. Shaer	
JRTR, the First Research Reactor in Jordan: Results of Commissioning in Light of Safety Enhancement Following Fukushima-Daiichi Accident	255-268
Khalifeh AbuSaleem	
Discrimination of Aerosol Types over Nairobi, Skukuza and Ilorin Using AOD-AE Clusters	269-289
S. B. Sharafa, B. I. Tijjani, R. Aliyu, T. H. Darma, H. T. Sulu and M. M. Bube	

Effect of Substrate Temperature on Optical Properties of Spray Pyrolytic Cadmium Sulphide Thin Films

I. S. Akinsola^{a,b}, A. B. Alabi^a, A. A. Ajayi^c, K. S. Adedayo^d and O. A. Babalola^e

^a Department of Physical and Mathematical Sciences (Physics Unit), Crown-Hill University, Eiyenkorin, Ilorin, Nigeria.

^b Department Of Physics, University Of Ilorin, Ilorin, Nigeria.

^c Department of Mathematical and Physical Sciences, Afe Babalola University, Ekiti State, Nigeria.

^d Department of Physics, University of Maiduguri, Nigeria.

^e Sheda Science and Technology Complex, Abuja, Nigeria.

Received on: 9/10/2018;

Accepted on: 6/2/2019

Abstract: Cadmium sulphide (CdS) thin films were prepared by chemical spray pyrolysis technique on micro-slide glasses using cadmium acetate and thiourea as precursors. The substrate temperature was varied in the range of 250°C- 350°C. The prepared films were annealed at 500°C for 1hour. The effects of substrate temperature and annealing on the optical properties of the films were investigated. The films were characterized using UV-Visible Spectrophotometer. The absorption and transmission spectra revealed that the transmission increases with wavelength, while the absorbance reduces as the wavelength increases in the visible region. The optical band gaps of the films were found to be 2.26eV, 2.07eV and 1.88eV with deposition temperature of 250°C, 300°C and 350°C, respectively. It was observed that the refractive index of the thin film obtained reduces as the substrate temperature increases and that annealing reduces the refractive index of the cadmium sulphide thin film. These findings show that cadmium sulphide is one of the most promising materials to be used as a window layer in hetero-junction thin film solar cells. It is also of good interest for its applications in some optoelectronic devices, like photoresistor and photodiode.

Keywords: Cadmium sulphide, Spray pyrolysis, Thin film, Annealing, Optical properties.

Introduction

Cadmium sulphide (CdS) is known as a II-VI semiconductor compound with wide band gap; 2.42 eV at room temperature [1]. It has been used in making hetero-junction thin film solar cells. A layer of material having thickness of the order of a few nanometers is generally referred to as 'thin film' [2]. The use of thin film has been growing at an increasing rate because of its potential applications in various fields of science and technology. The deposition of CdS films has

been explored by different techniques: thermal evaporation, chemical bath deposition (CBD), molecular beam epitaxy and spray pyrolysis [3]. Spray pyrolysis technique gives opportunity to vary several deposition parameters; like flow rate, air pressure, substrate temperature, spray nozzle-to-substrate distance, ... etc. Structural and optical properties of CdS deposited by spray pyrolysis technique depend on the parameters of relative concentration of the reactants for

chemical reaction, thickness of the film, substrate temperature and even annealing [4].

Apart from the afore-mentioned merits of spray pyrolysis technique for depositing thin films, it was also reported that it is simple, faster and provides uniform deposition of thin films [5].

The investigation of the basic properties of CdS thin films is of paramount importance in understanding and developing modern CdS solar cells [6].

Other schemes for power generation *via* solar cells include thin film solar cells and multi-junction solar cells. Multi-junction solar cells, although more efficient, have higher fabrication cost. Polycrystalline thin film solar cells are among the important candidates for large-scale photovoltaic applications because of their low cost, high efficiency and stable performance.

The influence of substrate temperature and annealing on the properties of cadmium sulphide thin films prepared by spray pyrolysis technique is reported in this study.

Experimental Details

Cadmium sulphide (CdS) was synthesized using spray pyrolysis technique. 0.1M of cadmium acetate dihydrate [$\text{Cd}(\text{CH}_3\text{COO})_2 \cdot 2\text{H}_2\text{O}$] $\geq 98.0\%$ (Sigma-Aldrich product) and 0.1M of thiourea [NH_2CSNH_2] (Sigma-Aldrich) were used as source of cadmium and Sulphur, respectively. The precursors, having been mixed with distilled water of required volume, were

stirred by the magnetic stirrer (ARGO LAB M2-A). Micro-slide glasses were used as substrate for the thin films. The substrates were pre-cleaned with detergent and distilled water as well as with methanol in an ultrasonic cleaner (VWR ultrasonic cleaner).

The substrate temperatures were varied between 250°C and 350°C using the Proportional Integral Derivative (PID) temperature controller, in the interval of 50°C . The air pressure used was 2 bars and the distance between the nozzle and substrate was kept at 24 cm. The solution was sprayed at a rate of 10 mlmin^{-1} . The thickness of the films was calculated using weight difference method and it was in the range of $2.98\mu\text{m} - 3.39\mu\text{m}$ for the as-prepared films. The films were annealed in a furnace at 500°C for 1hour.

Results and Discussion

Transmittance and Absorption Spectra

The UV-Visible spectrophotometer was used for obtaining the optical properties of the cadmium sulphide (CdS) film produced. The chosen range is within that of the visible region of the electromagnetic spectra, which is about 400-800nm. This region is chosen because the application of the prepared thin film in solar cell is of major concern in this work.

The wavelength dependence of the optical transmittance spectra for the thin films at different substrate temperatures of 250°C , 300°C and 350°C are shown in Fig. 1.

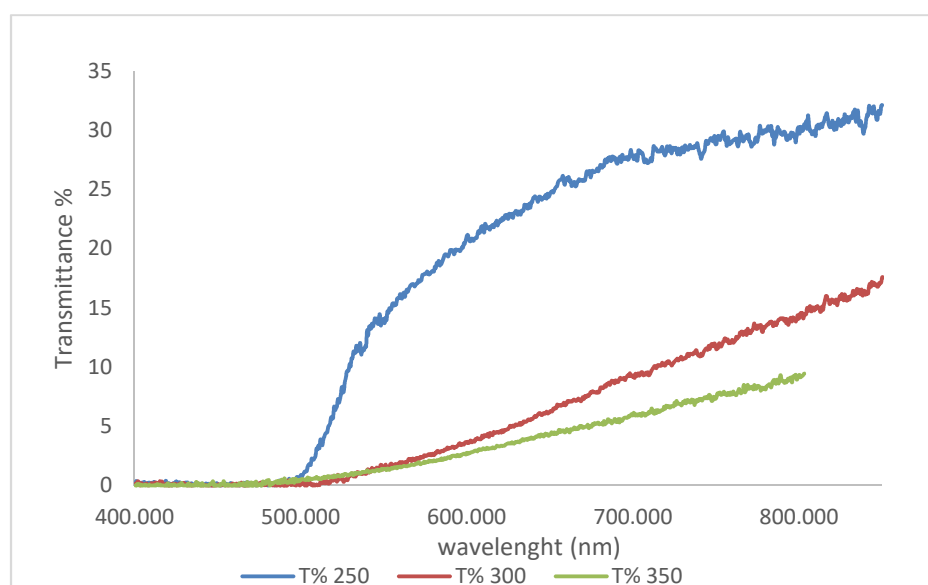


FIG. 1. Comparison of the variation in transmittance with wavelength for films sprayed at different substrate temperatures; 250°C , 300°C and 350°C .

It was observed that the transmission of visible light by the film increases as the wavelength increases in the visible region for all the films prepared at the different substrate temperatures stated above, though the transmission commenced at around 450 nm - 490 nm.

The percentage of transmission is a bit low when compared with what has been obtained by some researchers on cadmium sulphide thin film properties. This may be due to a little deviation of the composition of the material from the stoichiometric structure of the film or the thickness of the film. For a window layer in an hetero-junction thin film solar cell, the thickness of the material is expected to be very small (thinner than that of an absorber).

Figs. 2 and 3 show the comparison of the variation of transmittance with wavelength for the as-prepared films and those annealed at 500°C. From the comparison, it was observed that annealing improves the transmittance of the

films prepared at 300°C and 350°C, while it reduces the transmittance of the film prepared at 250°C, though annealed films transmit earlier in the visible region than as-prepared film, (Fig. 2). This effect of thermal annealing on the transmission of CdS films may be a result of some physical effects, such as structural and/or surface irregularity, and defect density, according to Hasnat and Podder, (2012). The heat treatment (annealing) is likely to have removed the defects present in the films prepared and thereby improved the crystallinity of the material which enhances more percentage of the visible light to be transmitted through the material.

Also, it was observed that the material prepared is sensitive to electromagnetic wave near infrared region (wavelength range of 700nm – 1mm). This makes it a potential material for use as a sensor in remote control devices, likewise in a light dependent resistor (LDR) and photodiode.

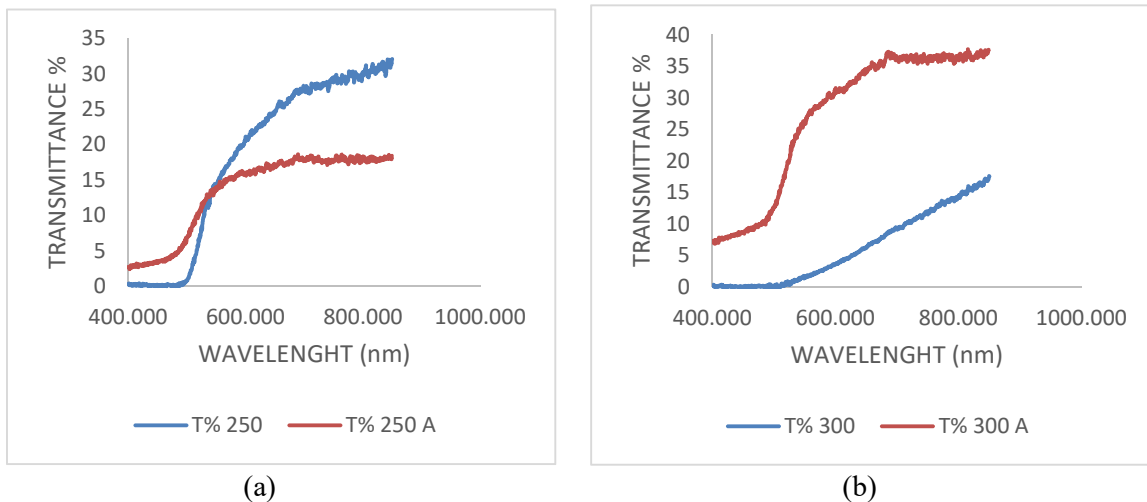


FIG. 2. Transmittance spectra of the as-prepared film at (a) 250°C and (b) 300°C, annealed at 500°C.

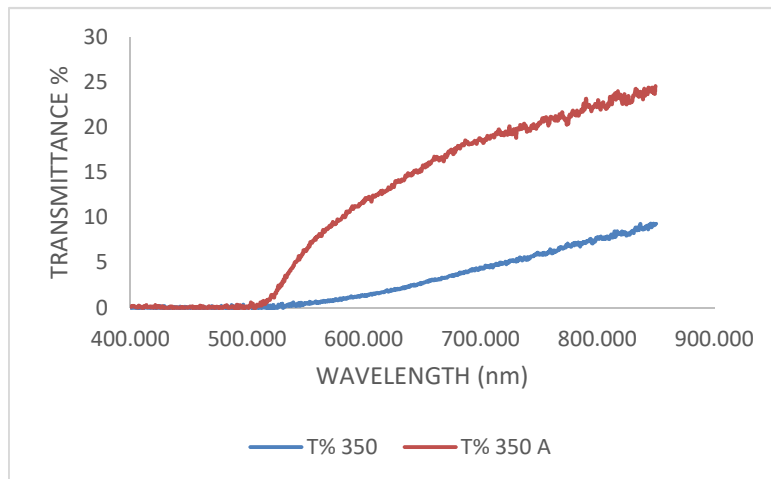


FIG. 3. Transmittance spectra of the as-prepared film at 350°C and annealed at 500°C.

The absorbance of the films deposited at the different temperatures mentioned earlier was also studied. The Absorbance A was obtained from the expression, $A = 2 - [\text{Log}\%T]$, where 'T' is the transmittance value. The result in Fig. 4 shows that the absorbance of visible light by the films reduces with increase in wavelength, though the absorption was observed till around 450nm; the absorption peak, before the fall commenced. When the films were treated with

heat (annealed) at 500°C, the absorbance decreases with increase in substrate temperature. Invariably, annealing reduces the optical absorbance of the film. This may be due to the fact that annealing removes likely defect that might be present in the film produced initially. Hence, it improves the property of the film for better application as a window layer in a thin film solar cell.

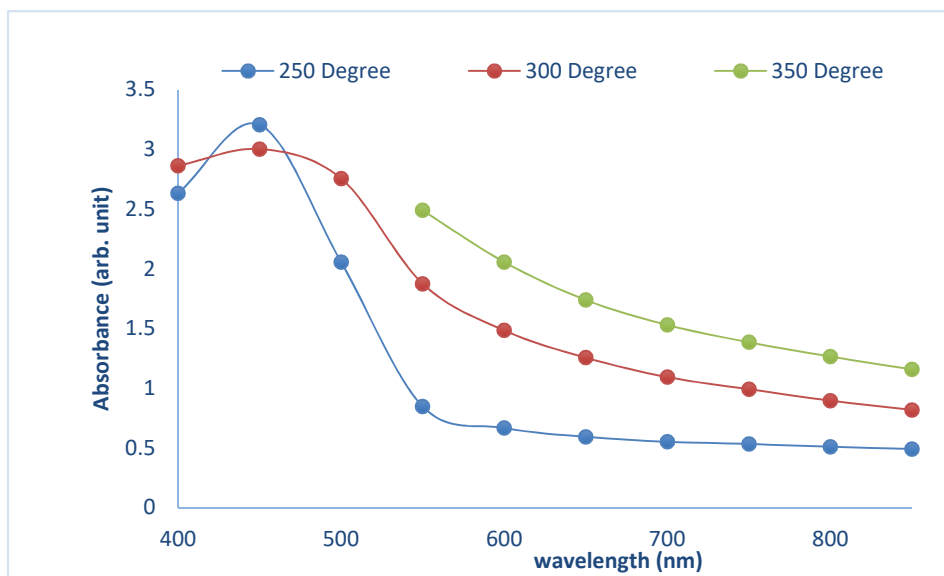


FIG. 4. Comparison of the variation of absorbance with wavelength for films sprayed at different substrate temperatures; 250°C, 300°C and 350°C.

Figs. 5, 6 and 7 show the comparison of the variation of the absorbance with wavelength for as-deposited film and the annealed films at 500°C.

It has been known that cadmium sulphide is a good window layer in a solar cell, which connotes that the absorbance will be low, with a reasonably high transmittance as compared with its absorbance in the visible region. The results shown in Figs. 1 - 4 confirmed this fact.

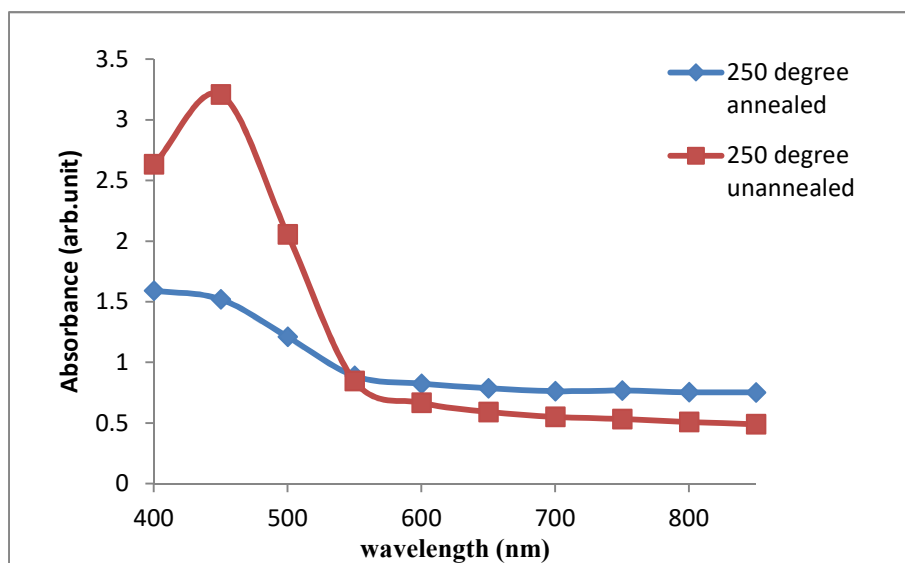


FIG. 5. Comparison of the variation of absorbance with wavelength for films sprayed at 250°C with the one annealed at 500°C.

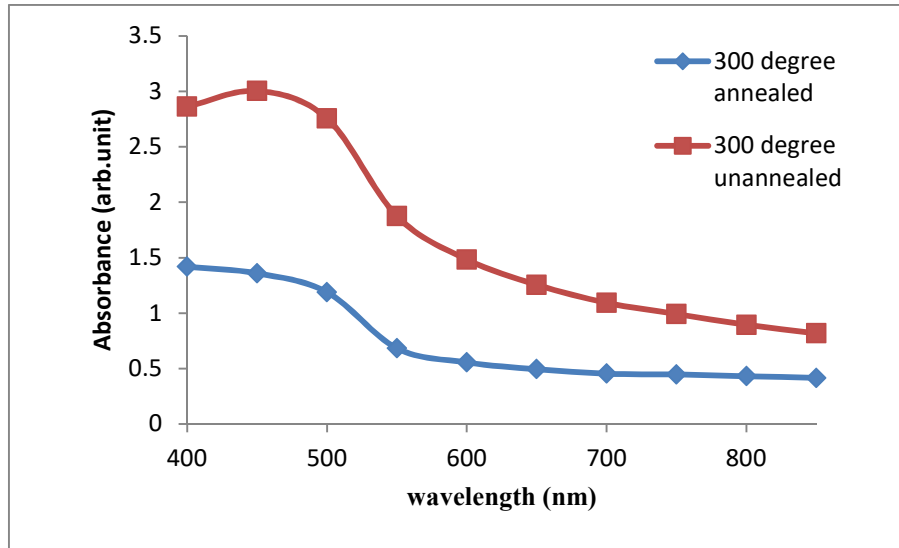


FIG. 6. Comparison of the variation of absorbance with wavelength for films sprayed at 300°C with the one annealed at 500°C.

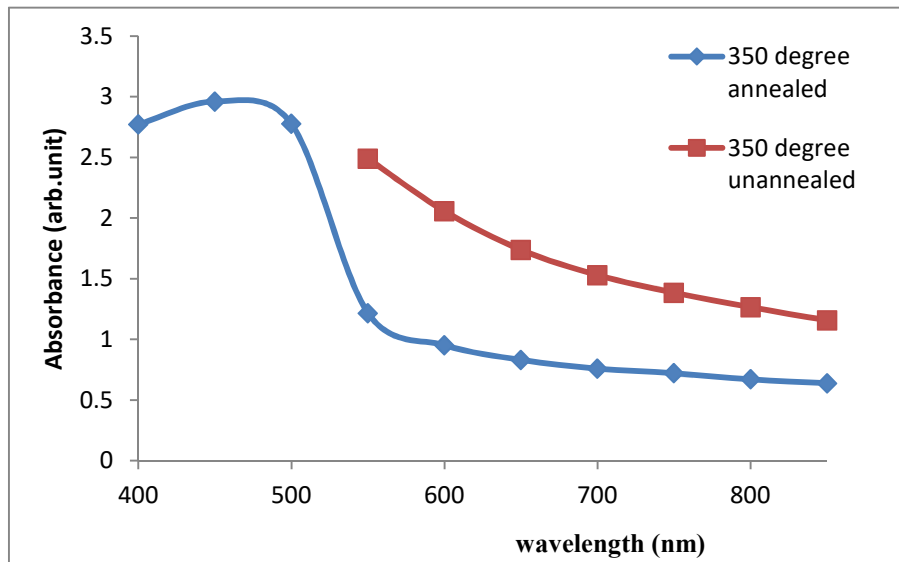


FIG. 7. Comparison of the variation of absorbance with wavelength for films sprayed at 350°C with the one annealed at 500°C.

Energy Band Gap

Moreover, the optical band gap E_g of the CdS thin film prepared was also determined from the absorption spectra using the Tauc-relation given as $\alpha hf = A (hf - E_g)^n$. With n as $\frac{1}{2}$ for a direct transition, since the semiconductor compound – CdS is having a direct band gap, α is the absorption coefficient, the energy band gap was obtained from the plot of $(\alpha hf)^2$ vs. hf , where h is Planck's constant and f is frequency. The absorption coefficient, $\alpha = \frac{2.303 A}{t}$, where ' t ' is the film thickness. This was done by extrapolating the linear portion of the plots to obtain the direct band gap of the films.

From Fig 8, the energy gap of the film as-prepared at 350°C is around 1.88 eV, while it is about 2.26eV for the same film annealed at 500°C. This shows that treating the film with heat, i.e., annealing, actually affects its optical properties. The annealed film has its band gap increased. The value of the energy band gap obtained for the annealed film is close to the bulk value for cadmium sulphide, which is 2.42eV.

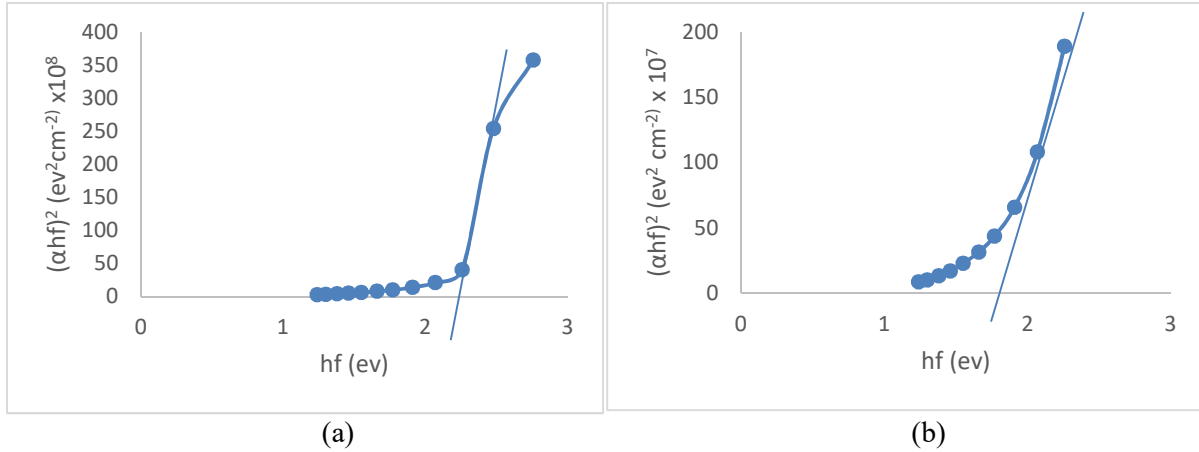


FIG. 8. Energy band gap of film as-prepared at (a) 350°C and (b) as-prepared at 350°C then annealed at 500°C.

A comparison of the band gaps of films prepared at different substrate temperatures is shown in Fig. 9. The band gaps at 250°C, 300°C and 350°C as-prepared are about 2.26eV, 2.07eV and 1.88eV, respectively. It was observed that the band gap decreases as the substrate temperature used to prepare the film increases.

This may be due to the fact that as temperature increases, some of the covalent bonds will be broken because of the thermal energy supplied to the crystal and hence the gap between the conduction band and the valence band gradually reduces.

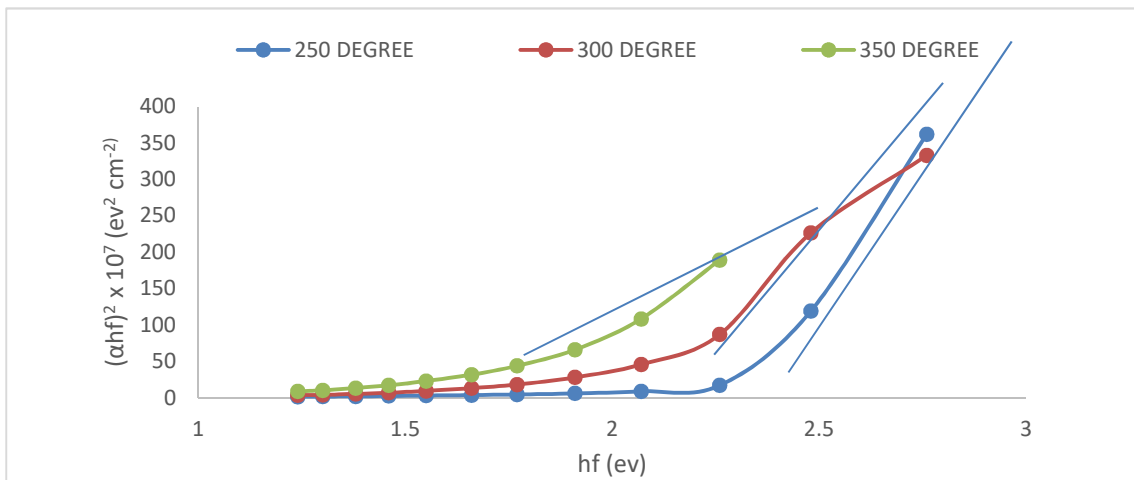


FIG. 9. Comparison of the energy band gaps of the films as-prepared at 250°C, 300°C and 350°C.

The band gap values of the CdS film prepared are around its theoretical value at room temperature given as 2.42eV and almost in

agreement with previous works on CdS, especially as reported by [1].

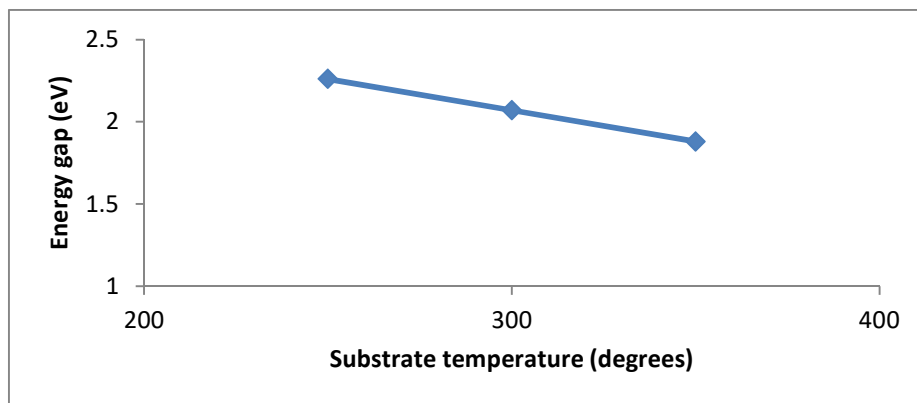


FIG. 10. Variation of energy band gap with substrate temperature of the thin films.

Refractive Index

Refractive index is a dimensionless quantity that describes how light propagates through that medium. It shows how much light is bent, or refracted, when entering a medium.

From Fig. 11, it was noticed that the refractive index reduces as the temperature used in preparing the film increases. Also, Figs. 12, 13 and 14 show that annealed films have lowered refractive indices compared to the ones not annealed. In this work, the refractive indices were calculated using the expression $n = \frac{1+\sqrt{R}}{1-\sqrt{R}}$,

where R is the reflectance values obtained from the UV-Vis spectroscopy characterization. Refractive index can also be given by the expression $n = c/v$, where n is the refractive index, c is the speed of light in vacuum and v is the speed of light in the material. Since n is inversely proportional to v , it connotes that as n reduces, the rate of transmission of electromagnetic wave in the material increases. This will actually result in better performance of the material as a good window layer in hetero-junction solar cells. The refractive index of a bulk CdS is about 2.52.

TABLE 1. The variation of refractive index with substrate temperature for the as-prepared films.

Substrate temperature (°C)	Average refractive index (in visible region), n
250	4.1
300	3.4
350	2.9

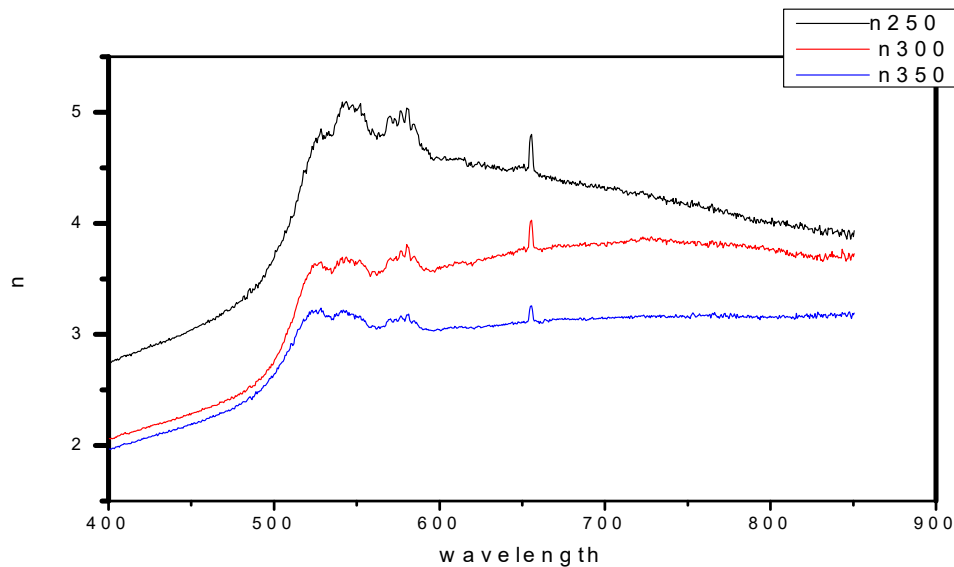


FIG. 11. Comparison of the variation of refractive indices of CdS thin films prepared at different temperatures with wavelength.

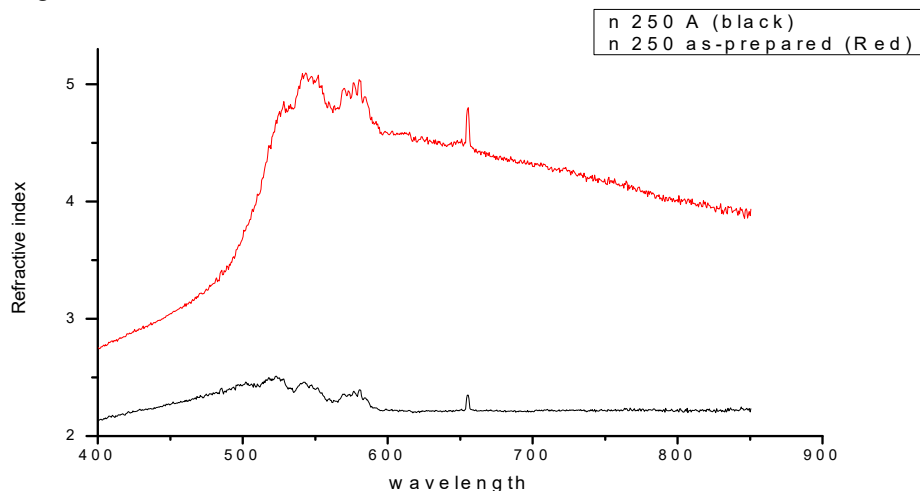


FIG. 12. Comparison of the variation of refractive indices of CdS thin films prepared at 250°C and the annealed film with wavelength.

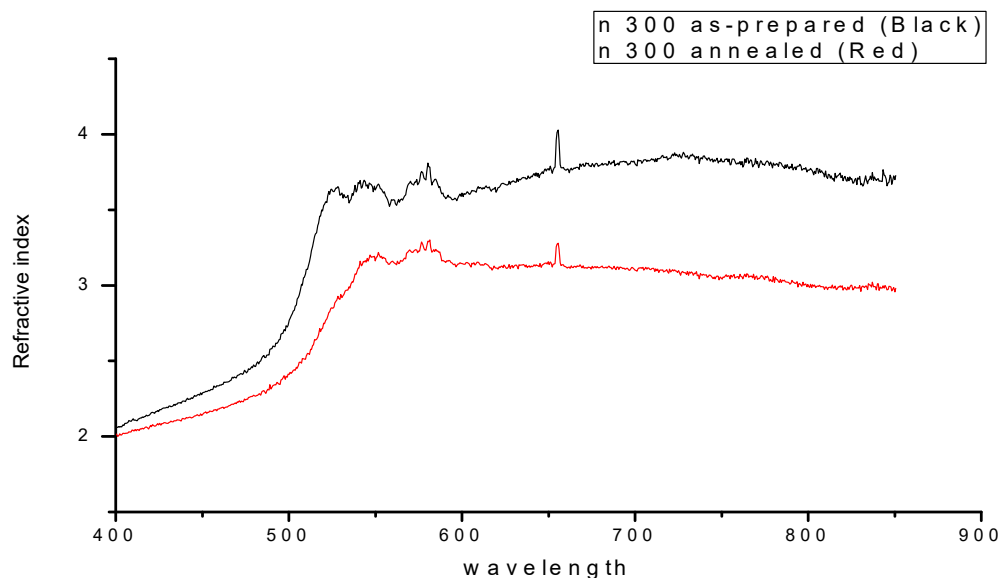


FIG. 13. Comparison of the variation of refractive indices of CdS thin films prepared at 300°C and the annealed film with wavelength.

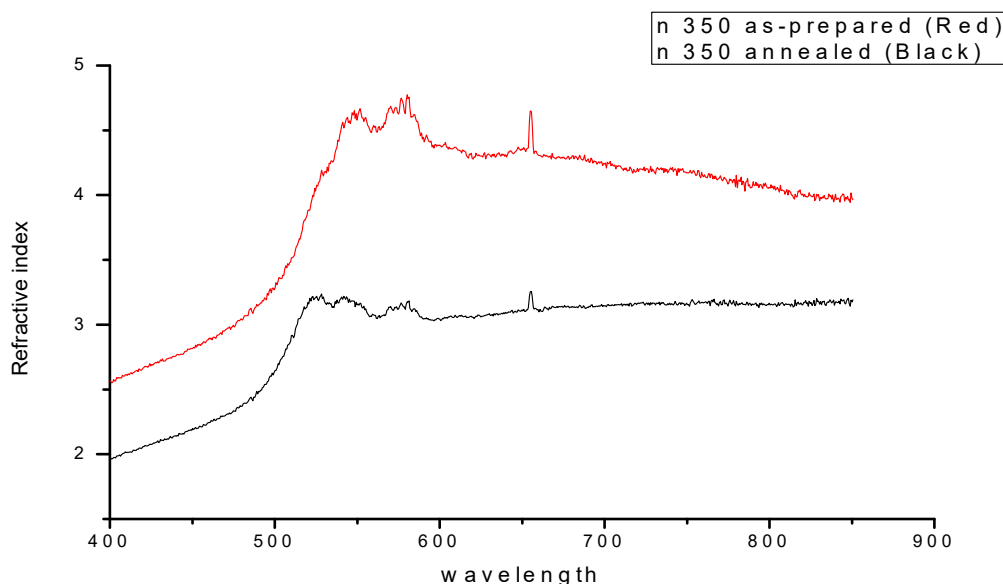


FIG. 14. Comparison of the variation of refractive indices of CdS thin films prepared at 350°C and the annealed film with wavelength.

Crystallinity of the Thin Film

The thin film was subjected to phase analysis by employing X-ray diffractometer (Model: EMPYREAN) that was equipped with $\text{CuK}\alpha$ as radiation source ($\lambda = 1.5406$ Angstrom). Only the film annealed at 500°C was characterized with XRD.

Fig. 15 shows the X-ray diffractometer pattern of CdS thin film obtained at an annealing temperature of 500°C and revealed the formation

of cadmium sulphide (CdS) with hexagonal crystal structure, though with background noise. The peaks considered at 2θ angles of 24.4, 26.0 and 27.2° correspond to diffraction from planes (1 0 0), (0 0 2) and (1 0 1), respectively, which are very close to the expected values from JCPDS 41-1049 for CdS. Using the X-ray diffraction data and Scherrer's equation given below, the average grain size was estimated.

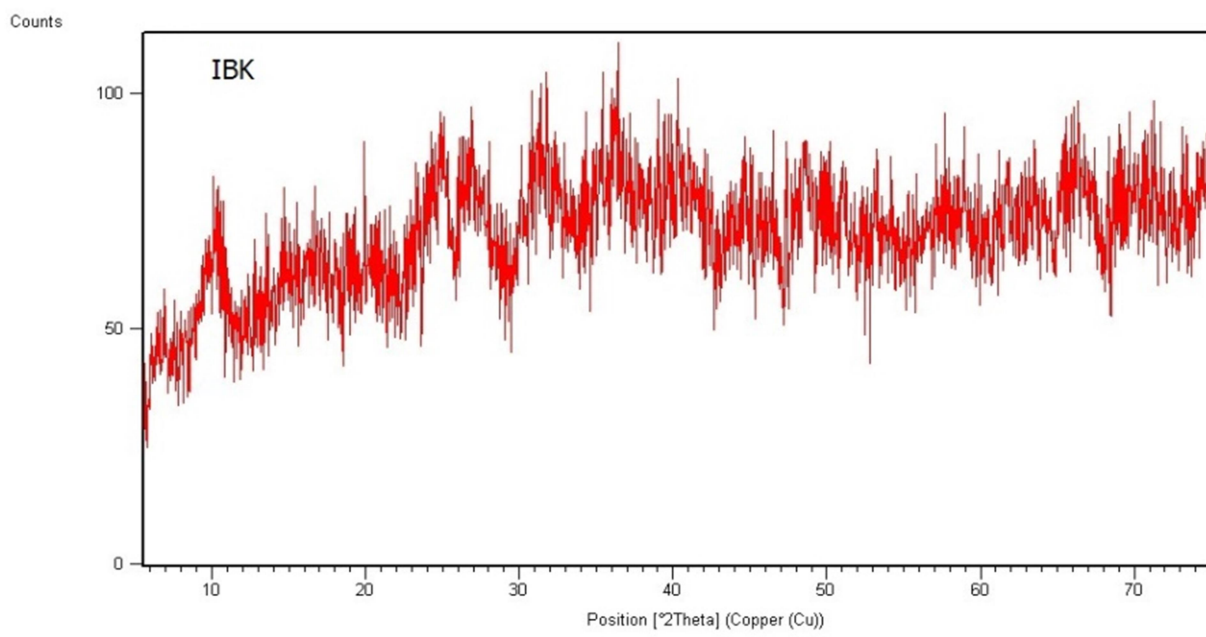


FIG. 15. XRD spectra of CdS thin film annealed at 500°C

$$g = \frac{K\lambda}{\beta \cos\theta} \quad (\text{Scherrer's equation})$$

where $K = 0.94$ is the shape factor, $\lambda =$ wavelength of X-ray used; 1.5406 Angstrom, $\beta =$ full width at half maximum (FWHM) in radians, $\theta =$ Bragg angle of the diffraction peak in radians and $g =$ average grain size.

The average grain size of CdS was calculated to be 20.50 nm, which confirmed that the CdS synthesized is in nano scale. The 2θ peaks for CdS, even though with background noise, show crystallinity of the nanostructured thin film produced by the annealing process. The noise in the XRD pattern may be due to the presence of impurities in the synthesized compound. Although not carried out in this work, the variation of substrate temperature influences phase of CdS films according to [7].

Conclusion

Cadmium sulphide (CdS) thin films have been prepared from cadmium acetate and thiourea as sources of Cd and S, respectively, using the chemical spray pyrolysis technique on micro-slide glasses. It has been observed that the films were affected by the variation of the

substrate temperatures used in preparing the thin films as well as by annealing the film. The optical band gap of the material was obtained in the range of $1.88\text{eV} - 2.26\text{eV}$. Film thicknesses, transmission spectra, optical band gaps, absorption spectra and refractive indices obtained in this investigations have really confirmed that annealing and increase in substrate temperature improve the properties of CdS for application in a solar cell and in some optoelectronic devices, because of its ability to transmit electromagnetic waves even near the infrared region, its high index of refraction and high electron affinity.

Source of Fund

The source of fund for this research is from the authors' own salaries.

Acknowledgment

The assistance given by the Materials Science Laboratory of Kwara State University, Malete, Nigeria, for the characterization done, is highly appreciated.

References

- [1] Obasuyi, A.R., Alabi, A.B., Babalola, O.A., Kajewole, E., Falana, F.H. and Robert, O., *Ilorin Journal of Science*, 1 (1) (2014) 121.
- [2] Vijaya, M.G., *International Journal of Recent advances in Physics*, 3 (1) (2014) 17.
- [3] Ashour, A., *Turk. J. Phys.*, 27 (2003) 551.
- [4] Hasnat, A. and Podder, J., *Journal of Bangladesh Academy of Sciences*, 37 (1) (2013) 33.
- [5] Ashok, CH., Venkateswara, R.K., Shilpa Charka, CH., Rajendar, V. and Lakshmi, N.R., *International Journal of Chem. Tech. Research*, 6 (6) (2014) 3367.
- [6] Abulmakarim, M., Rufai I.A. and Musa, A.O., *International Journal of Energy Engineering*, 4 (3) (2014) 61.
- [7] Meshram, R.S., Suryavanshi, B.M. and Thombre, R.M., *Advances in Applied Science Research*, 3 (3) (2012) 1563.

Density and Surface Tension of Propanol and Propanol-Water Mixtures Using Molecular Dynamic Simulations

K. A. Khasawneh^a, M. M. Al-Ali^a, R.M. Al-Salman^b, H. A. Abu-Ghazleh^b
and A. A. Obeidat^b

^a Department of Physics, Yarmouk University, Irbid, Jordan.

^b Department of Physics, Jordan University of Science and Technology, Irbid, Jordan.

Received on: 09/01/2019;

Accepted on: 14/3/2019

Abstract: Optimized Potentials for Liquid Simulations-All Atoms (OPLS-AA) and Transferable Potentials for Phase Equilibria-United Atom (TraPPE-UA) have been examined with two water models (TIP4P and SPC/E) to estimate the density and the surface tension for unary propanol and binary propanol-water mixtures. While both models predicted the experimental trend of the density for the unary system as a function of temperature and for the binary mixtures as a function of mole fraction of propanol, TraPPE-UA shows better fit with experimental data of pure propanol at low temperatures range (200K-300K). On the other hand, for the surface tension, TraPPE-UA provides a better agreement with the experimental data for pure propanol, while OPLS-AA shows better agreement for the binary mixtures at 300K for the entire mole fraction of propanol (0-1). The density profiles of the mixtures show that the structure of the mixtures changes from core-shell at low mole fractions of propanol to well-mixed at high concentrations of propanol.

Keywords: Molecular dynamics, Surface tension, Liquid density, OPLS-AA, TraPPE-UN.

PACS: 61.20. Ja, 68.03.Cd, 86.15.N.

Introduction

Molecular dynamic simulation is one of the best methods to study soft matter both quantitatively and qualitatively. Molecular dynamics is a computer simulation method that can be used to study thermodynamic and structural properties of physical systems consisting of a large number of subsystems, by providing a direct path from microscopic information to macroscopic properties. Such systems are aliphatic alcohols and their aqueous solutions, which have attracted the attention of many researchers over the past several years [1-11], due to their large variety of applications in industry, engineering, medical and biological sciences [12, 13]. Studying the density of these systems at different mole fractions is important in determining the nature of these fluids when they are mixed together. From density, one

might expect an initial structure of the mixture (well-mixed, core-shell, Russian doll); either miscible or immiscible. On the other hand, studying the surface tension is of great importance for studying many phenomena, such as: nucleation rates, sedimentation, hydrophobic effects, distillation, extraction, absorption, diffusion, among others. Regarding propanol-water mixtures, many scientists have studied this system thoroughly. Vargha-Butler et al. studied the effect of surface tension of the mixture on sedimentation of coal particles [14] and found out that the sedimentation of coal no. 8 *versus* surface tension has two maxima; when the effective surface tension of the coal particles equals the surface tension of the mixture. Raina et al. studied the surface enrichment in alcohol-water mixtures [15] and found out that surface enrichment is considerably more pronounced in

the case of *n*-butanol and *n*-propanol compared to that of ethanol. Surfaces of alcohol-water mixtures studied by sum-frequency generation vibrational spectroscopy have been reported by Sung et al. [16], who found out that the sum-frequency signal is always larger in the mixture than for pure alcohols. As an example, they found out that the sum-frequency signal of the mixture at a mole fraction of propanol of 0.1 is three times larger than that of pure propanol. Surface tension of alcohol-water mixtures has been measured by Gonzalo et al. [17] from 20-50 C and that of propanol-water mixtures at different temperatures and different mole fractions of propanol was studied by Hoke and Chen [18]. Densities of propanol-water mixtures have been measured thoroughly by Mikhail and Kimel [19].

Computationally, many potential models of alcohol have been developed to produce the right properties. Among those, we found out that the best two models for methanol and ethanol are the OPLS-AA [20] and the TraPPE-UA [21]. In this work, we have calculated the thermodynamic properties of propanol at relatively low temperatures from 200K-300K and water-propanol at room temperature with different mole fractions of propanol mixed with SPC/E [22] and TIP4P-water [23] models. The thermodynamic properties were calculated and compared with experimental published data [17, 18] for density and surface tension, while dynamical and structural properties of the system have been postponed to our forthcoming paper.

Simulation Details

After the good preferences of the TraPPE-UA and OPLS-AA models in reproducing the structural, dynamical and thermodynamic properties of methanol-water and ethanol-water systems [24, 25], we chose these potentials to

simulate propanol and propanol-water systems. In both models, propanol is considered to be rigid. Regarding the water potential models, we chose the TIP4P- water and the SPC/E- water models due to their validity of reproducing most of the real water properties. In all our MD simulations, periodic boundary conditions are applied in all directions. The pair intermolecular potential between atoms *i* and *j* is the sum of Lennard-Jones (LJ) and Coulomb potential, as follows:

$$V_{ij}(r_{ij}) = \frac{q_i q_j}{4\pi\epsilon_0 r_{ij}} + 4\epsilon_{ij} \left(\left(\frac{\sigma_{ij}}{r_{ij}} \right)^{12} - \left(\frac{\sigma_{ij}}{r_{ij}} \right)^6 \right)$$

where ϵ_{ij} and σ_{ij} are the LJ parameters for interaction between atoms of different types. The Lorentz-Berthelot rules are used for the interaction between the unlike atoms: $\sigma_{ij} = (\sigma_i + \sigma_j)/2$ and $\epsilon_{ij} = \sqrt{\epsilon_i \epsilon_j}$.

In this work, GROMACS package was used to perform all simulations [26]. The molecules are confined first inside a box of dimensions of about 3x3x10 nm³(see Fig.1), then the box is inserted in the middle of a bigger box of dimensions of 3x3x30 nm³, to assure vacuum in both sides of the binary mixture with 1000 molecules. For the unary systems, the size of the slab is 3x3x3 nm³, while the size of the whole simulation box is 3x3x12 nm³ with a total number of molecules of 600. Our systems are equilibrated for 1ns using Berendsen algorithm [27] under a pressure of 1 bar, followed by 4ns equilibration under a constant volume using Nose-Hoover thermostat [28, 29]. All the data is collected after 10ns and the cutoff radius of interaction is taken as 1.3 nm for OPLS-AA and 1.4 nm for TraPPE-UA [21], for the Leonard Jones potential and for the particle mesh Ewald (PME) [30] long-range interaction, respectively.

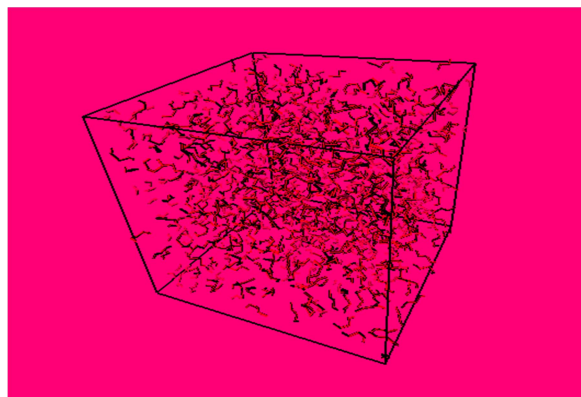


FIG. 1. Simulation box of the water-propanol mixtures (water (blue), propanol (red)).

Results and Discussion

We have computed two different thermodynamic properties of liquid propanol and its binary mixture with water for nine and four site potential models of propanol and two potential models of water.

Density

Vapor- liquid phase diagram is one of the most important quantities that can be used to confirm the validity and accuracy of a new model of soft- matter, through comparing the density with experimental data. Usually, the most published model data starts from room temperature up to an estimated critical temperature. At low temperatures, scaled model is the only rigorous method to estimate the vapor density [31, 32].

We followed the usual method of estimating liquid density by inserting all molecules in a slab within a larger empty box and fitting the profile

density to hyperbolic tangent function after assigning zero to the vapor density.

$$\rho(z) = \frac{1}{2}(\rho_l + \rho_v) - \frac{1}{2}(\rho_l - \rho_v)\tanh\left(\frac{z - z_0}{d}\right)$$

where ρ_l and ρ_v are the bulk densities of the liquid and vapor, respectively, z_0 is the position of the Gibbs dividing surface and d is the width of the interface. The graphic representation of our MD data for both TraPPE-UA and OPLS-AA shows that density decreases linearly with temperature. The results in Fig. 2 indicate that the TraPPE-UA potential model shows a better agreement with the experimental values [17] compared to OPLS-AA. This also occurred in our previous work on methanol and ethanol mixtures with water [24, 25]. This result is not surprising, since TraPPE-UA was modeled originally to give the best vapor- liquid phase diagram.

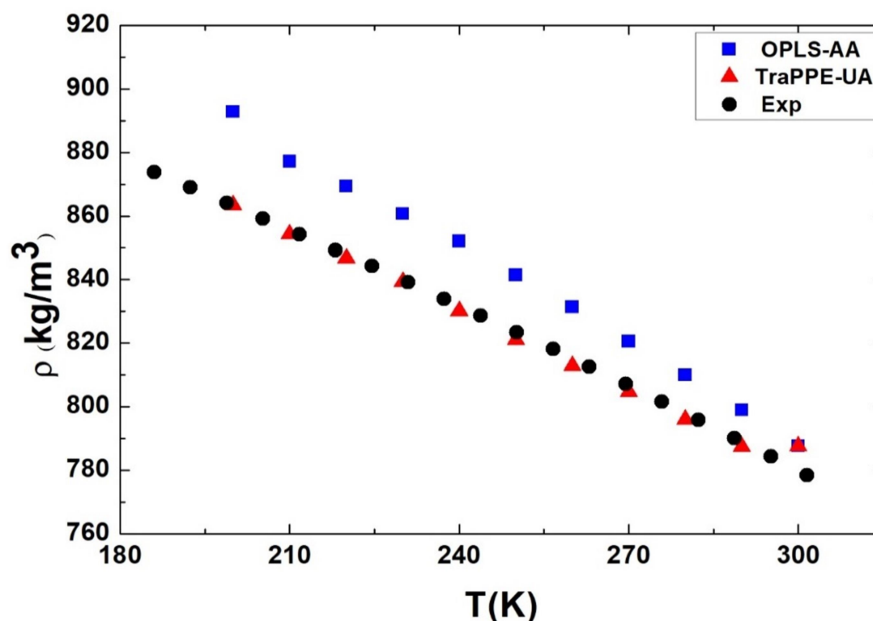


FIG. 2. Density of propanol as a function of temperature: OPLS-AA (blue), TraPPE-UA (red) and experimental data (black).

Fig. 3 shows the density profiles for water, propanol and the mixture at propanol mole fractions of 0.02, 0.08, 0.4 and 0.8. At relatively small values of mole fractions, we have noticed that most of propanol molecules lie near the surface (see the horn shape for the 2% and 8% curves) and very few molecules penetrate inside the water cluster. This behavior indicates that the initial structure of the mixture is a core-shell structure. At higher mole fractions of propanol (see for eg the curves for 40% and 80% curves),

propanol molecules tend to lie at the surface and the excess molecules tend to penetrate easily inside the water cluster as indicated by the density curves, which are almost uniform inside the core, indicating that the structure is well-mixed. This eventually is expected to reduce the surface tension of the mixture drastically, as we will elaborate further in Fig. 6. This behavior has been clearly noticed in the supplementary reading of methanol-water mixtures [24].

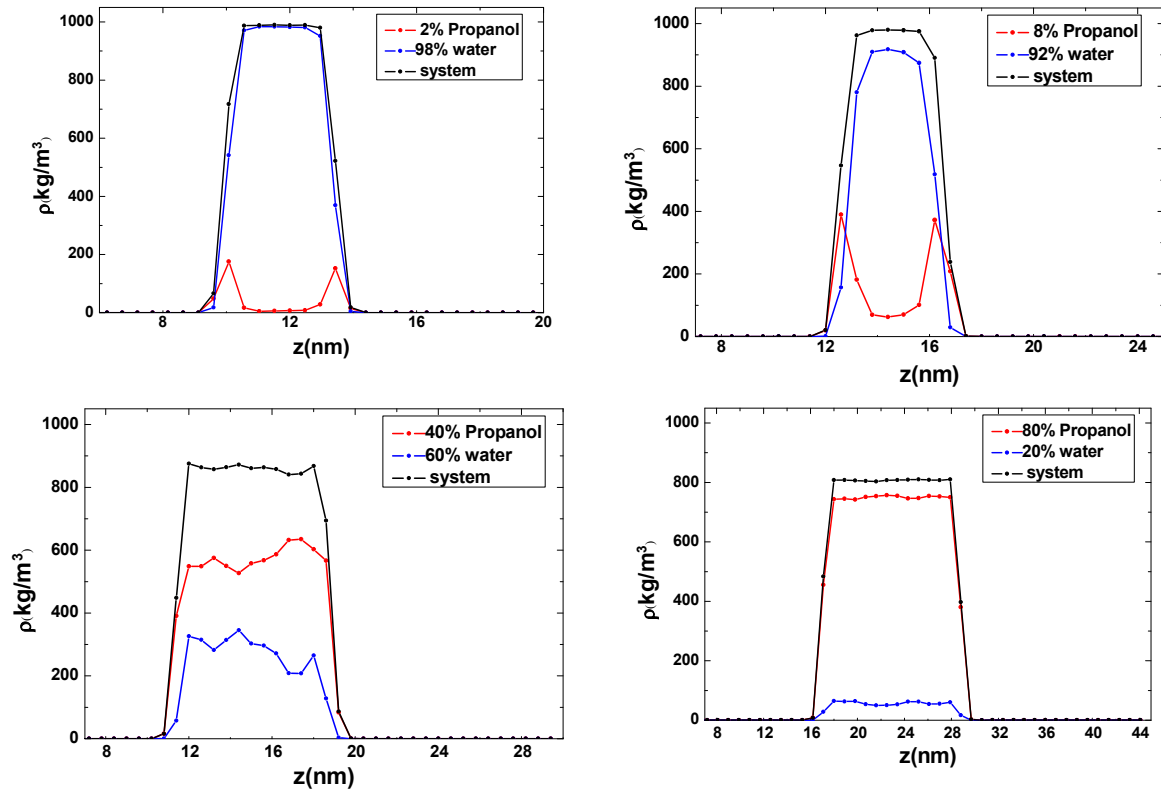


FIG. 3. Density profiles of OPLS-AA with TIP4P-water at mole fractions of propanol of 0.02, 0.08, 0.4 and 0.8.

Fig. 4 shows the density of TIP4P-water, propanol (OPLS-AA and TraPPE-UA) and the system compared to experimental data [19] as a function of mole fraction of propanol. We notice that the total density is linear, which means that the total density follows the relation of mixing rules; i.e., $\rho(x) = (1 - x)\rho_{lw} + x\rho_{lp}$, where ρ_{lw} is the density of pure water, ρ_{lp} is the density of pure propanol and x is the mole fraction of propanol. This means that in order to calculate

the total density at a specific mole fraction, one needs only the end points and to apply the relation of mixing rules. On the other hand, the small deviation between the total density calculated from the simulation and the total density calculated from the relation of mixing rules might be due to non-additive feature of the intermolecular potential; i.e., the Lorentz rule of mixing might not be totally satisfied [33, 34].

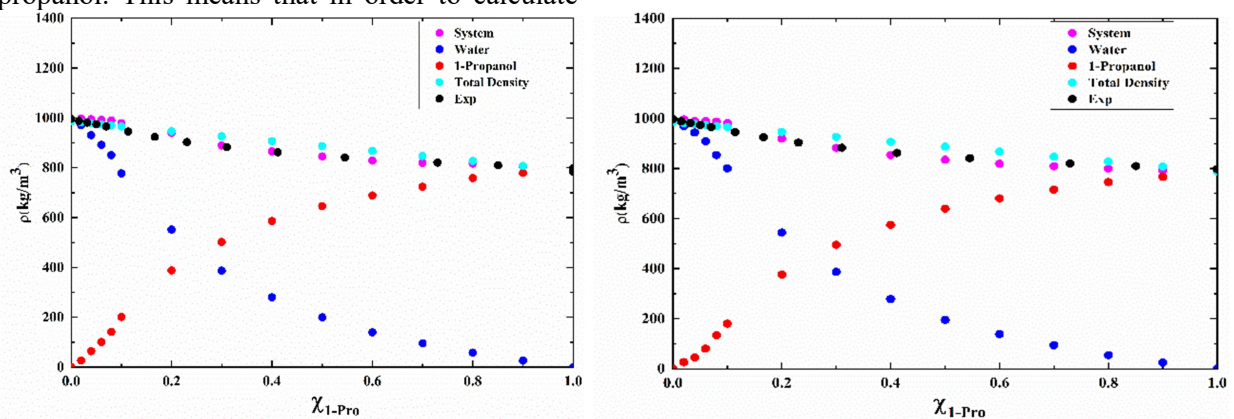


FIG. 4. Density of OPLS-AA propanol (left), TraPPE-UA (right), TIP4P-water (blue), total density from relation of mixing rules (green), system (magenta) and experimental data (black).

Surface Tension

The net force on the interior molecules of a liquid is zero, since the cohesive forces due to its neighboring molecules cancel each other. On the

other hand, the molecules at the surface do not have the same neighboring molecules on all sides; therefore, as a result, the net force on the

molecules pulls them inward causing the surface to become under tension.

There are many different methods to estimate the surface tension. In our work, we used the following relation:

$$\gamma = \frac{L_z}{2} \int \left(P_{zz} - \frac{P_{xx} + P_{yy}}{2} \right) dz + 2\pi\sigma^6 (\rho_l - \rho_v)^2 \int_0^1 ds \int_{r_c}^{\infty} \coth\left(\frac{rs}{d}\right) \frac{3s^3 - s}{r^3} dr$$

where $p_{\alpha\alpha}$ is the $\alpha\alpha$ component of the pressure tensor, L_z is the box length in the z direction, ϵ and σ are the Lennard-Jones parameters and r_c is the cutoff radius. The second term has been taken under the consideration of tail correction [35].

To get accurate results of surface tension in the presence of high fluctuations in pressure, we equilibrated our system for a long time, sometimes for 10 ns and then collected the data for further 10 ns.

Fig. 5 shows the effect of temperature on surface tension for pure propanol. It is clear that the surface tension of propanol decreases with temperature in both models, even though the surface tension obtained with TraPPE-UA model has high fluctuations, whereas the OPLS-AA model follows the same trend regarding the linearity behavior. However, the results show that TraPPE-UA model is better in matching the experimental data, whereas the OPLS-AA fail in producing the experimental data over the whole temperature range.

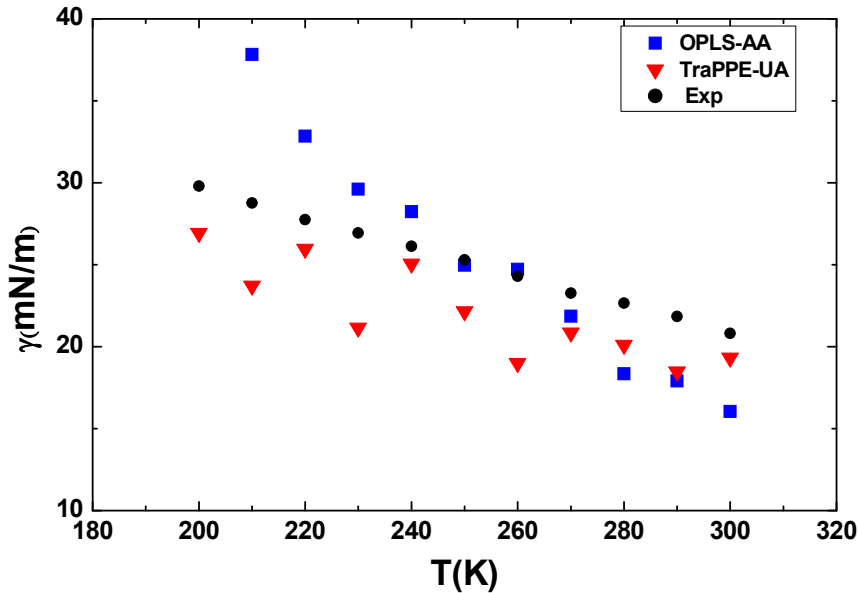


FIG. 5. Surface tension as a function of temperature, OPLS-AA (blue), TraPPE-UA (red) and experimental data (black).

The surface tension of propanol-water mixture was also calculated at different mole fractions of propanol from $\chi_{propanol} = 0.02$ to 0.1 with steps of 0.02 followed by steps of 0.1 up to $\chi_{propanol} = 1$.

Fig. 6 shows our simulation results for the surface tension of the binary system using TraPPE-UA and OPLS-AA force fields, with TIP4P-water compared to the experimental data. At rich water region, both TraPPE-UA and OPLS-AA potential models fit the experimental

data very well. At rich propanol region, the OPLS-AA potential model shows better agreement with the experimental data.

We can explain the fast drop of surface tension in Fig. 3 by that for small fractions of propanol, the surface of drop is mostly covered by water molecules and by increasing the mole fraction of propanol, the propanol molecules prefer to spread over the surface, which is a dominating factor in surface tension.

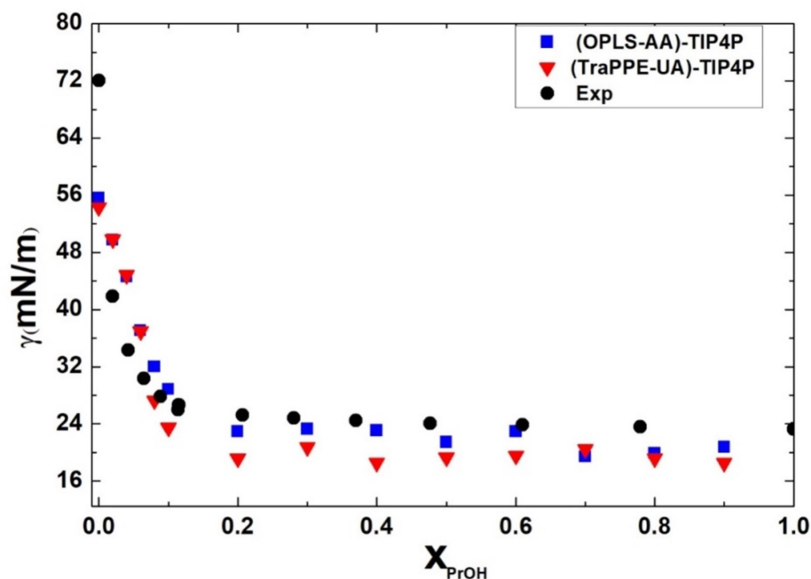


FIG. 6. Surface tension of propanol mixed with TIP4P-water at different mole fractions of propanol compared to experimental data (black), OPLS-AA with TIP4P (blue) and TraPPE-UA with TIP4P (red).

Conclusion

In this work, a series of molecular dynamic simulations (MD) have been performed in order to examine the validity and performance of the (TraPPE-UA) and (OPLS-AA) potential models in producing the thermodynamical properties of pure propanol and its aqueous mixtures by comparing the simulation results for the density and surface tension with the experimental data. Both models are in agreement with the experimental data for the temperature dependence of the density for pure propanol and the mole fraction dependence of the density for the propanol aqueous mixtures. The density profiles of the propanol-water mixtures indicate that at low molar concentrations of propanol (below $\sim 30\%$), the structure of the drop is a core shell, while for high molar concentrations of propanol (above $\sim 40\%$), the structure tends to be well-mixed solution. Moreover, the results of

the simulation showed that the total density of the mixture follows the relation of mixing rules.

Regarding the surface tension, (TraPPE-UA) performs better in producing the data for pure propanol, while (OPLS-AA) gives better results for the propanol-water mixtures. The results showed a fast drop in the surface tension as the propanol mole fraction increased, indicating that the propanol molecules prefer to lie on the surface of the water drop.

Overall, this means that one cannot judge the preference of one model over the other without considering the property to be studied. As an example, if one wants to study the nucleation of unary propanol and since nucleation rates depend on the surface tension to the power three, one is advised to use TraPPE-UA. Inversely, when calculating the nucleation rates of the binary water-propanol mixtures, it is more appropriate to use the OPLS-AA model.

References

- [1] Biscay, F., Ghoufi, A. and Malfreyt, P., *Journal of Chemical Physics*, 134 (2011) 044709.
- [2] Derlacki, Z., Easteal, A., Edge, A., Woolf, L. and Roksandic, Z., *Journal of Physical Chemistry*, 89 (1985) 5318.
- [3] Dixit, S., Soper, A., Finney, J.L. and Crain, J., *EPL (Europhysics Letters)*, 59 (2002) 377.
- [4] Easteal, A.J. and Woolf, L. A., *Journal of Physical Chemistry*, 89 (1985) 1066.
- [5] Galicia-Andrés, E., Dominguez, H., Pusztai, L. and Pizio, O., *Journal of Molecular Liquids*, 212 (2015) 70.
- [6] Gereben, O. and Pusztai, L.S., *Journal of Physical Chemistry B*, 119 (2015) 3070.

- [7] Gong, X., Bandis, A., Tao, A., Meresi, G., Wang, Y., Inglefield, P., Jones, A. and Wen, W.-Y., *Polymer*, 42 (2001) 6485.
- [8] Guevara-Carrion, G., Vrabec, J. and Hasse, H., *Journal of Chemical Physics*, 134 (2011) 074508.
- [9] Soetens, J.-C. and Bopp, P.A., *Journal of Physical Chemistry B*, 119 (2015) 8593.
- [10] Zhang, N., Shen, Z., Chen, C., He, G. and Hao, C., *Journal of Molecular Liquids*, 203 (2015) 90.
- [11] Bakó, I., Pusztai, L. and Temleitner, L., *Scientific Reports*, 7 (2017).
- [12] Ballal, D. and Chapman, W.G., *Journal of Chemical Physics*, 139 (2013) 114706.
- [13] Ghahremani, H., Moradi, A., Abedini-Torghabeh, J. and Hassani, S., *Der Chemica Sinica*, 2 (2011) 212.
- [14] Vargha-Butler, E., Zubovits, T., Absolom, D., Neumann, A. and Hamza, H., *Chemical Engineering Communications*, 33 (1985) 255.
- [15] Raina, G., Kulkarni, G. and Rao, C., *Journal of Physical Chemistry A*, 105 (2001) 10204.
- [16] Sung, J., Park, K. and Kim, D., *Journal of Physical Chemistry B*, 109 (2005) 18507.
- [17] Vazquez, G., Alvarez, E. and Navaza, J.M., *Journal of Chemical and Engineering Data*, 40 (1995) 611.
- [18] Hoke Jr, B.C. and Chen, J.C., *Journal of Chemical and Engineering Data*, 36 (1991) 322.
- [19] Mikhail, S. and Kimel, W., *Journal of Chemical and Engineering Data*, 8 (1963) 323.
- [20] Jorgensen, W.L., Maxwell, D.S. and Tirado-Rives, J., *Journal of the American Chemical Society*, 118 (1996) 11225.
- [21] Keasler, S.J., Charan, S.M., Wick, C.D., Economou, I.G. and Siepmann, J.I., *Journal of Physical Chemistry B*, 116 (2012) 11234.
- [22] Berendsen, H., Grigera, J. and Straatsma, T., *Journal of Physical Chemistry*, 91 (1987) 6269.
- [23] Jorgensen, W.L., Chandrasekhar, J., Madura, J.D., Impey, R.W. and Klein, M.L., *Journal of Chemical Physics*, 79 (1983) 926.
- [24] Obeidat, A. and Abu-Ghazleh, H., *AIP Advances*, 8 (2018) 065203.
- [25] Obeidat, A., Al-Salman, R. and Abu-Ghazleh, H., *AIP Advances*, 8 (2018) 075321.
- [26] Van Der Spoel, D., Lindahl, E., Hess, B., Groenhof, G., Mark, A.E. and Berendsen, H.J., *Journal of Computational Chemistry*, 26 (2005) 1701.
- [27] Berendsen, H.J., Postma, J.V., van Gunsteren, W.F., DiNola, A. and Haak, J., *Journal of Chemical Physics*, 81 (1984) 3684.
- [28] Hoover, W.G. and Hoover, C.G., "Time reversibility, computer simulation, algorithms, chaos", (World Scientific, 2012).
- [29] Nose, S., *Journal of Physics: Condensed Matter*, 2 (1990) SA115.
- [30] Darden T., York D. and Pedersen, L., *Journal of Chemical Physics*, 98 (1993) 10089.
- [31] Hale, B.N. and Thomason, M., *Physical Review Letters*, 105 (2010) 046101.
- [32] Hale, B.N. and Ward, R.C., *Journal of Statistical Physics*, 28 (1982) 487.
- [33] Saija, F., Fiumara, G. and Giaquinta, P., *Journal of Chemical Physics*, 108 (1998) 9098.
- [34] Saint-Martin, H., Medina-Llanos, C. and Ortega-Blake, I., *Journal of Chemical Physics*, 93 (1990) 6448.
- [35] Chapela, G., Chapela, G.A., Saville, G., Thompson, S.M. and Rowlinson, J.S., *J. Chem. Soc., Faraday Trans.*, 2 (73) (1977) 1133.

Simulation-Assisted Environment-Mapping Using Unidirectional Ultrasonic Pulses

M. Al-Shorman^a, M. Al-Kofahi^b and Q. I. Mohaidat^a

^a *Department of Physics, Yarmouk University, Irbid, Jordan.*

^b *Department of Computer Information Science, Higher College of Technology, Ras Al-Khaimah, UAE.*

Received on: 30/9/2018;

Accepted on: 17/3/2019

Abstract: In this paper, a new system for mapping and discovering an environment using simple ultrasound transceivers, connected to a microcontroller, is developed with the aid of an ultrasonic wavelet propagation simulation program. Environment mapping is achieved by sending ultrasonic pulses with known characteristics and listening to the reflections from all directions in real time. The change induced in the shape of a pulse wavefront due to reflection is found to be dependent on the barriers in the environment and on its geometry. The correlation between the changes in the shapes of the wavefronts and the shapes of the reflecting objects is investigated. This includes the slope or curvature of the reflecting wall (or barrier), wall tilt or angle and possible twists in corners. By analyzing the interference patterns and counting the interference fringes in the reflected pulses, a method for measuring object orientation is developed. The presented technique can also discover unseen objects behind corners. The results obtained show that this method is not only effective in discovering an environment, but also in measuring subtle features, such as the rotation of an object with an accuracy of 0.1° . The mapping and discovery techniques described in this paper are targeted for artificial intelligence applications and robotics. The infinite number of possibilities in the reflected wavefront characteristics, due to the similarly infinite environment shapes, makes experimentally collecting this data impossible. The simulated data presented in this paper will take more than six months to be collected experimentally.

Keywords: Simulation, Environment mapping, Unidirectional ultrasonic pulses.

Introduction

Several strategies have been used to obtain an environment's features using ultrasonic sensors due to their low cost and simplicity. Mapping and navigating an environment can be very useful in many applications.

Recent advances in navigation range from navigating wheel chairs [1] to vehicles [2] or any robot in general [3, 4, 5, 6]. For example, the authors in [7, 8] used signals from a set of distributed ultrasonic sensors to locate obstacles in 3D to help navigate a robot.

Mapping applications range from small features and cavities [9, 10, 11] to larger areas for robot and vehicle navigation [12, 13, 14]. The most common mapping technique is based on the time elapsed between transmission and reception of a pulse. Efforts in this field, using sound and ultrasound, varied from trying to distinguish a wall from a corner [6] or poles from trees [16], to the more elaborate efforts [17, 18, 19] of estimating a room geometry using omni-directional loudspeakers and multiple non-matched omni-directional microphones, located

randomly in the room. In these studies [17, 18], a room with different walls has been successfully described by using first-order echoes collected by microphones. However, the fact that microphones had to be scattered in a room made the technique less applicable for robotics applications. Besides, this imposed some limits on the shape of the environment.

The authors in [20, 21] introduced an active sensing technique that allows to estimate the number of occupants by detecting the changes in a room's acoustic properties. In their study, a centrally located beacon transmits an ultrasonic chirp and then records how the signal dissipates over time. By analyzing the frequency response over the chirp's bandwidth at a few known occupancy levels, they are able to extrapolate the response as the number of people in the room changes.

Contribution

In this paper, a new method for mapping and discovering an unknown environment using *unidirectional* ultrasonic pulses, without imposing any limitation on the unknown environment shape, is presented. The new method works by extracting simple characteristics from the reflected wavefronts and relating the changes in those characteristics to previously studied surface properties. Features, such as a wall tilt/slope, an angle magnitude and pointing direction or a wall curvature, can be measured easily in less than a second. More complicated tasks, such as measuring the dimensions of a room without having a direct line of sight and detecting objects hiding behind an angle, are also possible. A new method for measuring object rotation by observing ultrasound interference patterns to an accuracy of 0.1° using 40kHz transmitter is introduced. This 0.1° accuracy can be enhanced even more by using a higher frequency transmitter. The new mapping method is targeted for compact and low-power devices, such as robots that operate on batteries, because of the low processing power needed to extract the intended wavefront features. The new method is also ideal for artificial intelligence applications, where a robot/machine can learn to discover an environment by observing a specific set of features in the reflected wavefronts.

Since collecting experimental data for the vast number of possible environment shapes

under study is not practical, an ultrasound propagation simulator was developed and used. The developed simulator was tested and validated rigorously [22].

Unlike previous environment mapping attempts, the set of transceivers used were all mounted on the same device within few centimeters from each other, rather than being scattered in a room. Although it is possible to use regular sound waves for this application, ultrasound waves are preferred, because they are silent to the human ear and give a better spatial resolution compared to sound waves due to their shorter wavelengths. Ultrasound waves also have the advantage of being less prone to background noise.

This paper is organized as follows: A brief description of the simulation program used will be given. Then, the mapping technique will be described. Next, some mapping scenarios ranging from measuring an angle to seeing hidden objects behind a corner will be discussed. Finally, a conclusion will be given and some future work will be discussed.

Ultrasound Pulse Simulator

The simulator program has two main software components: A front-end written in C# and C++ that is responsible for parsing and interpreting the user input and a back-end that runs the actual simulation kernel written using OpenCL 2.0 heterogeneous compute language. OpenCL code can be run on a regular CPU or on a Graphics Processing Unit (GPU). GPUs have the advantage of typically containing several thousand compute units, while CPUs contain only few cores. This makes GPUs ideal for some computational tasks that can be massively parallelized. In this simulator, it is assumed that a pulse consists of millions of wavelets. The simulation of each wavelet runs on a separate compute unit on the GPU. Each wavelet oscillates and moves independently according to the equation:

$$r(\vec{t}) = \frac{A_0}{r} \sin(kx - wt) \hat{r} \quad (1)$$

Once a wavelet hits a wall, it will change its direction such that the incidence angle equals the reflection angle. There is no limitation on the shape and number of walls in the simulated environment. Surface roughness and scattering are ignored.

The simulator models the following environment components:

- **Walls and obstacles:** All physical obstacles are assumed to be homogeneous. Scattering and surface roughness are ignored. All wall shapes are described inside the simulation using mathematical formulae that are not limited by shape or number. More complicated features can be described using a series of small linear segments.
- **Ultrasonic pulse with known shape and properties:** Throughout this work, a 40 kHz conic-shaped pulse that models the one generated by the commonly used, low cost HC-SR04 transceiver, is used. A pulse is assumed to consist of a large number of wavelets that are evenly spaced in the radial and angular directions. The chosen wavelet density should balance the accuracy against the simulation performance. During our tests, a 0.02° – 0.001° angular spacing and a 1.0 mm radial spacing produced good results over a distance of 3 – 5 meters. The emitted pulse spatial intensity profile is assumed to be Gaussian in the radial and angular directions. Full-width at half-maximum (FWHM), in the radial and angular directions, values of $R_{FWHM} = 30\text{mm}$ and $\Theta_{FWHM} = 60^\circ$ were found to be a good match for HC-SR04 emitted pulse. See Fig. 4.
- **Ultrasound receivers:** A receiver is simulated as a region in space that records the passing wavelet amplitude, at its location, as a function of time. The recorded intensity is proportional to the receiver effective-area facing the incident wavelet. Each receiver has a known location, width and orientation. At the end of a simulation run, each receiver will have an intensity-time profile that resulted from a large number of wavelets crossing its location at different times. In this work, a typical simulation run modeled 360 receivers arranged in a 10cm-radius circle.

To demonstrate the accuracy of the simulation, a 78.5° corner was setup and twisted 2.5° counterclockwise. This arrangement will cause the incident pulse to have three separate wavefronts once reflected. The asymmetric shape of this arrangement means that the three wavefronts will not be similar and each one of

them is expected to have a different intensity and space-time location. As shown in Fig. 3, the positions, shapes and relative intensities in the experimental data are the same as those in the simulated data.

How the Mapping Process Works

The three main components of the mapping device, shown in Fig. 1 as a 3D model, are:

Transmitter: To map an environment using the proposed technique, an ultrasound transmitter that can send a $1\ \mu\text{s}$ to $100\ \mu\text{s}$ pulse in a known direction is needed. The transmitted pulse must have a known intensity spatial distribution. The transmitter characteristics, such as the angular spread of the transmitted pulse, must be known. The transmitter should be located at the center of a circular array of receivers. Fig. 4 shows a simulated pulse spatial distribution similar to the used 40kHz HC-SR04 transceiver pulse. This transceiver works by applying $\pm 15\text{V}$ voltage pulses on its piezoelectric element. The colors in Fig. 4 represent the normalized intensity using the color scale shown to the right of the figure.

Receiver Array: Once a pulse is transmitted, a set of receivers packed in a circle, as tightly as possible, start recording the reflected intensity in real time. A sampling rate of 0.5 Mega Sample Per Second (0.5 MSPS) was sufficient during our tests. A circle of 10cm radius can pack about 360 2.5 mm-width receivers. Instead of building this large set of receivers, a smaller rotating set can do the same job albeit in a longer period of time. The data collected from this large set of receivers, as a function of time, is plotted on a two-dimensional color map, where intensity is represented by the color. The normalized intensity color scale used is shown to the right of each plot throughout this paper.

Microcontroller: The transmitter and the receiver array must be connected to a microcontroller (MCU) or a field programmable gate array (FPGA) that can handle all of the analog signals in real time. An Atmel SAM3X8E ARM CortexM3 MCU was sufficient when the receiver is attached to Wantai 42BYGHM809 stepper motor (400 steps/rev) and its generic M542H driver.

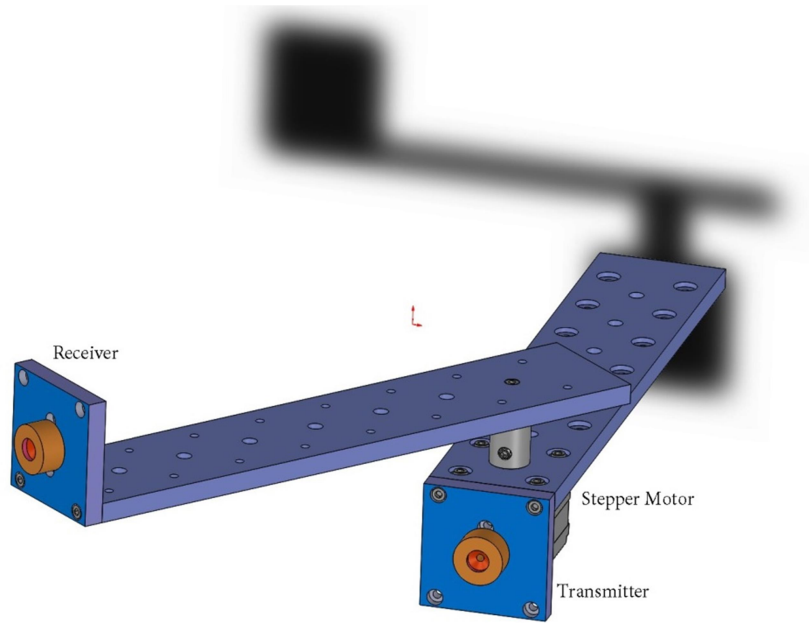


FIG. 1. Experimental setup 3D model.

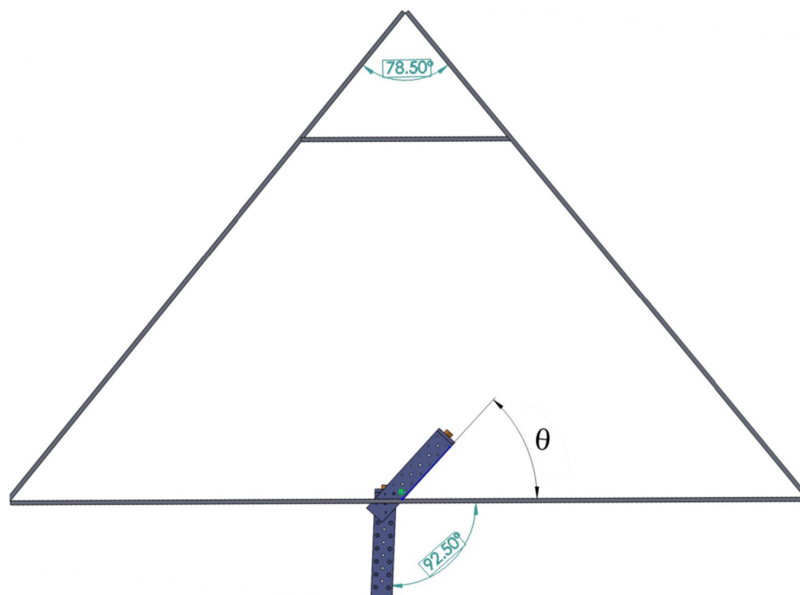
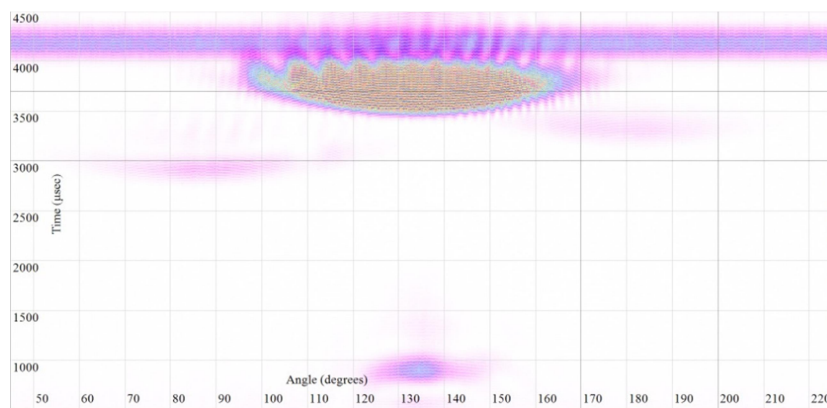
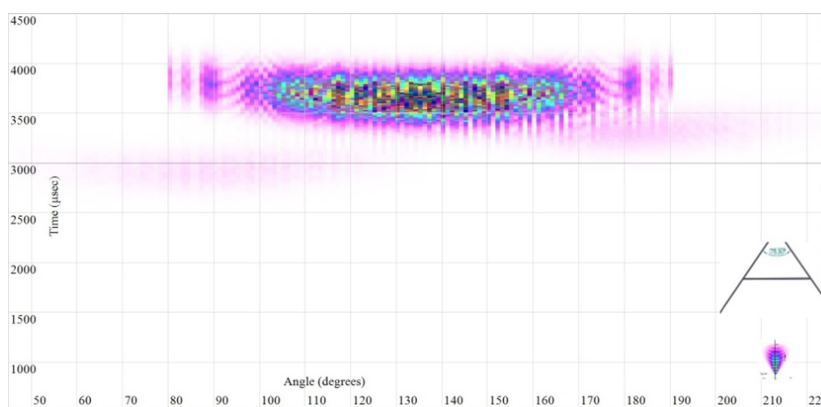


FIG. 2. Environment walls used to collect the experimental and simulated data shown in Fig. 3.



(a) Experimental



(b) Simulated

FIG. 3. Experimental vs. simulated ultrasound propagation data. The environment in which the pulse is propagating is shown in the inset of Fig. 3b and Fig. 2. The corner angle is 78.5° and is twisted 2.5° . X-axis: detector angle in degrees. Y-axis: time in micro-seconds. The normalized intensity is represented by the color scale to the right of each figure.

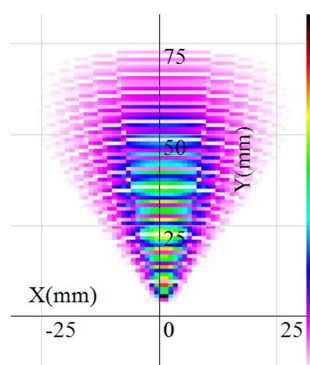


FIG. 4. A simulated 40kHz ultrasonic pulse spatial distribution similar to HC-SR04 transceiver pulse. X- & Y-axes: distance in millimeters.

Mapping Criteria

An environment can be mapped by tracking changes to the reflected pulse. For example, a reflected pulse may:

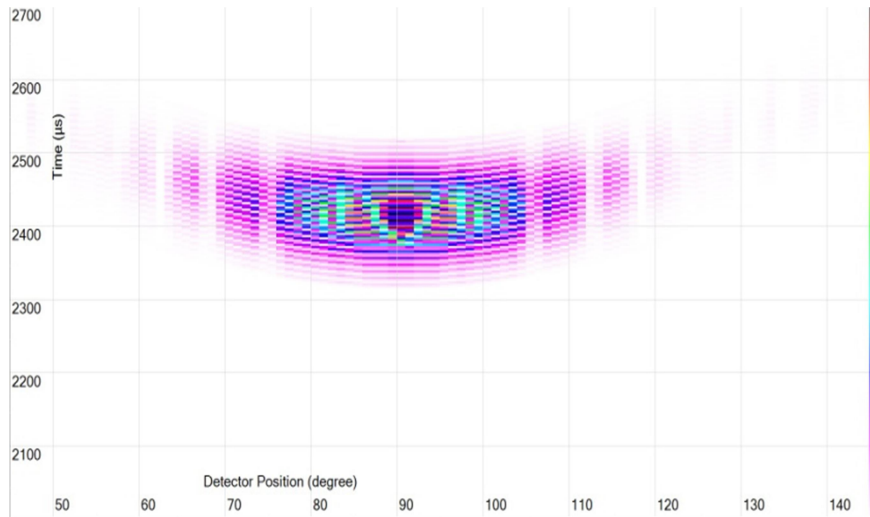
- Change its angular spread.
 - Change its time spread.
 - Get separated into two overlapping/non-overlapping wavefronts.
 - Contain wave interference patterns.
 - Include a specific object signature.
- It should be emphasized here that:
- A direct line of sight is not necessary.
 - A pulse may undergo multiple reflections before going back to the receivers.
 - The direction from which a reflected pulse comes is not necessarily the original transmission direction.

Mapping Scenarios

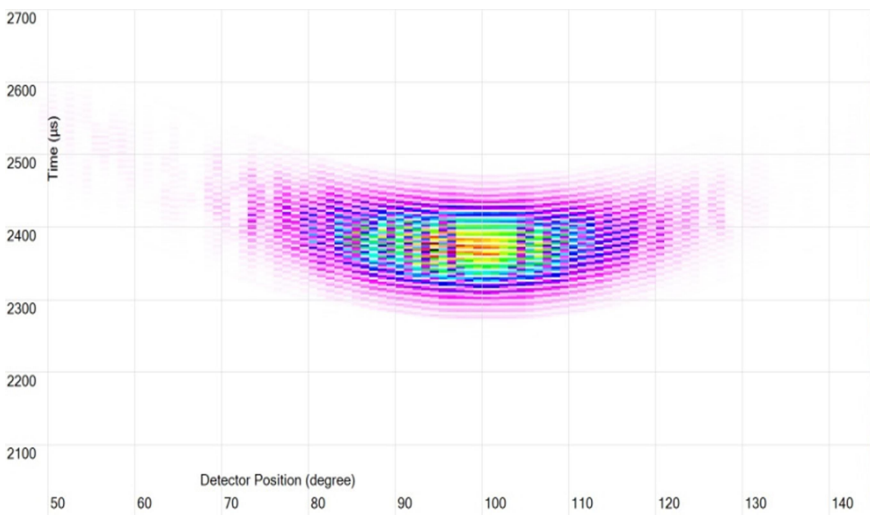
This section discusses how to infer an environment characteristic from the reflected wavefront properties. Those characteristics can be as simple as a wall slope or as complicated as detecting an unseen object behind an angle.

Measuring a Wall Slope and Curvature

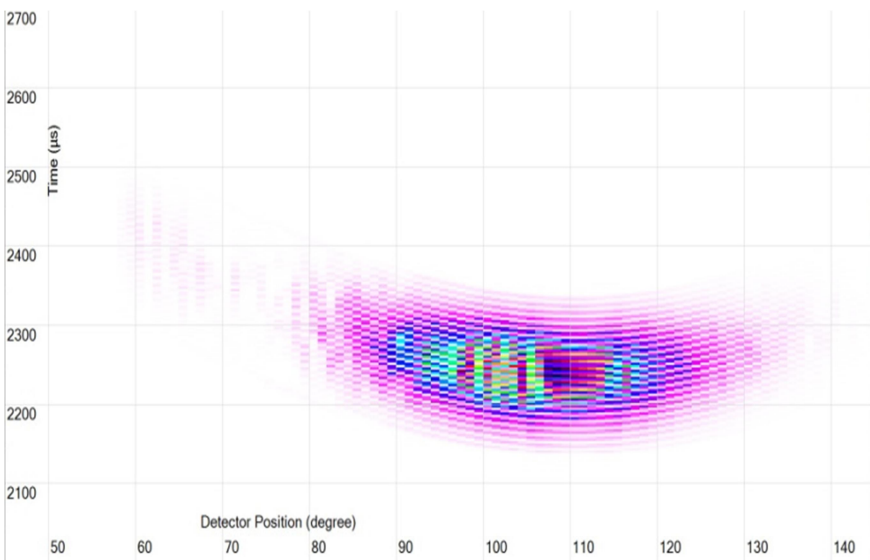
This section demonstrates how to use one of the reflected wavefront properties, its center, to calculate the slope of a wall. When a uniform pulse, such as the one shown in Fig. 4, direction of incidence is perpendicular to a wall, the reflected wavefront will come back to the direction from which it originated. The reflected wavefront will look like the reflection shown in Fig. 5a. Note that the x-axis in Fig. 5 is the detector angular position. The wavefront center in Fig. 5a, at 90° , is the original pulse incidence direction.



(a) Normal incidence



(b) 10° deviation from normal incidence.

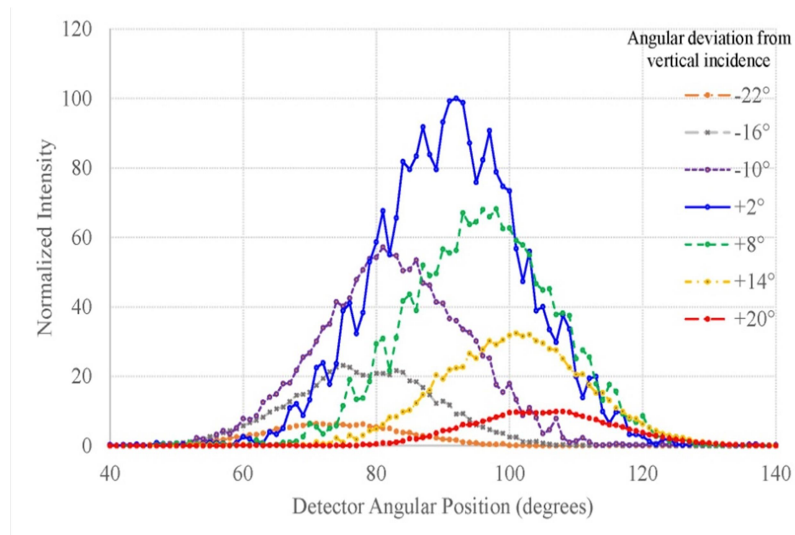


(c) 20° deviation from normal incidence.

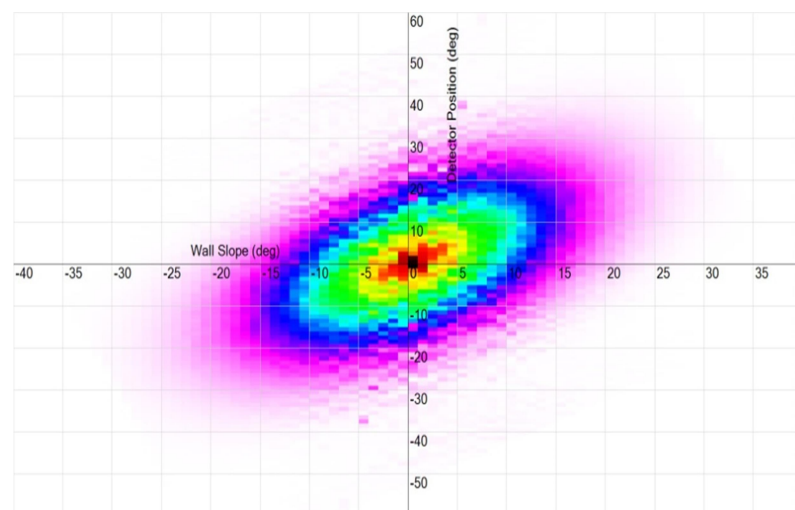
FIG. 5. Reflected wavefront for various incidence angles. X-axis: detector angle in degrees. Y-axis: time in micro-seconds. The normalized intensity is represented by the color scale to the right of each figure.

If the angle between the incident pulse direction and the wall surface starts deviating from 90° , the reflected wavefront shape will deviate from the symmetric shape. For example, Figs. 5b and 5c show the reflected wavefront if the angles between the direction of incidence and the normal to the wall are 10° and 20° , respectively. This deviation can be quantified by either integrating the reflected wavefront intensity over time (y-axis) or integrating it over detector angular position (x-axis) and then

comparing the result with normal incidence. Fig. 6a shows time-integrated intensity vs. detector angular position for various wall pointing directions. Note how the position of the peaks changes with the wall pointing direction. A large set of curves, as the ones shown in Fig. 6a, are put together in Fig. 6b. Each vertical slice from Fig. 6b represents a curve similar to the ones shown in Fig. 6a. The estimated maximum error in measuring the slope of a wall using this technique is about 4%.



(a) Time-integrated intensity vs. detector position for different wall pointing directions. A wall direction is the angle between the normal to the surface and the incidence angle.



(b) Wall pointing direction vs. detector position. The color represents the normalized intensity. The intensity color scale is shown to the right. X-axis: wall slope in degrees. Y-axis: detector position in degrees.

FIG. 6. A pulse reflected from a wall will have its position shifted by an amount that depends on the wall pointing direction.

Another property of the reflected wavefront is its width. Fig. 7 shows the final result of how this property can be used to calculate a wall curvature. The same technique can be applied for walls/corners that cannot be seen directly by

measuring reflections from a known plane wall. Discovered walls can be used as mirrors to see other objects by observing the change in a reflected wavefront position and width.

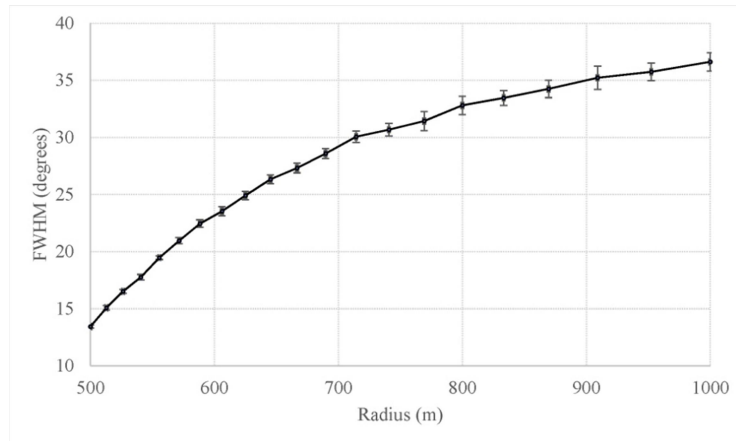
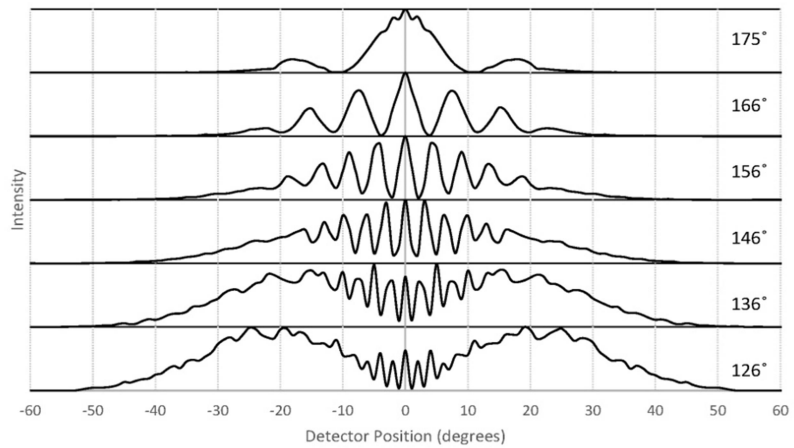


FIG. 7. Wall curvature measurement: FWHM of reflected wavefront time-integrated intensity vs. curvature radius.

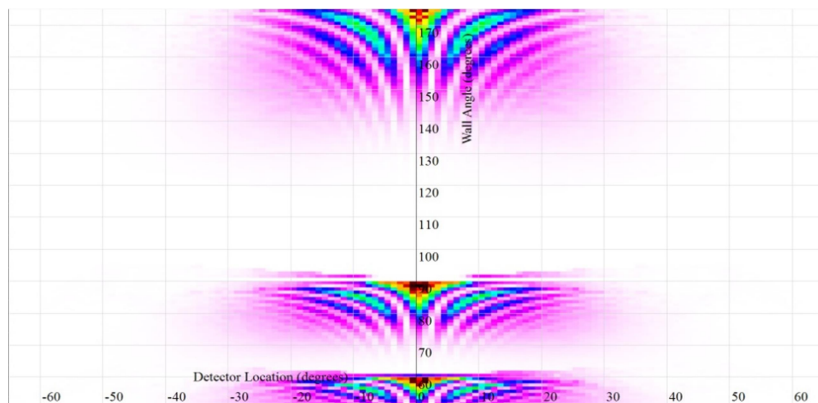
Measuring an Angle

When a pulse gets reflected from a corner, the incident wavefront will get split into two wavefronts. The reflected wavefront time-integrated-intensity vs. detector angular position is shown in Fig. 8a for various angles. Note how interference patterns start forming once the two reflected wavefronts start overlapping. When the

interference patterns are not the dominant feature of the reflected wavefront, the separation between the two peaks can be used as a metric to measure the wall angle. However, when the interference patterns are very strong, the spacing between the interference fringe separation and their number can be used as a metric for measuring the angle. See Fig. 8b.



(a) Time-integrated intensity vs. detector angular position of a pulse reflected from a corner.



(b) A large number of curves, such as the curves in Fig. 8a, for a wide range of wall angles, are packed together to give time-integrated intensity vs. detector-location vs. wall angle. X-axis: detector location in degrees. Y-axis: wall direction in degrees.

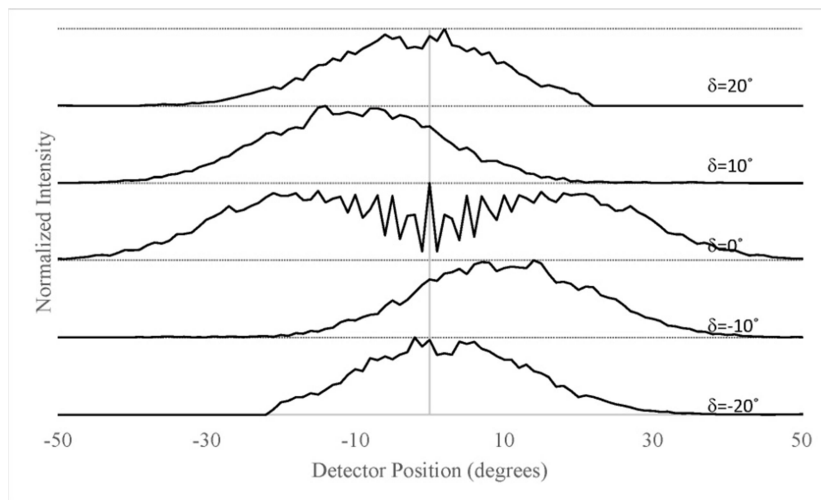
FIG. 8. Effect of a corner on the shape of a reflected wavefront.

Measuring an Angle Twist

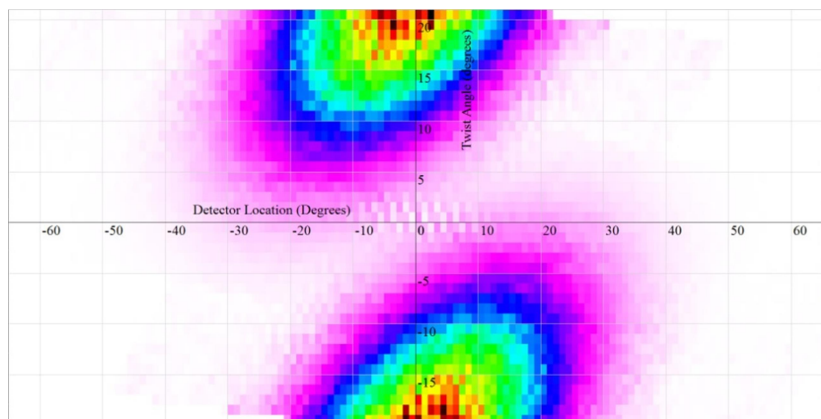
If the incident pulse does not divide a corner into halves, the two reflected wavefronts will not be symmetric. This will result in either two separate wavefronts with different angular locations and relative intensities, as in Fig. 9, or two overlapping wavefronts with strong interference patterns, as in Fig. 10.

The strong interference patterns shown in Fig. 10 can be useful, not only in mapping an area, but also in positioning objects. For example, a tiny angular object can be mounted on a plane surface that needs to be positioned accurately. By counting the number of ultrasonic fringes that pass while rotating the object, one can measure

an angular position change in tenths of degrees. This can be very useful in situations where an accurate positioning is required, but a direct angle measurement is not feasible. This idea is similar to the way in which Fabry–Perot interferometers are used in optics to position objects linearly accurately, except that it is being done here for angular positioning with a wavelength that is more practical for many applications such as robotics. For example, a 40kHz ultrasonic source can be used to position objects as accurately as 0.1° . This accuracy can be enhanced by using a source with a higher frequency.

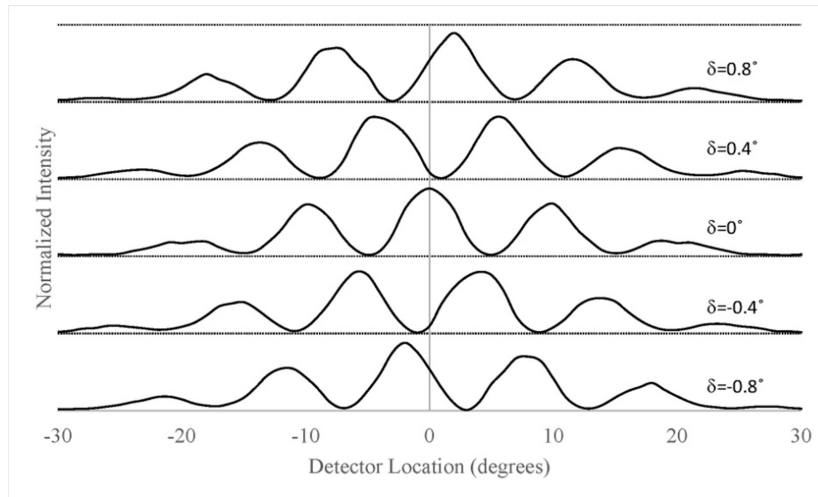


(a) Time integrated intensity vs. angular detector position of a reflection from 135° corner twisted by an angle δ . $\delta = 0$ means that the incident pulse direction divides the corner into halves.

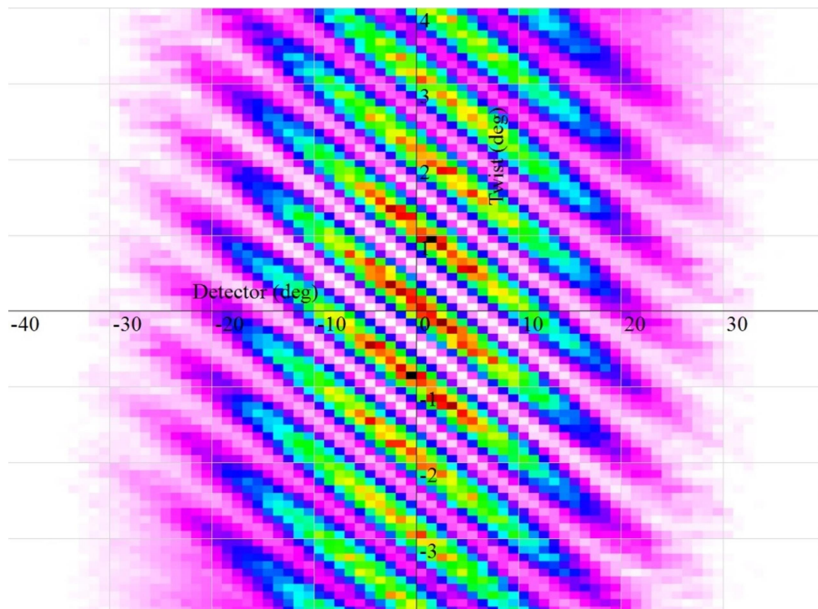


(b) A large set of curves, such as those in Fig. 9a, packed in a single 3D plot. X-axis: detector location in degrees. Y-axis: twist angle in degrees. The normalized intensity is represented by the color scale to the right of each figure.

FIG. 9. Effect of changing a 135° corner pointing direction on the reflected wavefront shape.



(a) Time-integrated intensity vs. angular detector position of a reflection from 169° corner twisted by an angle δ . $\delta = 0$ means that the incident pulse direction divides the corner into halves.



(b) A large set of curves, such as those in Fig. 10a, packed in a single 3D plot. X-axis: detector location in degrees. Y-axis: twist angle in degrees. The normalized intensity is represented by the color scale to the right of each figure.

FIG. 10. Effect of changing a 169° corner pointing direction on the reflected wavefront shape.

Seeing Behind a Corner

Observing changes in the reflected wavefront properties is not limited to objects with a direct line of sight. An object hidden behind a corner can still be detected by analyzing the waves reflected from an adjacent wall. To demonstrate this, Figs. 12a and 12b show the echoes coming out of empty hallways that are 150 cm and 200 cm long, respectively. The outgoing pulse source is placed close to the entrance without having a direct line of sight into it. The time-spacing and number of wavefronts in the train of echoes coming out gives the hallway depth and width. A robot with a digital signal processor (DSP) can

detect these simple features and guess the shape of that environment after getting some artificial intelligence training.

Objects in real life do not always have simple geometries. However, a given object will change a reflected pulse in a specific way. In other words, a complicated object will have its signature in the reflected wavefronts. To demonstrate this, an object that consists of two overlapping squares with one of them rotated 45° is placed inside the 200 cm long hallway. The reflections coming out, after placing the object 100 cm and 150 cm inside the hallway, are shown in Figs. 13a and 13b, respectively. Note

that the signature of the unseen object, marked in the figures, is the same for both cases. Note also how the echoes that are a characteristic of the hallway itself at the upper left corner of Fig. 12b

are still there in Fig. 13. One can get the information about the object itself and still get the hallway dimensions.

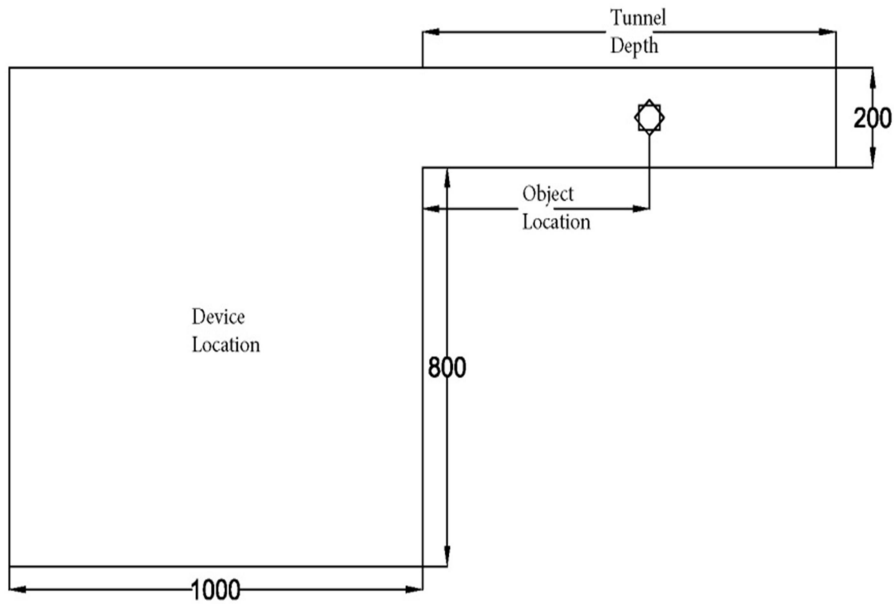
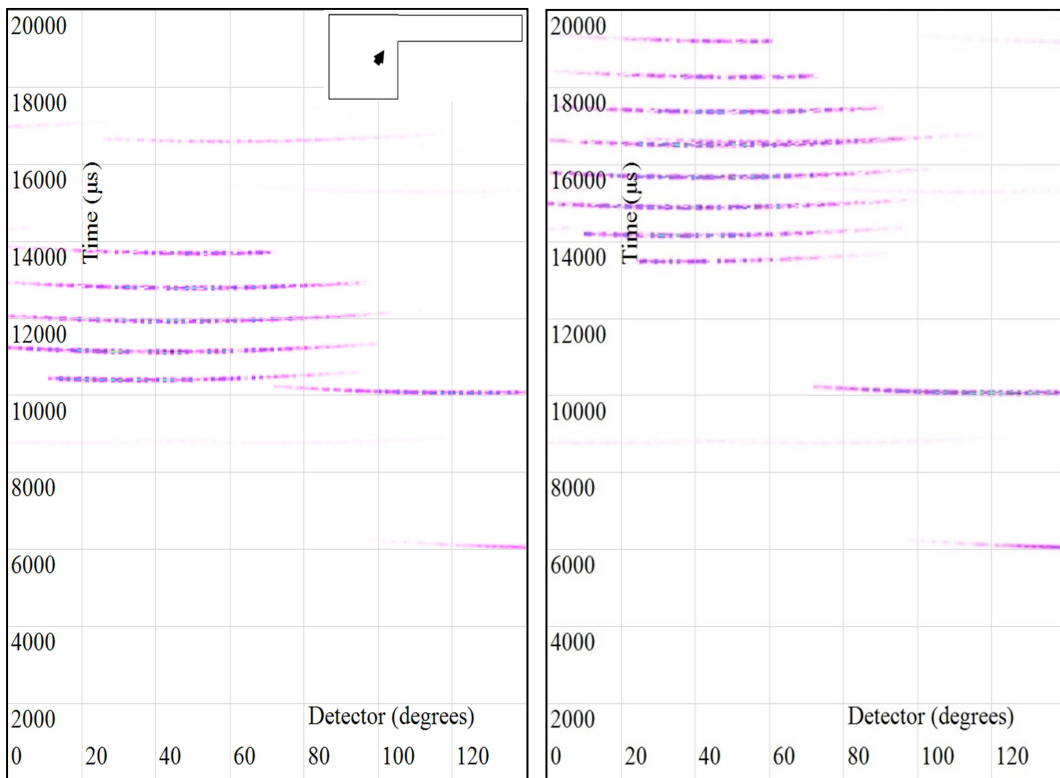


FIG. 11. Environment walls used to collect the simulated data shown in Figs. 12 and 13.



(a) Echoes coming out of a 150 cm deep hallway. (b) Echoes coming out of a 200 cm deep hallway.

FIG. 12. Train of echoes coming out of a hallway, after emitting a pulse into it, without a direct line of sight into the hallway. The inset at the upper right corner of Fig. 12a describes the geometry of the walls under study. The test environment is similar to the one shown in Fig. 11, but without the test object placed inside the tunnel.

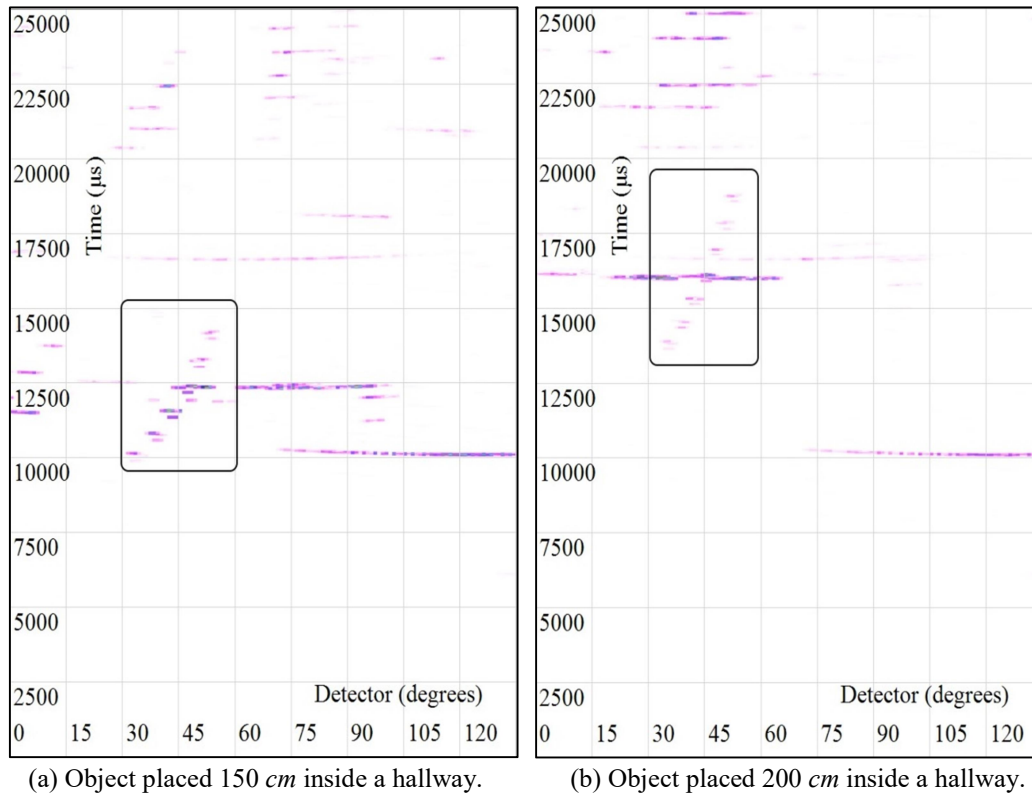


FIG. 13. Signature of an object that consists of two overlapping squares with one of them rotated 45° , placed inside a hallway, without a direct line of sight. Test environment design is shown in Fig. 11.

Conclusion

In this paper, a new method for mapping an environment and discovering unseen objects is demonstrated. This was achieved by sending a pulse with a known shape and listening to the reflections from all directions in real time. The changes in the shape of the reflected wavefronts

enable detecting simple features, such as a slope, an angle or a twist in a corner. The ability to measure object rotation, with an accuracy as high as 0.1° , by counting ultrasound interference fringes and the ability to discover unseen objects behind a corner, are demonstrated.

References

- [1] Hinderer, M., Friedrich, P. and Wolf, B., *Robotics and Autonomous Systems*, 94 (2017) 219.
- [2] Dairi, A., Harrou, F., Senouci, M. and Sun, Y., *Robotics and Autonomous Systems*, 100 (2018) 287.
- [3] Padgett, J. and Campbell, M., *Robotics and Autonomous Systems*, 98 (2017) 292.
- [4] Urena, J., Mazo, M., Garcia, J.J., Hernandez, A. and Bueno, E., *Robotics and Autonomous Systems*, 29 (4) (1999) 269.
- [5] Martinez, M. and Benet, G., *Sensors*, 10 (12) (2010) 10683.
- [6] Benet, G., Martinez, M., Blanes, F., Perez, P. and Sim'ó, J.E., *Robotics and Autonomous Systems*, 50 (1) (2005) 13.
- [7] Popelka, M., Struska, J. and Struska, M., *International Journal of Circuits, Systems and Signal Processing*, 10 (2016) 82.
- [8] Christopher, T. C., M.A. Thesis, University of Illinois at Urbana-Champaign, (2012), USA.
- [9] Ding, T., Hu, H., Bai, C., Guo, S., Yang, M., Wang, S. and Wan, M., *Ultrasonics*, 69 (2016) 166.
- [10] Khan, M.A., Jilani, S.Z., Menouar, H. and Al-Majed, A.A., *Ultrasonics*, 39 (5) (2001) 321.

- [11] Ding, T., Zhang, S., Fu, Q., Xu, Z. and Wan, M., *Ultrasonics*, 54 (1) (2014) 147.
- [12] Woodward, B. and Sharp, H., *Ultrasonics*, 29 (5) (1991) 381.
- [13] Zelenyak, A.-M., Schorer, N. and Sause, M.G.R., *Ultrasonics*, 83 (2018) 103.
- [14] Boltryk, P., Hill, M., Keary, A., Phillips, B., Robinson, H. and White, P., *Ultrasonics*, 42 (1-9) (2004) 473.
- [15] Gao, W. and Hinders, M.K., *Robotics and Autonomous Systems*, 53 (2) (2005) 89.
- [16] Dokmanic, I., Parhizkar, R., Walther, A., Lu, Y.M. and Vetterli, M., *Proceedings of the National Academy of Sciences*, 110 (30) (2013) 12186.
- [17] Dokmanic, I., Lu, Y.M. and Vetterli, M., In: *Acoustics, Speech and Signal Processing (ICASSP)*, IEEE, (2011) 321.
- [18] Crocco, M., Trucco, A., Murino, V. and Del Bue, A., In: *Signal Processing Conference (EUSIPCO), Proceedings of the 22nd European IEEE*, (2014) 910.
- [19] Lazik, P., Rajagopal, N., Shih, O., Sinopoli, B. and Rowe, A., In: *Proceedings of the 13th ACM Conference on Embedded Networked Sensor Systems*, ACM, (2015) 73.
- [20] Shih, O. and Rowe, A., In: *Proceedings of the ACM/IEEE Sixth International Conference on Cyber-Physical Systems*, ACM, (2015) 149.
- [21] Al-Shorman, M. and Al-Kofahi, M., *International Journal of High-performance Computing Applications*, 33 (5) (2019) 1019.

The Collision-Induced Absorption Spectra of Hydrogen Complexes in the Second Overtone Band

M. Abu-Kharma^a, Mahmoud H. Saleh^a, Z. M. Elimat^b and W. J. Kadhem^b

^a Department of Physics, Faculty of Science, Al-Balqa Applied University, Al-Salt 19117, Jordan.

^b Department of Physics and Basic Sciences, Faculty of Engineering Technology, Al-Balqa Applied University, Amman 11134, Jordan..

Received on: 03/02/2019;

Accepted on: 16/4/2019

Abstract: The second overtone band (3-0) of pure hydrogen spectra at different temperatures and hydrogen gas densities is reviewed with particular emphasis on the most recent theoretical and experimental results. Different experimental and theoretical techniques were used to record and calculate the second overtone band profiles. The calculated theoretical binary and ternary absorption coefficients are in good agreement with experimental values obtained. Different line shapes were used to fit the experimental profiles. The fitting values are tabulated in the references therein. The goal of this article is to draw the attention of the absorption spectroscopy community to the fact that there have been only a few investigations on the latter subject on the second overtone band (3-0) on hydrogen, even though the investigations on the other bands are quite abundant.

Keywords: Collision-induced spectroscopy, Infrared absorption, CIA, IR spectra, H₂, Second overtone band, Line shape functions, Roto-vibrational state.

PACS: 33.15.Mt, 33.20.a, E33.20.Vq

Introduction

There has been substantial interest in the study of the hydrogen spectra driven by the fact that the hydrogen molecule is the simplest of all diatomic molecules. Further, hydrogen is the most abundant element in the atmospheres of the planets and stellar objects and constitutes about 75% of all matter in the universe. Indeed, the collision mechanism of H₂-H₂ yields the associated thermal emission and absorption spectra. Within this context, the second overtone band of hydrogen is important for studies of both planetary and stellar atmospheres [1-8] and appears between the visible and the near-infrared spectral region, approximately between 11000 and 13800 cm⁻¹. The properties of this band have not been precisely delineated due to the weakness of absorption and the experimental difficulties encountered in its investigation. It

consists of the short-range electron-overlap interaction and the long-range quadrupole induced transitions of the types:

(a) single transitions $(3 \leftarrow 0) Q_3(J) + Q_0(J), S_3(J) + Q_0(J)$ and $Q_3(J) + S_0(J)$,

(b) double transitions $[(2 \leftarrow 0) + (1 \leftarrow 0)] Q_2(J) + Q_1(J), S_2(J) + Q_1(J), Q_2(J) + S_1(J)$ and $S_2(J) + S_1(J)$, and

(c) triple transitions $[(1 \leftarrow 0) + (1 \leftarrow 0) + (1 \leftarrow 0)] Q_1(J) + Q_1(J) + Q_1(J)$,

where the subscripts 0,1,2 and 3 indicate Δv , the change in the vibrational quantum number and J indicates the rotational quantum number.

The collision-induced absorption spectrum (CIA) arises from transient electric dipole moments that exist during binary, ternary and

higher-order collisions. Three mechanisms contribute to the induction of an electric dipole moment: (a) the polarization of one hydrogen molecule in the multipolar field of another hydrogen molecule, (b) electron exchange in the H_2 - H_2 molecule at near range and (c) the dispersion interaction. When the transient induced-dipole moments interact with the electromagnetic field from an infrared radiation source, the colliding molecules absorb infrared radiation in the spectral regions corresponding to roto-vibrational, pure rotational and translational states. The major properties of the absorption lines in this case are: (a) the line widths are large, typically 10 - 50 cm^{-1} ; (b) the absorption profiles and the integrated absorption coefficients $\int \alpha(\nu) d\nu$ are proportional to the square and the cube of the density for pure gases in the case of binary and ternary collisions, respectively; (c) the integrated intensity of the band is temperature-dependent and (d) a dip at $Q_3(1)$ with characteristic low and high wavenumber components Q_P and Q_R is observed which is temperature-dependent.

There have been many theoretical and experimental investigations on the CIA of the second overtone band of hydrogen at different temperatures [1-20]. Initially, Herzberg identified a diffuse feature at 12093 cm^{-1} , observed in the spectra of Uranus and Neptune by Kuiper earlier, as the collision-induced $S_3(0)$ line of the second overtone band of H_2 [2].

Later, Herzberg photographed the second overtone band of H_2 at a gas pressure of 100 atm at 78K with a path length of 80 m. Herzberg interpreted the spectrum as consisting of a pure second overtone band, in which one of the two colliding molecules makes a vibrational transition $\Delta\nu = 3$ such as: $Q_3(J) + Q_0(J)$ and a double vibrational band in which one molecule makes a vibrational transition $\Delta\nu = 2$, while the second molecule makes a vibrational transition $\Delta\nu = 1$, such as: $Q_1(J) + Q_2(J)$, $Q_1(J) + S_2(J)$ and $Q_2(J) + S_1(J)$ [3]. Subsequently, Hunt recorded the same band at room temperature and pressures up to 2200 atm [4].

A few years later, Mckellar and Welsh recorded the second overtone band spectra of H_2 at gas densities of about 37 amagat ($1\text{ amagat} = 44.614981\text{ mol/m}^3$) at 85 K with a path length of 137m. Their analysis of the absorption profiles showed several discrepancies between the experimental and calculated profiles. They

suggested that these discrepancies arise because of the overlap-induction contribution to the 3-0 band that has not been included in their calculations [5, 6].

Further down the road, Gillard recorded the induced spectra of H_2 and D_2 in the second overtone region at 77K and densities in the range 500-930 amagat using a 2m absorption cell. He was the first to record the second overtone band of deuterium. Further, he also interpreted the observed peaks in the spectra and calculated the binary and ternary absorption coefficients of the measured integrated absorption. But, he met some difficulties in the analysis of the CIA spectra due to lack of information on the available values of the quadrupole-moment matrix elements, polarizability and anisotropy of the polarizability of H_2 and D_2 [7].

Fan Xiang recorded the absorption spectra of the second overtone region of H_2 for gas densities up to 1000 amagat at 77, 201 and 298 K using a 2m absorption cell. He observed a dip at $Q_3(1)$ with characteristic low and high wavenumber components Q_P and Q_R . The dip occurs due to the short-range electron-overlap interaction of the collisions of the second overtone band. Good agreement between the experimental and calculated absorption profiles has been obtained by reducing the matrix elements of the quadrupolar moment $\langle 0J|Q|v'J' \rangle$ for the first and second overtone band by a factor of 0.68 [8]. Reddy et al. [9] presented the first observation of simultaneous vibrational transitions involving three molecules in CIA spectra. They analyzed the experimental profiles resulting from triple-collision transitions using the Lorentz line-shape function as well as Birnbaum-Cohen line-shape function.

Brodbeck et al. recorded the CIA spectra of H_2 in the region of the second overtone at $0.8\mu\text{m}$ and temperatures of 298 and 77.5 K for gas densities ranging from 100 to 800 amagats. The spectra were recorded with a Fourier transform spectrometer using two high-pressure absorption cells. These authors obtained the binary absorption coefficients by extrapolating their measurements and compared the calculated binary absorption coefficients with results from *ab initio* calculations [11, 12]. More recently, Abu-Kharma [18-20] studied the second overtone bands of hydrogen and deuterium at different temperatures for gas densities up to 1000 amagat. Also, the binary and ternary

absorption coefficients have been determined. Satisfactory agreement between the calculated and the recorded profiles has been observed.

Many methods have been used to calculate the spectral lines of the second overtone band [7-19]. In parallel to experimental research, theoretical investigations took place, such as those following. Yi Fu et al. conducted a quantum mechanical computation of the collision-induced roto-vibrational absorption spectra of hydrogen in the second overtone band [13]. Borysov et al. presented a semi-empirical numerical method to compute the binary collision-induced roto-vibrational absorption spectra of hydrogen molecules in the second overtone band of hydrogen, at temperatures from 50 to 500 K [14]. They compared their semi-empirical model with the CIA spectra of normal hydrogen for the second overtone band at 77.5 K and 298 K measured by Brodbeck et al. [15]. Brodbeck et al. studied the CIA spectra in the second overtone region at ambient and liquid nitrogen temperatures. They found good agreement between the experimental and calculated binary absorption coefficients [11, 12]. Abel studied the CIA in the roto-translational band of H₂-H₂ and in the fundamental, first and second overtone bands of H₂ in dense hydrogen gas. He compared the existing measurements of the latter overtones of H₂ with *ab initio* calculations based on new dipole and potential energy surfaces. Over the full range of frequencies considered, the agreement between theoretical calculations and measurements is remarkable. His method can reproduce the measured spectra with high accuracy [16]. Abel et al. [17] computed the binary absorption coefficients at wavelengths near 5 μm at temperatures of 77.5 and 297K based on an *ab initio* interaction-induced dipole surface of collisionally interacting molecular hydrogen pairs H₂-H₂ and compared their results with an existing laboratory measurement.

Moraldi and Frommhold [10] studied the triple transition Q₁(J₁) + Q₁(J₂) + Q₁(J₃) near 12466 cm⁻¹ in compressed hydrogen. They used the model of the overlap-induced, irreducible, ternary dipole component of three interacting H₂ molecules to calculate the intensity of the triple Q₁ transition observed by Reddy et al. [9] in pure hydrogen gas near 12466 cm⁻¹. The calculated intensities agree with measurements within a factor of 2 or 3.

In the present paper, we present the collision-induced absorption spectra of H₂-H₂ with emphasis on the second overtone band. Also, we include the most recent experimental and theoretical results.

Experimental and Theoretical Details

The pressure cells used in the CIA experiments are constructed of polished stainless steel and equipped with sapphire windows. The lengths of the cells are 300.5 cm, 215.25 cm [11, 12], 194.2 cm, 194.5cm, 194.8cm [7,8]. Further, an absorption optical path of 80m or 137m length has been obtained with a cell 3.5 m long [5].

The spectra are recorded using different spectrometers:

- 1- A Perkin-Elmer model 112G single beam double pass grating spectrometer equipped with a plane grating of 300 lines/mm. The spectral resolution is ~2cm⁻¹ at 11782 cm⁻¹.
- 2- A Bruker IFS 66V FT spectrometer with a resolution of 0.5 cm⁻¹.

The infrared source of radiation is a General Electric FFJ 600 W quartz line projection lamp housed in a water-cooled brass jacket.

Different detectors suitable and sensitive to the second band region have been used:

- 1- A Hammamatsu model R758 photomultipliers tube.
- 2- A Si diode running at room temperature.

For more experimental details, the reader is referred to the references therein.

Binary and Ternary Absorption Coefficients

The absorption coefficient $\alpha(\nu)$ of a pure gas at a given wavenumber ν is:

$$\alpha(\nu) = \frac{1}{l} \ln \left[\frac{I_0(\nu)}{I(\nu)} \right] \quad (1)$$

where $I_0(\nu)$ is the transmitted intensity of the radiation source through an evacuated cell of optical path length l and $I(\nu)$ is the transmitted intensity through the cell which contains the absorbing pure gas at a given density ρ (amagat). The dimensionless absorption coefficient reads:

$$\tilde{\alpha}(\nu) \equiv \frac{\alpha(\nu)}{\nu} \quad (2)$$

which is given by:

$$\tilde{\alpha}(\nu) = \sum_m n \frac{\tilde{\alpha}_{nm}^0 W_n(\Delta\nu)}{1 + e^{(-hc\Delta\nu/kT)}} \quad (3)$$

where n stands for the induction mechanism and $n = ov, q$ or h are overlap, quadrupolar or hexadecapolar induction, respectively, m represents a specific transition arising from a given mechanism, $\tilde{\alpha}_{nm}^0$ is a parameter equal to twice the maximum absorption coefficient at the frequency ν_m and $W_n(\Delta\nu)$ with $\Delta\nu = \nu - \nu_m$ represents the line shape function of the n type. The factor $[1 + e^{(-hc\Delta\nu/kT)}]$ satisfies the detailed balance condition and converts the symmetric into asymmetric line shape function.

The integrated absorption coefficient for the pure gas is given by:

$$\int \alpha(\nu) d\nu = \alpha_1 \rho^2 + \alpha_2 \rho^3 + \dots \quad (4)$$

where α_1 and α_2 are the binary and ternary absorption coefficients. Eq. (4) can be rewritten in the form:

$$(1/\rho^2) \int \alpha(\nu) d\nu = \alpha_1 + \alpha_2 \rho + \dots \quad (5)$$

The plot of $(1/\rho^2) \int \alpha(\nu) d\nu$ versus ρ gives a straight line of slope α_2 and an interception of α_1 . The integrated binary absorption coefficient due to quadrupole induction for a given band is given by Poll [21]:

$$\tilde{\alpha}_{qm} = \frac{1}{\rho^2} \int \frac{\alpha_m(\nu)}{\nu} d\nu = \frac{4e^2\pi^2}{3hc} n_0^2 a_0^5 \left(\frac{a_0}{\sigma}\right)^5 \tilde{J}_2 X_{2m} \quad (6)$$

where

$$X_{2m} = \sum P_{j_1} P_{j_2} \left[\begin{array}{l} C(J_1 2J'_1; 00)^2 \langle V_1 J_1 | Q_{21} | V'_1 J'_1 \rangle^2 \\ C(J_2 0J'_2; 00)^2 \langle V_2 J_2 | \alpha_2 | V'_2 J'_2 \rangle^2 \\ + C(J_2 2J'_2; 00)^2 \langle V_2 J_2 | Q_{21} | V'_2 J'_2 \rangle^2 \\ C(J_1 0J'_1; 00)^2 \langle V_1 J_1 | \alpha_1 | V'_1 J'_1 \rangle^2 \end{array} \right] + Y_{2m} \quad (7)$$

and

$$\tilde{J}_2 = 12\pi \int_0^\infty x^{-6} g_0(x) dx. \quad (8)$$

where e is the charge of an electron, $n_0 = 2.387 \times 10^{19}$ molecules/cm³ is Loschmidt's number, a_0 is the Bohr radius and σ is the intermolecular separation corresponding to the intermolecular potential $V(\sigma) = 0$, $\langle v_j | Q_2 | v'j' \rangle$ is the matrix element for the quadrupole induction, $\langle v_j | \alpha | v'j' \rangle$ is the matrix element of the isotropic polarizability, $g_0(x)$ is the pair correlation function for the gas, $x = R/\sigma$, R being the intermolecular separation and the numbers 1 and 2 refer to the two colliding molecules. P_j stands for the normalized Boltzmann factors:

$$P_J = \frac{g_T(2J+1)e^{(-E_J/kT)}}{\sum_J g_T(2J+1)e^{(-E_J/kT)}} \quad (9)$$

with g_T being the nuclear statistical weight of the molecule in each rotational state, E_J is the rotational energy and g_T is 1 and 3 for the even and odd J , respectively, for H₂. $C(JLJ'; 00)$'s are Clebsch-Gordan coefficients, the values of which are given by Rose [25]. The Y_{2m} term is small compared to X_{2m} and accounts for the contribution of the anisotropy of polarizability of the quadrupole transitions.

The Line Shape Function

The line shape function in Eq. (3), $W_n(\Delta\nu)$ for the overlap transition is represented by:

$$W_{ov}(\Delta\nu) = \left[\left(\frac{2\Delta\nu}{\delta_d} \right)^2 K_2 \left(\frac{2\Delta\nu}{\delta_d} \right) \right] \left[1 - \gamma \left\{ 1 + \left(\frac{\Delta\nu}{\delta_c} \right)^2 \right\}^{-1} \right] \quad (10)$$

It is formed of two parts: the intra-collisional line shape function (Levine-Birnbaum shape function) and the inter-collisional line shape function [26], where K_2 is the modified Bessel function of the second kind, δ_d is the intra-collisional half-width at half-height, γ is a constant that equals one unit yields zero absorption at the dip at ν_m and δ_c is the inter-collisional half-width at half-height equal to $(1/2\pi c\tau_c)$, where τ_c is the mean time between collisions.

The line shape function for the quadrupolar transitions is given by:

(a) the dispersion-type function:

$$W_q(\Delta\nu) = \frac{1}{1 + \left(\frac{\Delta\nu}{\delta_q} \right)^2} \quad (11)$$

where δ_q is the quadrupolar half-width at half-height. Gillard [7] modeled quadrupolar transitions with a modified dispersion line-shape function:

$$W_q(\Delta\nu) = \frac{1}{1 + \left(\frac{\Delta\nu}{\delta_{q1}} \right)^2 + \left(\frac{\Delta\nu}{\delta_{q2}} \right)^4} \quad (12)$$

where the fourth-power term better reproduces the spectrum.

(b) The Birnbaum-Cohen (BC) line shape function is given by:

$$W_q^{BC}(\Delta\nu) = \frac{1}{2\pi^2 c \delta_1} \exp\left(\frac{\delta_1}{\delta_2}\right) \exp\left(\frac{hc\Delta\nu}{2kT}\right) \frac{zK_1(z)}{1+(\Delta\nu/\nu)} \quad (13)$$

where

$$z = [1 + (\Delta\nu\delta_1)^2]^{1/2} \left[\left(\frac{\delta_1}{\delta_2}\right)^2 + \left(\frac{hc\delta_1}{2\pi kT}\right)^2 \right]^{1/2} \quad (14)$$

$\Delta\nu = \nu - \nu_m$, $K_1(z)$ is a modified Bessel function of the second kind of order 1, $\delta_i = 1/2\pi c\tau_i$ is a wavenumber parameter and τ_i is a characteristic time in the dipole moment correlation function. Lewis [22] modified the BC line-shape with a new one referred to as the Lewis-Birnbaum-Cohen (LBC) line-shape which is given by:

$$W^{LBC}(\Delta\omega) = \frac{2}{1+e^{-\beta h\Delta\omega}} \frac{e^{\tau_2/\tau_1}}{\pi} \frac{\tau_2}{\sqrt{1+\Delta\omega^2\tau_1^2}} K_1\left(\sqrt{1+\Delta\omega^2\tau_1^2} \frac{\tau_2}{\tau_1}\right) \quad (15)$$

where $\Delta\omega = \omega - \omega_m + \omega_s$, with ω_m being the frequency of the m^{th} transition ($\omega = c/\nu$). The LBC line-shape function is derived from the BC line-shape function with a slight modification of the procedure used. Beside the semi-line-shapes discussed earlier, there are:

- (a) A semi-empirical numerical method to calculate the binary collision-induced roto-vibrational absorption spectra of $\text{H}_2\text{-H}_2$ complexes in the second overtone region of hydrogen at temperatures from 50-500 K. The numerical procedure uses simple analytical model line-shapes and can generate the roto-vibrational CIA spectra of hydrogen pairs easily [14].
- (b) Quantum line-shape functions which are derived from quantum mechanical computations of the roto-vibrational CIA spectra of $\text{H}_2\text{-H}_2$ in the second overtone band [13].

Results and Discussion

Summary of Experimental Work

Illustrative examples of CIA spectra of the $\text{H}_2\text{-H}_2$ second overtone band in the pure gas at 77, 86, 201 and 298 K are shown in Figs. (1-4). Fig. 5 represents absorption profiles of the second overtone band of gaseous $\text{H}_2\text{-H}_2$ at 77, 201 and 298K obtained with a two-meter cell. Also, typical absorption profiles of deuterium in the pure gas at 77K and densities 685, 830 and 929 amagat in the second overtone region are shown in Fig. 6 by a plot of $\text{Log}[I_0(\nu)/I(\nu)]$

versus the wave number $\nu(\text{cm}^{-1})$. The recorded profiles mainly consist of the overlap component which occurs due to the short-range electron-overlap interaction of the collisions and the long-range quadrupole-induced transitions of the single, double and triple transitions. The possible quadrupolar and overlap transitions which contribute significantly to the absorption at different temperatures are listed in Table 1. These transitions are calculated from the constants of the free hydrogen molecules (Foltz et al. for $\nu=3$ and Bragg et al. for $\nu=0,1$ and 2 [23,24]).

Several features of these profiles are worth mentioning. First, the appearance of a characteristic dip in the $Q_3(J)$ lines with its low and high wave-number maxima Q_P and Q_R . The separation between Q_P and Q_R increases with density and becomes more obvious at room temperature. Further, the dip position is shifted to high wave-numbers with increasing density. The sharp absorption dip occurs due to the inter-collisional interference effect which arises from the negative correlations existing between the short-range overlap of dipole moments induced in successive collisions [26]. It appears that either the overlap induction is active in the 1-0, 3-0, 5-0, ... etc. bands and absent in the 2-0, 4-0, 6-0, ... etc. bands; or it is absent for some reason only in the first overtone band [5]. In the future, we shall seek to find an explanation for the latter absence. The line width increases with temperature. Second, the spectral band profiles defined by $[1/l\rho^2] \text{Ln}(I_0)/I$ vary significantly with the gas density ρ [12]. The increase of $\alpha(\nu)$ with the density, observed in the region 12400-12600 cm^{-1} , may be partially arising from the contribution of the ternary transitions. Third, the quadrupolar lines in the second overtone profiles appear to be somewhat narrower than the corresponding lines in the fundamental and first overtone bands. This is attributed to the diffusional narrowing which occurs at high densities used to record the second overtone region. Fourth, the recorded profile at 86 K shows no dip in the $Q_3(J)$ branch and only five peaks are displayed because of the low gas density used. Fifth, the number of peaks increases with decreasing temperature, as shown in Figs. 1 to 4. Absorption peak positions and the assignments of the transitions contributing to these peaks are listed in Table 2. The observed positions of the peaks 1 to 9 and their assignments are listed in Tables 1 and 2.

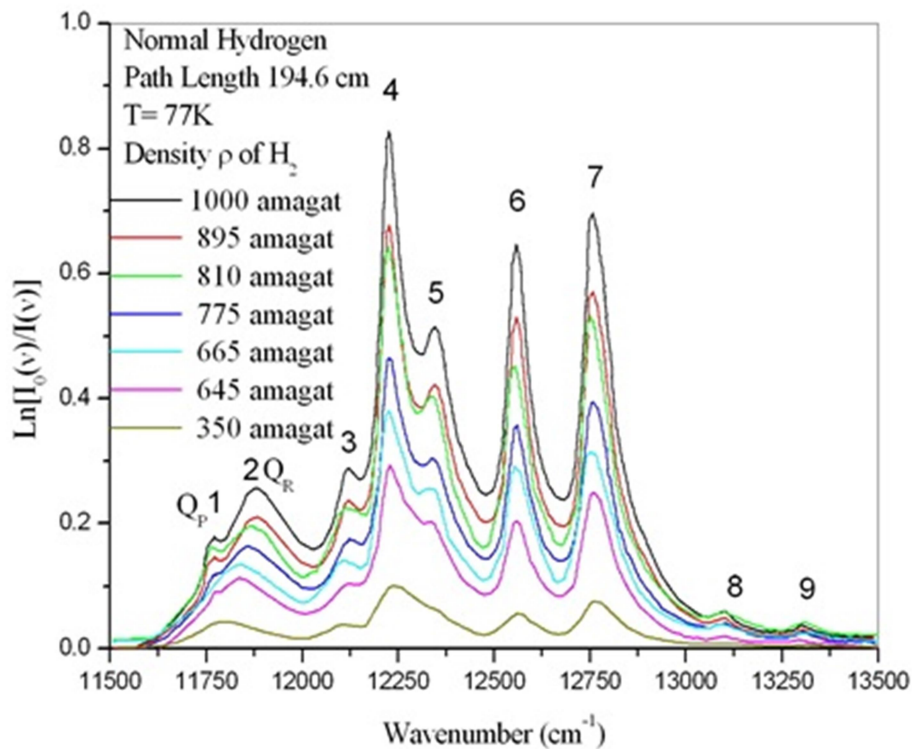


FIG. 1. Absorption profiles of the second overtone band of H_2 at 77 K with a path length of 194.2 cm.

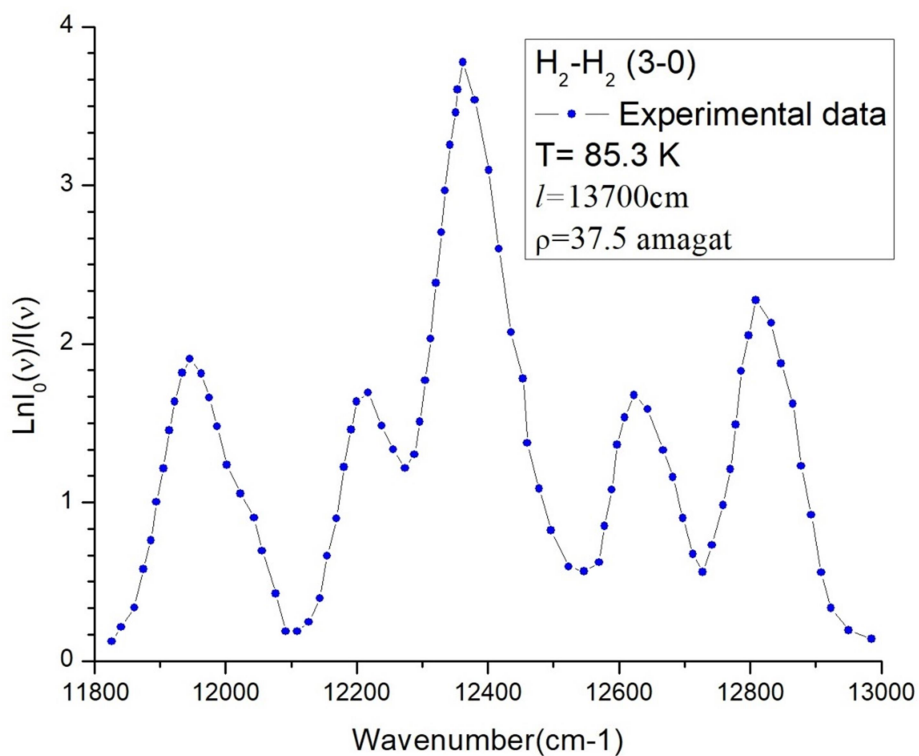


FIG. 2. Absorption profile of the second overtone band of normal hydrogen at 86 K with a path length of 137m [5].

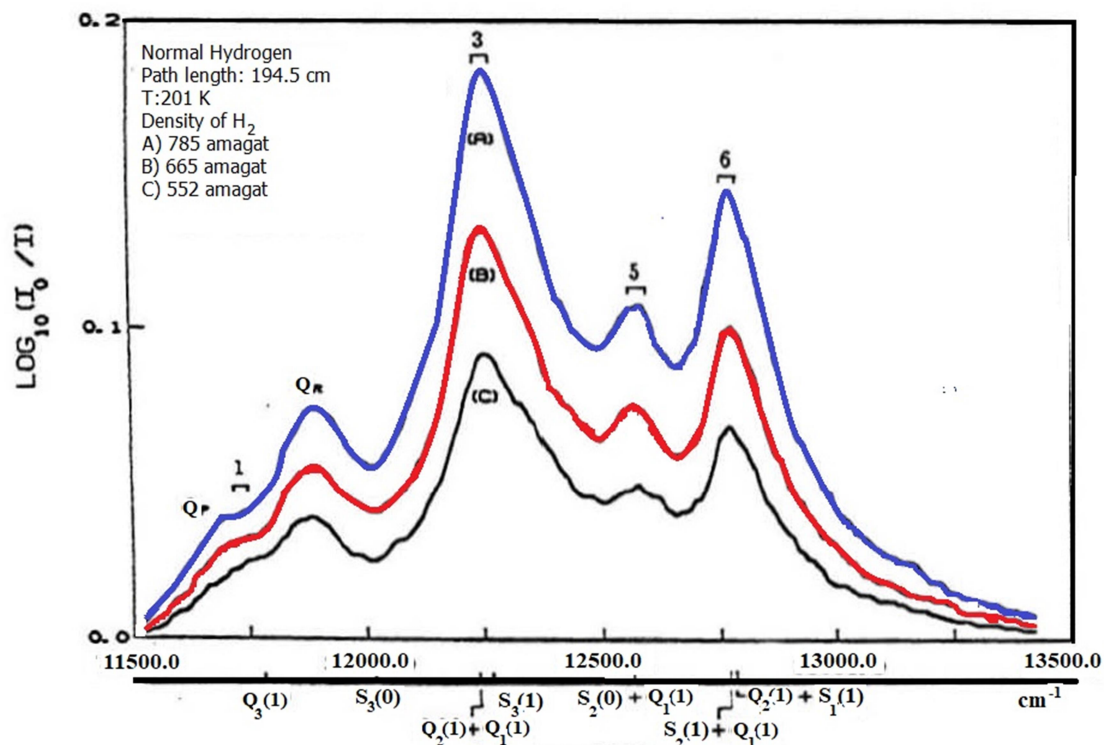


FIG. 3. Absorption profiles of the second overtone band of H₂ at 201 K with a path length of 194.5 cm.

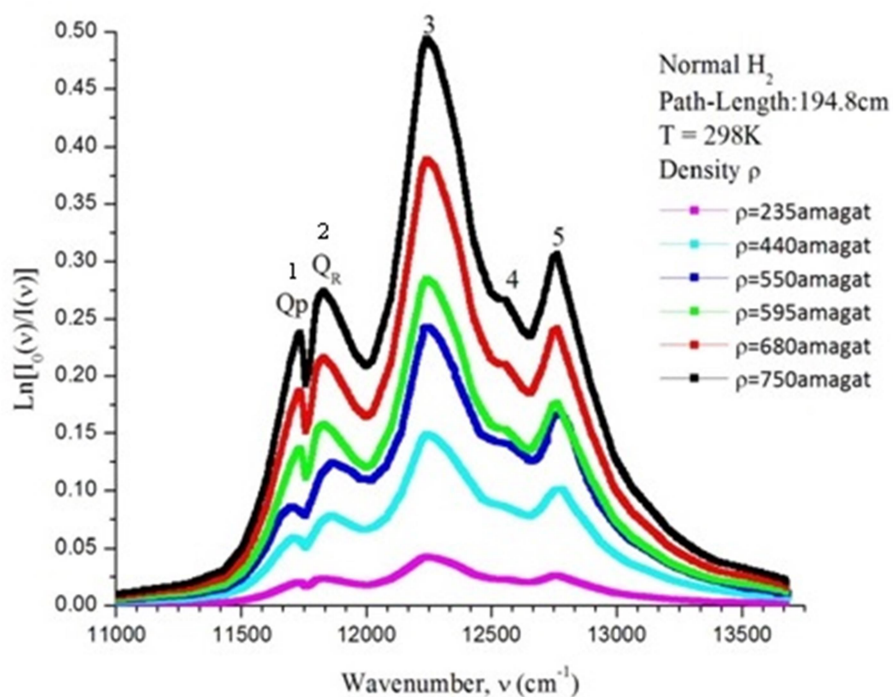


FIG. 4. Absorption profiles of the second overtone band of H₂ at 298 K with a path length of 194.8 cm.

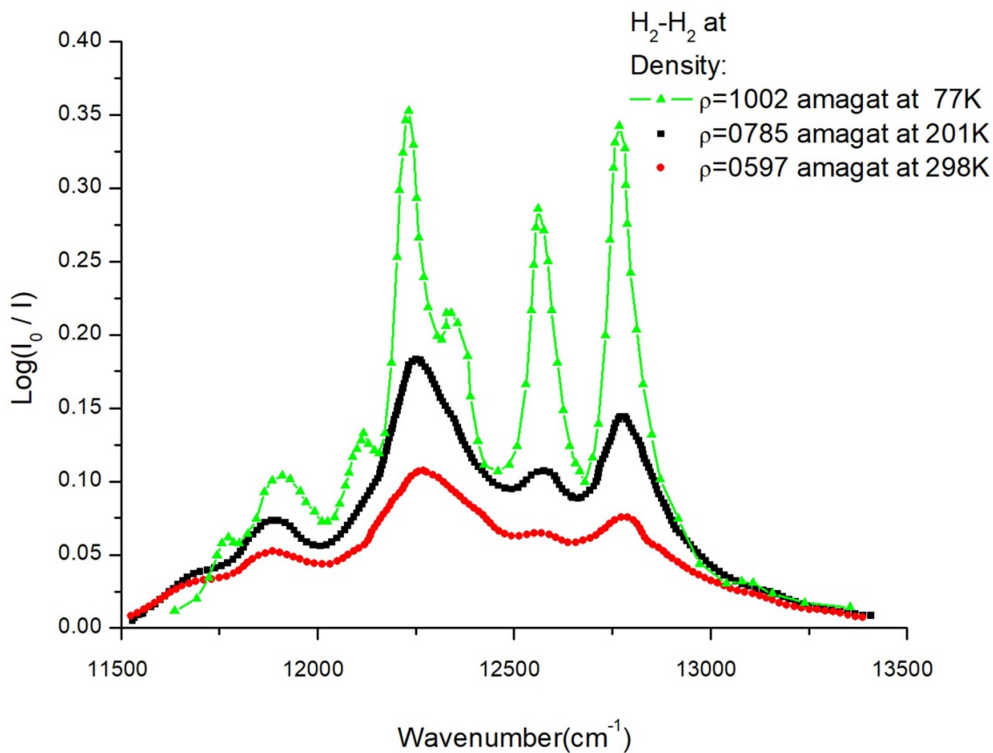


FIG. 5. Absorption profiles of the second overtone band of H₂ at 77, 201 and 298 K.

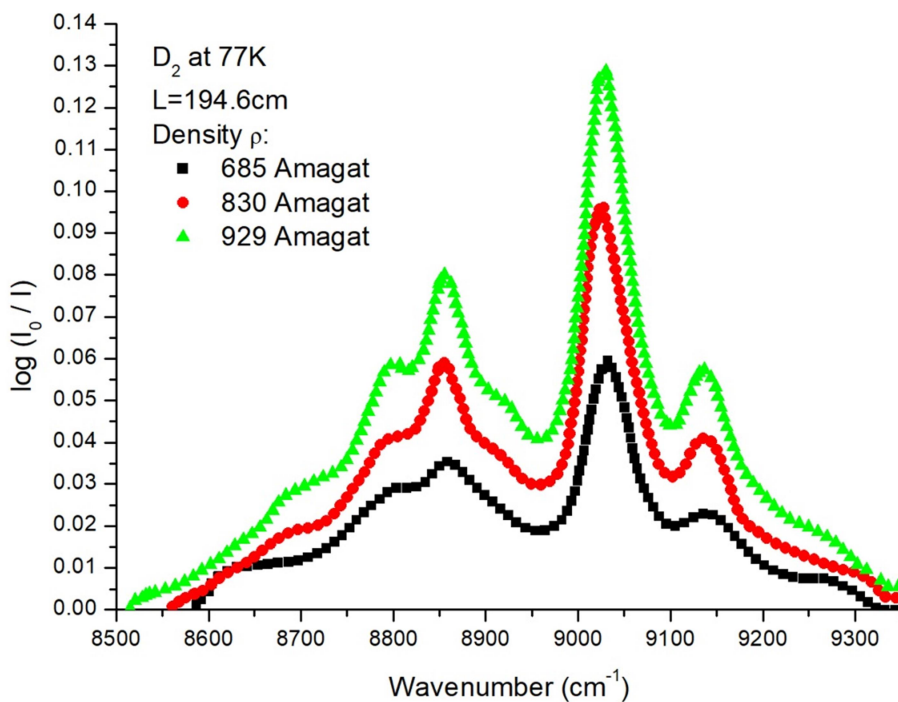


FIG. 6. Absorption profiles of the D₂ second overtone region at 77K with a path length of 194.6cm.

TABLE 1. Transitions that contribute to the (3-0) band of H₂-H₂ at different temperatures.

#	Transitions	Wavenumber (cm ⁻¹)	Number of components for different temperatures
1 Single Transitions	Q ₃ (J=0-5) + S ₀ (J=0-5)	11532-12997	4-22
	Q ₃ (J=0-5) + Q ₀ (J=0-5)	11550-11678	4-24
	S ₃ (J=0-3) + Q ₀ (J=0-5)	12085-12754	4-24
	S ₃ (J=0-3) + S ₀ (J=0-3)	12439-13595	4-13
2 Double Transitions	O ₁ (J=2-5) + S ₂ (J=0-4)	11498-12899	0-16
	S ₁ (J=0-3) + O ₂ (J=2,3)	11986-12597	0-8
	Q ₁ (J=0-5) + Q ₂ (J=0-4)	11988-12248	4-22
	Q ₁ (J=0-5) + S ₂ (J=0-5)	12480-13376	4-31
	S ₁ (J=0-5) + Q ₂ (J=0-3)	12412-13534	4-22
	S ₁ (J=0-2) + S ₂ (J=0-3)	12904-13702	4-13
3 Triple	Q ₁ (J ₁) + Q ₁ (J ₂) + Q ₁ (J ₃)	12300-12700	8
4	Overlap transition Q _{3ov} (J=0-5)	11793-11798	2-5

 TABLE 2. Assignment of the observed absorption peaks and the dip of the H₂-H₂ second overtone region.

Peak number	Wavenumber of observed peak at 77K [7,8,19]	Wavenumber of observed peak cm ⁻¹ at 201 [8]	Wavenumber of observed peak cm ⁻¹ at 85 [5,6]	Wavenumber of observed peak cm ⁻¹ at 298 [8,20]	Assignment
1	11773-11775	11732	11765-11782	11740	Q ₃ (J)+Q ₀ (J)
2	11793-11798	-	-	-	Q ₃ (J) overlap dip
3	12120	-	12085-12137	-	S ₃ (0)+Q ₀ (J), Q ₃ (J)+S ₀ (0)
4	12226-12227	12255	12230-12369	12255	S ₃ (1)+Q ₀ (J), Q ₂ (J)+Q ₁ (J)
5	12345	-	-	-	Q ₃ (J)+S ₀ (1)
6	12560-12562	12572	12568-12585	12571	S ₂ (0)+Q ₁ (J), Q ₂ (J)+S ₁ (0)
7	12760-12762	12786	12760-12800	12780	S ₂ (1)+Q ₁ (J), Q ₂ (J)+S ₁ (1)
8	13100-13107	-	-	-	S ₂ (1)+S ₁ (0), S ₂ (0)+S ₁ (1)
9	13310	-	-	-	S ₂ (1)+S ₁ (1)

The integrated absorption coefficients $\int \alpha(\nu) d\nu$ of the second overtone region are determined by integrating the areas under the experimental profiles. Fig. 7 represents a plot of $(1/\rho^2) \int \alpha(\nu) d\nu$ versus density ρ for the experimental profiles at 298, 201 and 77K. The intercept and the slope of the best straight line, which gives the values of the binary and ternary absorption coefficients, respectively, are calculated by a least-square fit of the experimental data. The binary and ternary absorption coefficients obtained by different researchers are given in Table 3.

An example of the profile analyses is shown in Fig. 8. The B-C and L-B lines were used for this purpose. We fit the Birnbaum-Cohen (BC)

line shape function to the experimental profiles. The BC function is given by:

$$W_q^{BC}(\Delta\nu) = \frac{1}{2\pi^2 c \delta_1} \exp\left(\frac{\delta_1}{\delta_2}\right) \exp\left(\frac{hc\Delta\nu}{2kT}\right) \frac{zK_1(z)}{1+(\Delta\nu/\delta_1)} \quad (16)$$

where

$$z = \left[1 + (\Delta\nu\delta_1)^2\right]^{1/2} \left[\left(\frac{\delta_1}{\delta_2}\right)^2 + \left(\frac{hc\delta_1}{2\pi kT}\right)^2 \right]^{1/2} \quad (17)$$

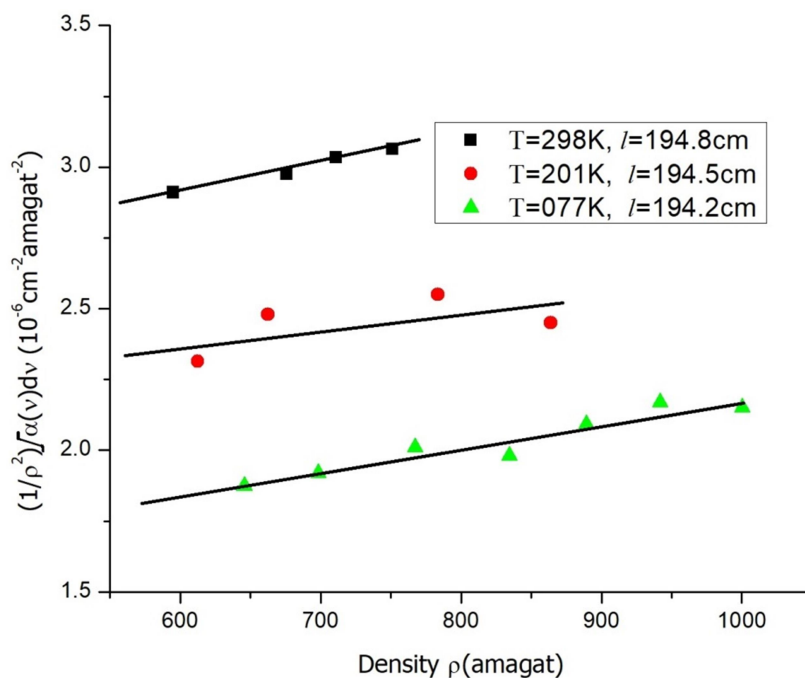


FIG. 7. $(1/\rho^2) \int \alpha(\nu) d\nu$ versus density ρ for the experimental profiles at 298, 201 and 77K.

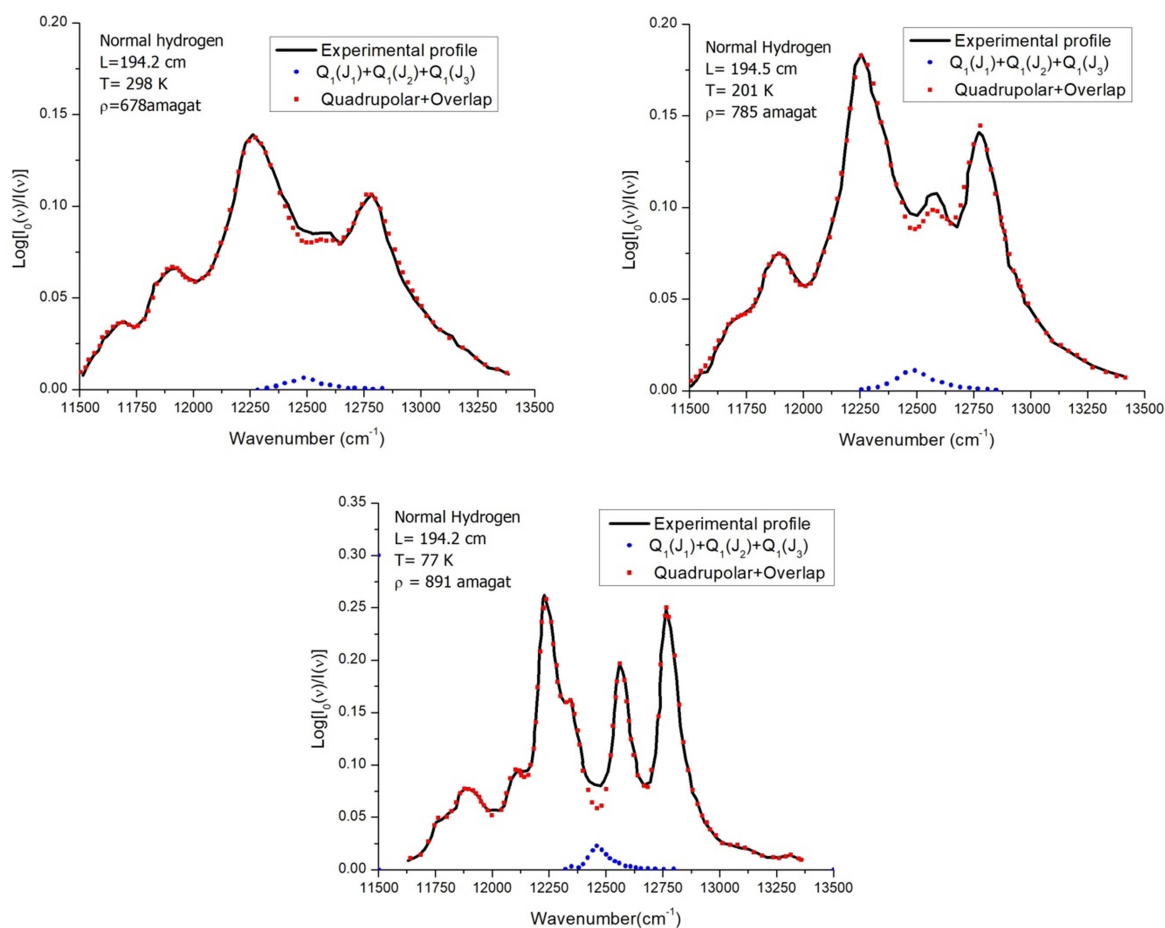


FIG. 8. Analysis of the absorption profile of the second overtone band of H_2-H_2 in the pure gas density 891 amagat at 77 K, density 785 amagat at 201 and density 678 amagat at 298K. The black curve is the experimental profile. The blue square represents the summation of single, double and overlap transitions. The curve represented by red circle around $12,460 \text{ cm}^{-1}$ is the difference between the experimental and the previous sum and is attributed to the triple transitions of the type $Q_1(J_1) + Q_1(J_2) + Q_1(J_3)$.

TABLE 3. The binary and ternary absorption coefficients of hydrogen and deuterium (experimental and theoretical values).

Temperature	Binary absorption coefficient $\alpha_1 \times 10^{-6}$ (cm ⁻² amagat ⁻²)	Ternary absorption coefficient $\alpha_2 \times 10^{-9}$ (cm ⁻² amagat ⁻³)
77K H ₂	(1.98±0.20) [19] (1.35±0.04) [8] $\tilde{\alpha}_1 = 4.53 \pm 0.3 \times 10^{-39}$ (cm ⁶ s ⁻¹) 0.86±0.06 [$\tilde{\alpha}_1 = 4.4 \pm 0.3 \times 10^{-39}$ (cm ⁶ s ⁻¹)] [7] [$\tilde{\alpha}_1 = 7.18 \times 10^{-39}$ (cm ⁶ s ⁻¹)] [7] (2.10) [11,12] (1.9) [11,12] (calculated)	0.8±0.2 [8] 0.76±0.08 [7]
85K H ₂	[$\tilde{\alpha}_1 = 5.4 \times 10^{-39}$ (cm ⁶ s ⁻¹)] [5]	
201K H ₂	2.13±0.02 $\tilde{\alpha}_1 = 7.11 \times 10^{-39}$ (cm ⁶ s ⁻¹) [8]	0.4±0.1 [8]
298K H ₂	(3.25±0.07) [20] (2.33±0.02) $\tilde{\alpha}_1 = 7.88 \times 10^{-39}$ (cm ⁶ s ⁻¹) [8] (3.14) (2.74) [11,12] (calculated)	0.9±0.3 [8]
77K D ₂	(0.17±0.05) [$\tilde{\alpha}_1 = 0.78 \pm 0.24 \times 10^{-39}$ (cm ⁶ s ⁻¹)] theory [2.14×10 ⁻³⁹] [7]	[$\tilde{\alpha}_1 = 0.32 \pm 0.06 \times 10^{-39}$ (cm ⁶ s ⁻¹)] [7]

It is applied in the case of quadrupolar, single, double and triple transitions. Also, the Levine-Birnbaum (LB) line shape function is applied for the overlap transitions and reads:

$$W_{ov} = \left(\frac{2\Delta\nu}{\delta_d} \right)^2 K_2 \left(\frac{2\Delta\nu}{\delta_d} \right) \left[1 - \frac{\gamma}{1 + \left(\frac{2\Delta\nu}{\delta_c} \right)^2} \right] \quad (18)$$

A typical CIA spectrum of H₂-H₂ in the 3-0 band recorded at a gas density of 891 amagat at 77 K is shown in Fig. 9, where $\text{Log} [I_0(\nu)/I(\nu)]$ is plotted *versus* the wave-number ν (cm⁻¹). The positions of several transitions are marked along the wave-number axis. The black curve represents the experimental profile. The dashed curves show the individual quadrupolar components and the red solid line represents the individual overlap components. The green circles represent the sum of the overlap and the quadrupolar components.

A good fit between the experimental and the synthetic profile is obtained except in the range 12300-12700 cm⁻¹. The difference between the recorded and the sum profile is interpreted as

arising from the triple transitions Q₁(J₁) + Q₁(J₂) + Q₁(J₃) of hydrogen with (J₁, J₂, J₃) taking values (111), (110), (100) and (000). These transitions contribute to the absorption, where J takes values 0 and 1 at 77K. Fig. 10 represents absorption profiles of the triple transitions of the type Q₁(J₁) + Q₁(J₂) + Q₁(J₃) of H₂ at 77, 201 and 298 K at different densities of the gas in the second overtone region. The plot of $(1/\rho^3) \int \alpha(\nu) d\nu$ *versus* gas density ρ for the triple transition profiles of H₂ at 77, 201 and 298K is given in Fig. 10. The intercepts obtained from the least-square fit give the ternary absorption coefficients. The calculated values are listed in Table 3.

Profile analyses of the recorded spectrum were carried out using the Birnbaum-Cohen (BC) line shape function for the quadrupolar transitions and the Levine-Birnbaum (LB) line shape function for the overlap transitions. The observed spectra were modeled with synthetic profiles, which are composed of the superposition of an overlap-induced profile and a quadrupolar induced profile. The values of the fitting parameters at different temperatures are given in Table 4.

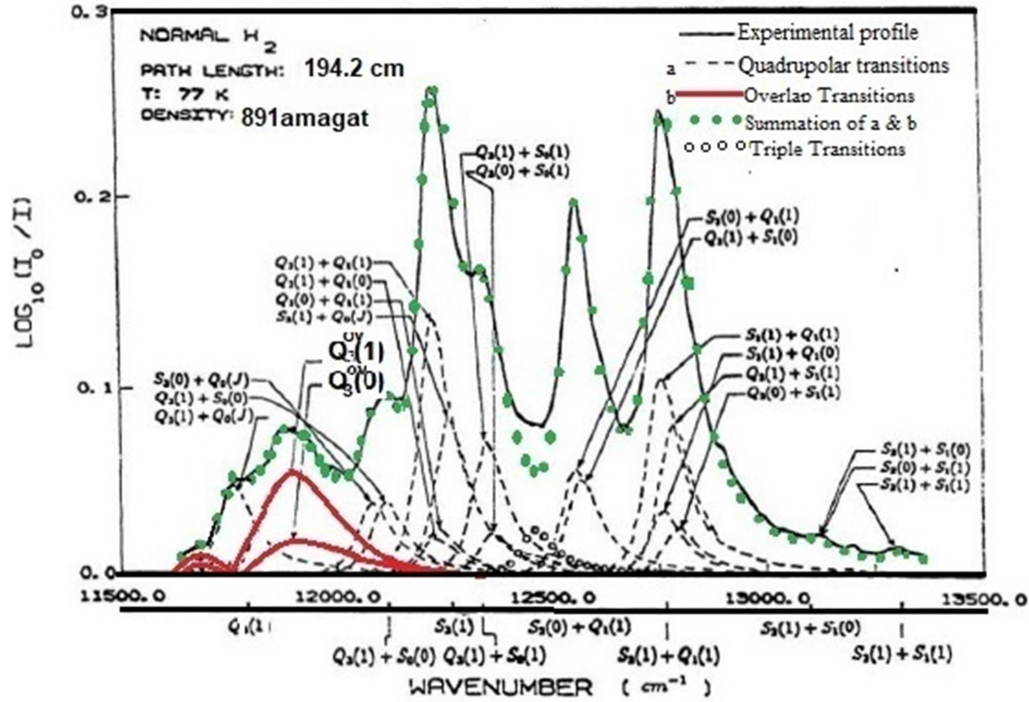


FIG. 9. Analysis of an absorption profile of normal H₂ in the pure gas at 891 amagat and 77 K in the second overtone region. Here, the rotational quantum number J takes the values 0 to 3. The black curve is the experimental profile. The red curve represents the computed overlap-induced profiles, while the dashed curves are quadrupoler-induced profiles. The green circles represent the sum of the computed overlap and quadrupolar components. The difference between the experimental and the sum represented by the curve in open circles is the contribution due to triple transitions.

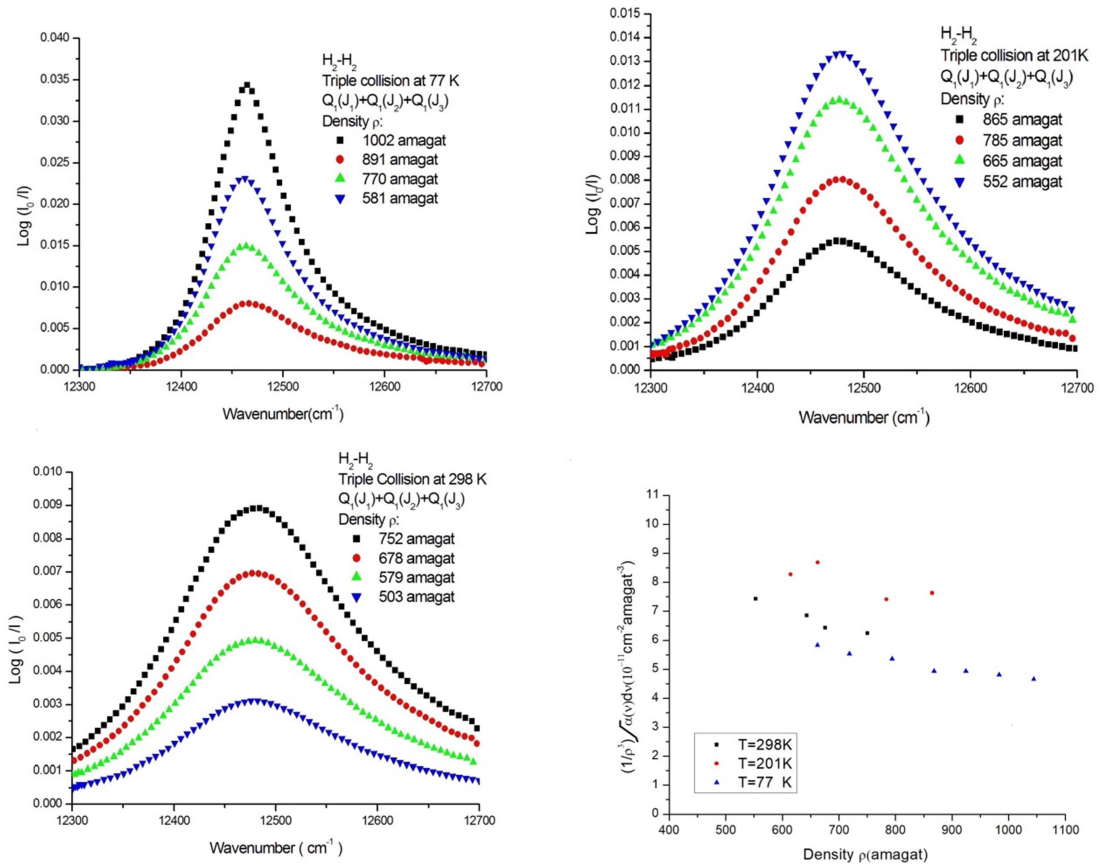


FIG. 10. Absorption profiles of the triple transitions of H₂-H₂-H₂ and $(1/\rho^3) \int \alpha(v) dv$ versus density ρ for the experimental profiles at 298, 201 and 77K.

TABLE 4: Results of profile analysis of H₂-H₂ in the 3-0 band [8, 9].

T	Intra-collisional half-width	Collision duration	Quadrupolar half-width	Collision duration	BC Profile parameters	BC Profile parameters	Overlap contribution	Quadrupolar contribution
(K)	δ_d (cm ⁻¹)	τ_d (10 ⁻¹⁴ s)	δ_q (cm ⁻¹)	τ_q (10 ⁻¹⁴ s)	δ_1 (cm ⁻¹)	δ_2 (cm ⁻¹)	(%)	(%)
77	98±3	5.4	50±1	11.1	47±3	315±4	11	89
201	104±3	5.1	82±1	6.5	100±1	297±3	15	85
298	118±6	4.5	106±3	5.0	135±5	264±4	19	81

Summary of Theoretical Work

A semi-empirical numerical method has been used to compute the binary collision-induced roto-vibrational spectra of hydrogen complexes in the second overtone region at different temperatures. Also, quantum mechanical computation was used to calculate the second overtone profile of hydrogen [11-14].

This code is modified by Borysow and her group. Illustrative examples are given in Fig. 11 and Fig. 12. Fig. 11 shows two profiles calculated at 77 and 298K using the semi-empirical method. Fig. 12 represents two profiles calculated with two methods of normal hydrogen at 77K. These figures are calculated using the code given by Borysow, see:

<https://www.astro.ku.dk/~aborysow/programs/>.

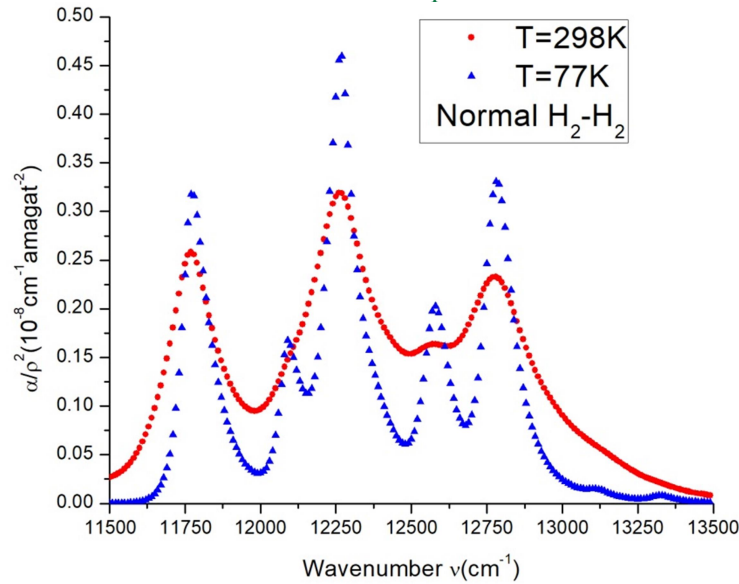


FIG. 11. Two profiles of the CIA spectra calculated theoretically at 77 and 298K.

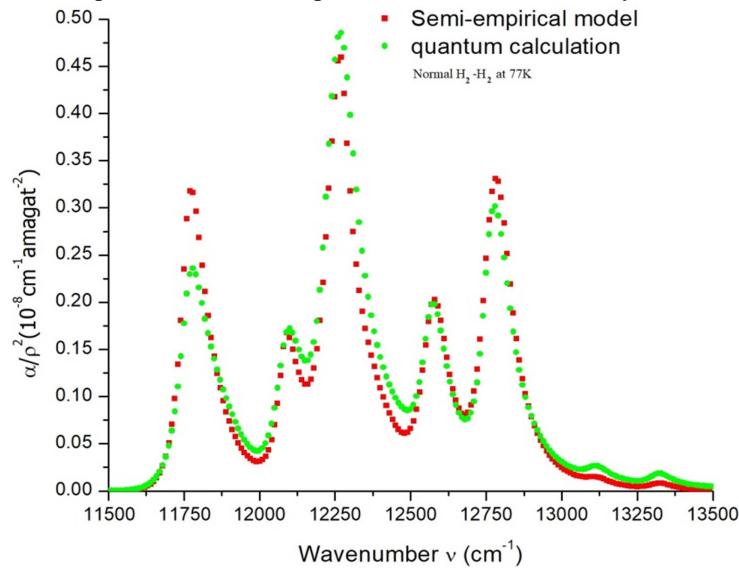


FIG. 12. Theoretical calculations of the CIA spectra of hydrogen at 77K.

Conclusion

The spectra of the second overtone band of H₂-H₂ at 77, 201 and 298K were recorded for different gas densities. Profile analyses of these spectra were carried out using the Birnbaum-Cohen (BC) line shape function for the quadrupolar transitions and the Levine-Birnbaum (LB) line shape function for the overlap transitions. The observed spectra were modeled with synthetic profiles, which are composed of the superposition of an overlap-induced profile and a quadrupolar induced profile. Satisfactory agreement of the measurements with the calculated profiles was observed. The calculated binary and ternary

absorption coefficients are in good agreement with theoretical values found by other researchers.

We have reviewed the second overtone band spectra of H₂-H₂ spectra at different temperatures and densities that were studied since 1949. The aim of this article has been to shed more light on the important results obtained since then.

Acknowledgments

The authors are grateful to Asaad R. Sakhel and Basim N. Bulos for their valuable comments on the article.

References

- [1] Frommhold, L., "Collision-induced absorption in gases", (Cambridge University Press, 1993).
- [2] Kuiper, G.P., *Astrophys. J.*, 109 (1949) 540.
- [3] Herzberg, G., *Astrophys. J.*, 115 (1952) 377.
- [4] Hunt, J.L., Ph.D. Thesis, University of Toronto, (1959), Canada.
- [5] McKellar, A.R.W. and Welsh, H., *Proc. Roy. Soc. Lond. A*, 322 (1971) 421.
- [6] Welsh, H.L., "Pressure-induced absorption spectra of hydrogen", Ed. D. Ramsay (Butterworths, London, 1972).
- [7] Gillard, P.G., Ph.D. Thesis, Memorial University of Newfoundland, (1983), Canada.
- [8] Xiang, F., M.Sc. Thesis, Memorial University of Newfoundland, (1992), Canada.
- [9] Reddy, S.P., Xiang, F. and Varghese, G., *Phys. Rev. Letters*, 74 (1995) 367.
- [10] Moraldi, M. and Frommhold, L., *Phys. Rev. Letters*, 74 (1995) 363.
- [11] Brodbeck, C., Bouanich, J., Thanh, N. and Borysow, A., *Planetary and Space Science*, 47 (1999) 1285.
- [12] Brodbeck, C., Bouanich, J., van Thanh, N., Fu, Y. and Borysow, A., *J. Chem. Phys.*, 110 (1999) 4750.
- [13] Fu, Y., Zheng, C. and Borysow, A., *JQSRT*, 67 (2000) 203.
- [14] Borysow, A., Borysow, J. and Fu, Y., *Icarus*, 145 (2000) 601.
- [15] Borysow, A., Jorgensen, U.G. and Fu, Y., *JQSRT*, 68 (2001) 235.
- [16] Abel, M., M.Sc. Thesis, The University of Texas, (2009), Austin.
- [17] Abel, M., Frommhold, L. and Gustafsson, M., *Journal of Chemical Physics*, 131 (2009) 181102.
- [18] Abu-Kharma, M., Shawagfeh, N. and Gillard, P., 20th ICSSL Ed. J. Lewis, *Predio-Cross. AIP* (2010) 245.
- [19] Abu-Kharma, M., *Can. J. Phys.*, 90 (2012) 339.
- [20] Abu-Kharma, M., *J. Mol. Spect.*, 48-50 (2015) 308.
- [21] Poll, J.D., *Proc. Symposium, I.A.U.*, No. 40 on Planetary Atmospheres (Morfa, Texas, Dordrecht: Reidel, 1969).
- [22] Lewis, J.C., *Spectral Line-shapes*, Ed. M. Roger Herman, (American Institute of Physics, 1999).
- [23] Bragg, S.L. Brault, J.W. and Smith, W.H., *Astrophys. J.*, 263 (1982) 999.
- [24] Foltz, J.V., Rank, D.H. and Wiggins, T.A., *J. Mol. Spect.* 21 (1966) 203.
- [25] Rose, M.E., "Elementary Theory of Angular Momentum", (John Wiley and Sons, Inc. NY, 1957).
- [26] van Kranendonk, J., *Can. J. Phys.*, 46 (1968) 1173.

Estimation of Radionuclide Concentrations and Average Effective Dose from Some Selected Imported Foodstuff

A. B. Ogunremi^{a,b} and K. A. Adewoyin^b

^a Department of Physical, Federal University of Agriculture Abeokuta, Abeokuta, Nigeria .

^b Department of Physical Science, Yaba College of Technology, Yaba Lagos, Nigeria.

Received on: 4/12/2018;

Accepted on: 21/4/2019

Abstract: Radionuclide concentrations in imported food products depend on the geological and mineralogical characteristics of the soil from which the products are derived and this is a major cause of concern in radiation monitoring. The analysis of three naturally occurring radionuclides that are: ²²⁶Ra, ²³²Th and ⁴⁰K in fourteen selected imported food samples was carried out in this research using sodium iodine detector. Reasonable quantities of each of the samples were packed in cylindrical containers and kept for a month to attain secular equilibrium. The activity concentrations of the analyzed samples ranged from 48.76 ± 5.03 to 85.45 ± 3.20 , from 10.10 ± 1.70 to 21.10 ± 2.20 and from 8.06 ± 1.4 to 10.54 ± 3.64 Bq/kg and their average values were 65.32 ± 4.14 , 11.23 ± 2.18 and 9.68 ± 2.08 for ⁴⁰K, ²²⁶Ra and ²³²Th, respectively. For ²³²Th, ten samples were seen to be below detection limit BDL. The mean effective dose was estimated to be $4.17 \mu\text{Sv/y}$. The result of the radiation dose was less than the average value of 1mSv/y for general public, making the foodstuff analyzed radiologically safe for consumption.

Keywords: Imported foodstuff, Radionuclides, Monitoring, Effective dose, Consumption.

Introduction

Foods are substances whether in liquid, solid, frozen, dried or dehydrated form that are consumed by humans to provide essential nutrients (vitamins, minerals and fats) for growth and development. They are ingested by organisms and assimilated into their cells to provide energy. Food remains the most critical need for human existence. It has been estimated that at least one-eighth of the mean annual effective dose due to natural sources is caused by the consumption of foodstuff [1, 2]. Radionuclide concentrations in imported food products depend on the geological and mineralogical characteristics of the soil from which the products are derived and this is a major cause of concern in radiation monitoring. Food consumed by humans may be contaminated through naturally occurring radioactivity, nuclear power plant accidents,

winds or rainfall, as well as through nuclear weapons which are deposited on plants, soil or water and can enter the food chain through the absorption *via* plant roots, putting human beings at risk after ingestion of the contaminated food, leading to acute health effects, such as nausea and vomiting, as well as to chronic health effects, such as increase in the risk of cancer [3]. The aim of this work, therefore, is the estimation of radionuclide concentrations and average effective dose through ingestion from some selected imported foodstuff.

Materials and Methods

Food Sampling and Preparation

Fourteen samples of imported foodstuff were selected for analysis as these are foods commonly taken by Nigerians. The samples

were dried by placing them in the oven for 24 hrs at 110 °C, to ensure that moisture is completely removed. Then, some foodstuff, like rice, cornflakes, oat, beans, ... etc. were ground and sieved to give room for uniformity in size. The samples were then weighed with a weighing balance and 100g of nutmeg, cocoa, ... etc., which were already homogenized, were sealed and packed in plastic containers of 8cm height and 6cm diameter. The containers were later sealed using paper- tape to avoid any possibility of radon leakage. All the fourteen samples were kept for at least 4 weeks (28 days) to attain secular equilibrium between radon and its daughters [4] prior to gamma spectroscopy analysis. After the preparation, the radionuclide concentrations in the samples were measured.

Measurement of Radionuclides with Gamma - Ray Spectroscopy

The analysis of all the samples was carried out using a well-calibrated NaI (TI) and well-shielded detector couple to a computer resident quantum MCA2100R multichannel analyzer for 36,000s. The background sample measurement by the detector was achieved by filling an empty thoroughly clean plastic container with distilled water and counting for the same reasonable period as the sample and the peaks were resolved for the natural radionuclide.

1460KeV gamma-radiation of ^{40}K was used to determine the concentration of ^{40}K in the sample. The gamma transition energy of 1764.5KeV ^{214}Bi was used to determine the concentration of ^{238}U , while the gamma transition energy of 2614KeV ^{208}Tl was used to determine the concentration of ^{232}Th and ^{137}Cs was detected by its 661.6KeV gamma energy. The efficiency calibration of the detector was carried out using a reference standard mixed source traceable to Analytical Quality Control Service (AQCS, USA), which has certified activities of the selected radionuclides and has a geometrical configuration identical to the sample containers. The activity concentration in the sample was obtained using the expression in [5, 6].

$$C \left(\frac{\text{Bq}}{\text{kg}} \right) = \frac{C_n}{\varepsilon \rho_\gamma M_s} \quad (1)$$

where C is the activity concentration of the radionuclide in the sample, C_n is the count rate under each photopeak due to each radionuclide, ε is the detection efficiency for the specific gamma energy, ρ is the absolute transition probability of the specific gamma energy and M_s is the mass of the sample.

Results and Discussion

The results of the activity concentration (Bq/kg) of the primordial elements targeted in the samples are shown in Table 1.

Potassium has the highest concentration when compared with other radionuclides from the foodstuff samples.

There are variations in the activity concentrations of radionuclides among the different food samples. The activity concentration of ^{40}K ranged from 48.76 ± 5.03 Bq/kg to 85.45 ± 3.20 Bq/kg with a mean value of 65.32 ± 1.77 Bq/kg, ^{226}Ra ranged from 10.06 ± 2.24 Bq/kg to 21.10 ± 2.03 Bq/kg with a mean value of 11.23 ± 0.85 Bq/kg and ^{232}Th ranged from BLD to 10.54 ± 3.64 Bq/kg with a mean value of 9.68 ± 1.59 , as shown in Table 1. Samples 7 and 2 exhibited the first and second highest concentration of ^{40}K with values of 85.45 ± 3.2 Bq/kg and 74.84 ± 1.02 Bq/kg, respectively. The first and second highest concentrations of ^{226}Ra were found in samples 14 and 5 with their corresponding values as 21.10 ± 2.03 and 12.04 ± 1.38 Bq/kg, respectively. The first and second highest concentrations of ^{232}Th were 10.54 ± 3.64 and 10.45 ± 1.2 Bq/kg for samples 5 and 7, respectively. From all the measured samples, ten samples of ^{232}Th had values below the detection limit. The study revealed that the activity concentrations of ^{226}Ra , ^{232}Th and ^{40}K for all samples under study were much lower than the activity concentration values in food, which are usually in the range 40- 600Bq/kg [7]. The trend of activity concentrations of the radionuclides was in the order of magnitude $^{40}\text{K} > ^{226}\text{Ra} > ^{232}\text{Th}$ in all the sample studied.

TABLE 1. Activity concentrations of ^{40}K , ^{226}Ra and ^{232}Th (Bq/kg) in the food samples.

S/N	PRODUCT NAME	Origin	^{40}K	^{226}Ra	^{232}Th
1	Nutmeg	USA	65.59±3.19	10.49±2.50	BDL
2	Quaker Oat	U.K	74.84±1.02	10.10±2.01	BDL
3	Titus Fish	Cotonou	72.34±6.29	10.19±3.01	BDL
4	Olotu Beans	South Africa	65.22±5.03	11.25±1.09	BDL
5	Horlicks Cocoa	U. K	68.03±5.88	12.04±1.38	10.54±3.64
6	Thailand Rice	Cotonou	55.02±3.90	10.10±1.70	BDL
7	K. Cornflakes	South Africa	85.45±3.20	10.10±2.20	10.45±1.2
8	Creamcraker B.	U. K	63.08±3.19	11.25±0.09	BDL
9	Instant Coffee	South Africa	65.47±2.45	10±2.24.06	BDL
10	Ginger	U.S.A	65.38±6.64	10.12±1.53	BDL
11	Cerellac	U. K	65.31±6.29	10.13±1.85	BDL
12	Frisco Gold	Netherland	48.76±5.03	10.12±3.23	BDL
13	Horlicks milk	U. K	55.10±5.88	10.12±3.13	8.06±0.66
14	White Oat	U.S.A	64.84±2.45	21.10±2.03	DBL
Mean +S.D.			65.32±1.77	11.23±0.85	9.68±1.59

BDL: Below Detection Limit.

Annual Effective Dose from Ingestion of the Food Samples

The effective dose helps estimate the doses from radionuclides through ingestion from different sources of radioactivity. It is based on the risks of radiation-induced health effects [6].

The annual effective dose due to the intake of radionuclides from foodstuff is calculated using the metabolic model developed by [8, 9]:

$$D_{rf} \left(\frac{\text{Sv}}{\text{y}} \right) = R_f \sum (C_r A_{rf}) \quad (2)$$

where D_{rf} is the annual effective dose in Sv/y, C_r is the effective dose conversion factor 0.28 E-06,

0.23 E-07 and 0.006 E-06 Sv/Bq, for ^{226}Ra , ^{232}Th and ^{40}K , respectively. A_{rf} is the activity concentration of the radionuclide in the ingested foodstuff. R_f is the consumption rate (kg/y) and the values are presented in Table 2.

The effective dose ($\mu\text{Sv/y}$) varied from 0.01 in Olotu beans to 15.88 in rice. The estimated values for baby foods, which are cerelac, friscogold, horlick milk, white oat and beans, are extremely small compared with effective dose values for rice, cornflakes and creamcraker. The mean effective dose was estimated to be 4.17($\mu\text{Sv/y}$).

TABLE 2. Consumption rate and annual effective dose.

S/N	Product Name	Consumption rate (kg/y)	Annual effective dose ($\mu\text{Sv/y}$)
1	Nutmeg	4.90	3.11
2	Quaker Oat	0.03	0.02
3	Titus	11.2	7.49
4	Olotu Beans	0.02	0.01
5	Horlicks	2.00	1.37
6	Rice	28.23	15.88
7	Cornflakes	20.67	15.40
8	Creamcraker	18.55	11.82
9	Instant Coffee	0.04	0.03
10	Ginger	5.00	3.13
11	Cerelac	0.03	0.02
12	Frisco	0.03	0.02
13	Horlicks milk	0.03	0.02
14	White Cat	0.03	0.03
Mean			4.17

Source: Food Balance Sheet, Nigeria, 2006.

Conclusion

This research has helped identify and measure the primordial radionuclides present in the imported foodstuff consumed by Nigerians, in order to determine the activity concentrations and assess the health impact from the consumption of the foodstuff. Furthermore, it has also helped ascertain the level of health risks that might be involved for countries consuming the foodstuff.

The variations of radionuclide concentrations from one sample to another might stem from the heterogeneity of the environment from where the foodstuff originated.

The health impact assessment of the present study revealed that the consumption of the analyzed imported foodstuff does not pose any radiological effects to Nigerians consuming them. Nonetheless, there is a need for regular monitoring of the imported foodstuff so as to avoid the accumulative effect of doses.

References

- [1] UNSCEAR, "Sources and Effects of Ionizing Radiation". United Nation Scientific Committee on Atomic Radiation. Vol.1, New York, United Nation Publication (2000).
- [2] Hosseini, T., Fathivand, A.A., Abbasiasar, F., Karimi, M. and Barati, H. (2006). *Radiat. Prot. Dos.*, 121 (3) (2006) 330.
- [3] Addo, M.A., Darko, E.O., Gordon C. and Nyarko, B.J.B., *International Journal of Environmental Sciences*, 3 (6) (2013) 2312.
- [4] International Atomic Energy Agency (IAEA). "Guidelines for Radioelement Mapping Using Gamma Ray Spectrometry Data", IAEA-TECDOC-1363, Vienna-Austria, (2003) Pp. 6–7.
- [5] Akinloye, M.K. and Olomo, J.B, *Nigerian Journal of Physics*, 12 (2000) 60.
- [6] Jibiri, N.N., Farai, I.P. and Alausa, S.K., *Journal of Environmental Radioactivity*, 94 (1) (2007) 31.
- [7] Amin, S., Al-Kafaje, M. and Al-Ani R. *Journal of Natural Sciences Research*, 6 (13) (2016) 2224.
- [8] International Commission of Radiological Protection ICRP, "Age- dependent Doses to Members of the Public from Intake of Radionuclides: Part 5". *Compilation of Ingestion and Inhalation Dose Coefficient (ICRP Pub. No. 72)* (Pergamon Press, Oxford, 1996).
- [9] Abojassim, A.A., Hady, H.N. and Mohammed, Z.B., *Journal of Bioenergy and Food Science*, 3 (3) (2016) 113.
- [10] Federal Office of Statistics, Nigeria (FOS), *Compilation of FOS/FAO Annual Consumption Data/Food Balance Sheet of Nigeria. A Publication of Federal Office of Statistics (FOS), Nigeria, (2006).*

Study of Lattice Parameter and Nanoparticle Size in Lead Chalcogenides (PbX, X = S, Se & Te)

D. R. Adhikari^a, S. K. Adhikari^b and H. P. Lamichhane^c

^a Department of Physics, Amrit Science Campus, Tribhuvan University, Kirtipur, Kathmandu, Nepal.

^b Department of Physics, Birendra Multiple Campus, Tribhuvan University, Kirtipur, Kathmandu, Nepal.

^c Central Department of Physics, Tribhuvan University, Kirtipur, Kathmandu, Nepal..

Received on: 31/3/2019;

Accepted on: 23/6/2019

Abstract: In the present paper, the structural and electronic properties have been studied with the help of thermodynamic parameter. The lattice parameter and nanoparticle size in lead chalcogenides [(PbX, X = S, Se and Te)] are calculated with the help of fitting parameter under the effect of temperature. The calculated values are in close agreement with the experimental results.

Keywords: Lead chalcogenides, Lattice parameter, Nanoparticle size, Energy band gap.

Introduction

Lead chalcogenides (Pb X, X = S, Se and Te) are narrow band gap (0.2-0.4 eV) semiconductors at lower temperatures. They have unique structural and electronic properties. They have wide technological applications and are used to fabricate various optoelectronic, spintronic and thermo-electronic devices, as well as in nanoscience and nanotechnology [1-9]. Various classes of thermoelectric materials had been developed, such as bismuth telluride for low-temperature applications [10, 11] and germanium telluride for higher-temperature applications [12]. Theoretical and experimental studies have been performed on their structural and electronic properties [13-22]. Those properties have been studied in terms of lattice constant, nanoparticle size and energy band gap under the effect of temperature. Lattice constant and energy band gap are functions of temperature [15-22]. The structural and electronic properties, such as lattice constant (a) and nanoparticle size (R), are calculated. The calculated values are compared with experimental results.

Theoretical Methodology

Lead chalcogenides are narrow band gap semiconductors. Energy band gap and lattice parameter are functions of temperature [24-25]. The crystal structure of lead chalcogenide is of NaCl (B1) type. The coordination number and bond between lead (Pb) and chalcogen {X = S, Se, Te} are 6 and ionic, respectively. The electronic and structural properties were studied in terms of lattice parameter and energy band gap with temperature [23-26]. Various experimental studies have found that lead chalcogenides exhibit strongly anharmonic lattice dynamics [27]. Coulomb interaction and short-range two-body interaction in lead chalcogenides are given by:

$$U_{ij} = \frac{Q_i Q_j}{R_{ij}} + X e^{-\frac{R_{ij}}{\rho}} - \frac{D_6}{R_{ij}^6} \quad (1)$$

In Eq. 1, the first term describes the long-range Coulomb interaction between two charges. The second term indicates the repulsive potential. The third term represents the dipole-

dipole interaction Buckingham potential; where X, ρ and D_6 are fitting parameters. Short-range cation-cation interactions are ignored. Thermodynamic enthalpy in NaCl (B1) structure is given by:

$$H = E + PV. \quad (2)$$

The Gibbs free energy is given by:

$$G = H - TS. \quad (3)$$

According to the classical Heisenberg model, the Hamiltonian is given by:

$$\mathcal{H} = -\frac{1}{2} \sum \vec{S}_i (J_1 \sum_j^{nn} \vec{S}_j + J_2 \sum_j^{nnn} \vec{S}_j) \quad (4)$$

with normalized spin vectors \vec{S}_i and \vec{S}_j and summation over nearest neighbor and next nearest neighbor.

The energy differences in terms of J_1 and J_2 are given by the following relations:

$$\Delta E_1 = 8J_1$$

$$\Delta E_2 = 6J_1 + 6J_2.$$

The atomic radius of lead chalcogenide PbX (X=S, Se and Te) is a function of temperature. Then,

$$R(T) = A + BT + CT^2 \quad (5)$$

where A, B and C are the fitting parameters, the values of which are given in Table 1.

The lattice parameter in term of atomic radius is given by the following relation:

$$a(T) = 2\sqrt{2} R(T).$$

The energy gap is related with temperature and lattice parameter by the following relation:

$$\left[\frac{\partial E_g}{\partial T} \right]_{LATTICE} = \left(\frac{\partial E_g}{\partial a} \right) \left(\frac{\partial a}{\partial T} \right). \quad (6)$$

The forbidden width is a linear function of temperature [28-30]. Then,

$$E_g(T) = E_g(0) + \frac{\partial E_g}{\partial T} T, \quad (7)$$

$E_g(0)$ being the energy at absolute zero.

The enthalpy of lead chalcogenide crystal is defined as:

$$H \approx H_{ELEC} + H_{VIB}^0 + H_{VIB}(T) + H_{ROT}(T) + H_{TRANS}(T) + RT \quad (8)$$

where, H_{ELEC} is the electronic component of enthalpy, H_{VIB}^0 is the vibrational component of enthalpy (main State), $H_{VIB}(T)$ is the vibrational

component of enthalpy, $H_{ROT}(T)$ is the rotational component of enthalpy, $H_{TRANS}(T)$ is the trans. component of enthalpy, R is the universal gas constant and T is the temperature.

The entropy of the crystal is the sum of following components:

$$\Delta S = S_{TRANS} + S_{VIB} + S_{ELECT} - nR[\ln(nN_0) - 1] \quad (9)$$

where, N_0 is the Avogadro constant and N is the number of moles in the molecules.

The Gibbs free energy of the crystal is determined in term of the entropy of individual members of molecules of reagent Pb and X (S, Se and Te). Then,

$$\Delta G = H_{Pb} - H_X + \frac{1}{2} \sum_{i \in Pb} h \nu_i - \frac{1}{2} \sum_{j \in X} h \nu_j - T (S_{VIB}^{Pb} - S_{VIB}^X + S_{ROT}^{Pb} - S_{ROT}^X + S_{TRANS}^{Pb} - S_{TRANS}^X) \quad (10)$$

where, H_{Pb} is the enthalpy of lead, H_X is the enthalpy of chalcogen [X = S, Se and Te], S_{VIB}^{Pb} is the entropy of lead due to vib. component, S_{VIB}^X is the entropy of chalcogen due to vib. component, S_{ROT}^{Pb} is the entropy of lead due to rot. component, S_{ROT}^X is the entropy of chalcogen due to rot. component, S_{TRANS}^{Pb} is the entropy of lead due to trans. component and S_{TRANS}^X is the entropy of chalcogen due to trans. component.

The particle size of PbX (X = S, Se and Te) has been calculated by effective mass of holes and electrons. Now, the carrier effective mass of a hole is given by:

$$m_h^* = 1.44 m_e^* \quad (11)$$

where m_e^* be the carrier effective mass of an electron.

Generally, electrons and holes are in the conduction band and valence band, respectively. Both achieved the lowest energy for an optical transition from valence band to conduction band. Then, the expression for the radius of nanoparticle is given by:

$$R^2 = \frac{h^2}{8(\Delta E_{gT} - \Delta E_g)} \left[\frac{1}{m_e^*} + \frac{1}{m_h^*} \right] \quad (12)$$

where, ΔE_{gT} is the energy gap at 4.2K and 300K, respectively and ΔE_g is the energy gap at 0K.

The structural properties have been predicted by lattice parameter and are shown in Figs. 1, 2 and 3. In Figs. 1, 2 and 3, the lattice parameter is the linear function of temperature. The values of

lattice parameter and nanoparticle size are calculated. The calculated values of lattice parameter and nanoparticle size are shown in

Tables 1 and 2, respectively. Finally, our calculated values are in close agreement with the experimental results.

TABLE 1. Variation of atomic radius and lattice parameter with temperature for lead chalcogenides (PbX, X=S, Se and Te).

Temperature K	PbS	PbSe	PbTe
	$R(t) = \frac{a}{2\sqrt{2}}$	$R(t) = \frac{a}{2\sqrt{2}}$	$R(t) = \frac{a}{2\sqrt{2}}$
	A = 2.082 (Å)	A = 2.157 (Å)	A = 2.277 (Å)
	B = 0.367×10 ⁻⁴ (Å K ⁻¹) C = 2.938×10 ⁻⁸ (Å K ⁻²)	B = 3.136×10 ⁻⁵ (Å K ⁻¹) C = 0.417×10 ⁻⁷ (Å K ⁻²)	B = 0.371×10 ⁻⁴ (Å K ⁻¹) C = 2.867×10 ⁻⁸ (Å K ⁻²)
	Calc. Exp.[28-30]	Calc. Exp.[28-30]	Calc. Exp.[28-30]
0	2.082	2.157	2.277
4	2.082	2.158	2.278
75	2.085	2.159	2.280
150	2.088	2.165	2.283
225	2.091	2.166	2.286
300	2.095	2.170	2.290
375	2.100	2.175	2.295
400	2.101	2.176	2.296
525	2.109	2.184	2.304
600	2.114	2.190	2.309

TABLE 2. Nanoparticle size of lead chalcogenides at different temperatures and band gaps.

Compound	Energy gap (ΔE_g) at 0K eV Exp. [16]	Energy gap (ΔE_g) at 4K eV	Particle size (R) nm	Energy gap (ΔE_g) at 300K eV	Particle size (R) nm
PbS	0.290	0.20	5.42	0.26	9.39
PbSe	0.170	0.18	16.27	0.23	6.64
PbTe	0.190	0.65	2.4	0.69	2.03

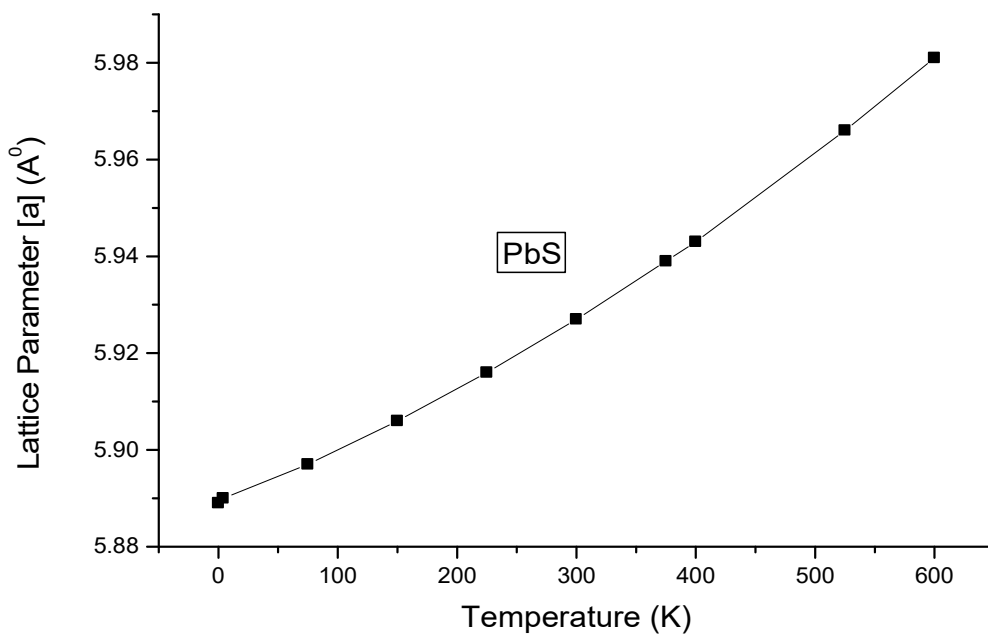


FIG. 1. Lattice parameter with temperature for PbS.

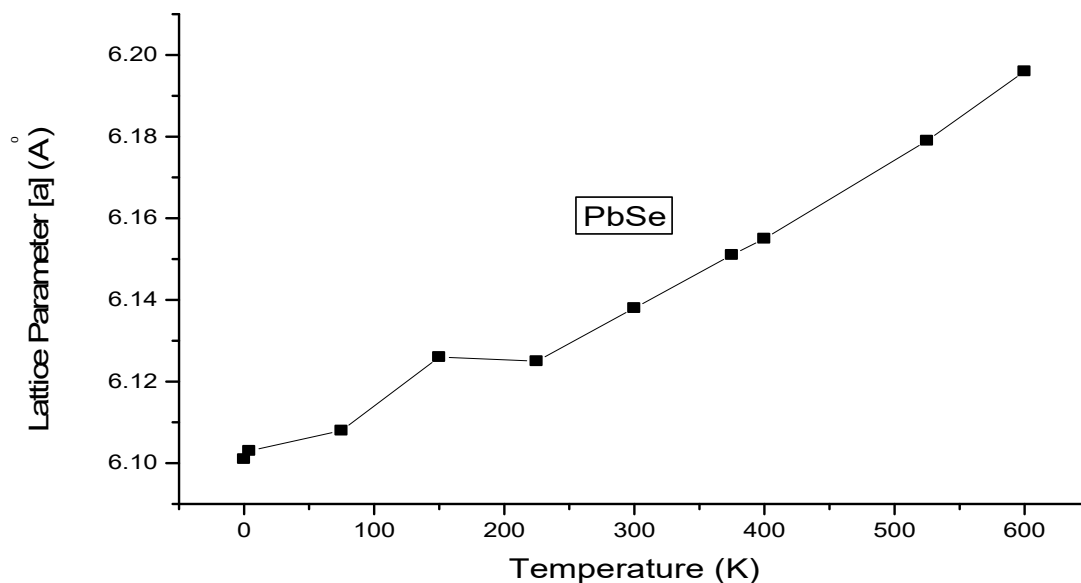


FIG. 2. Lattice parameter with temperature for PbSe.

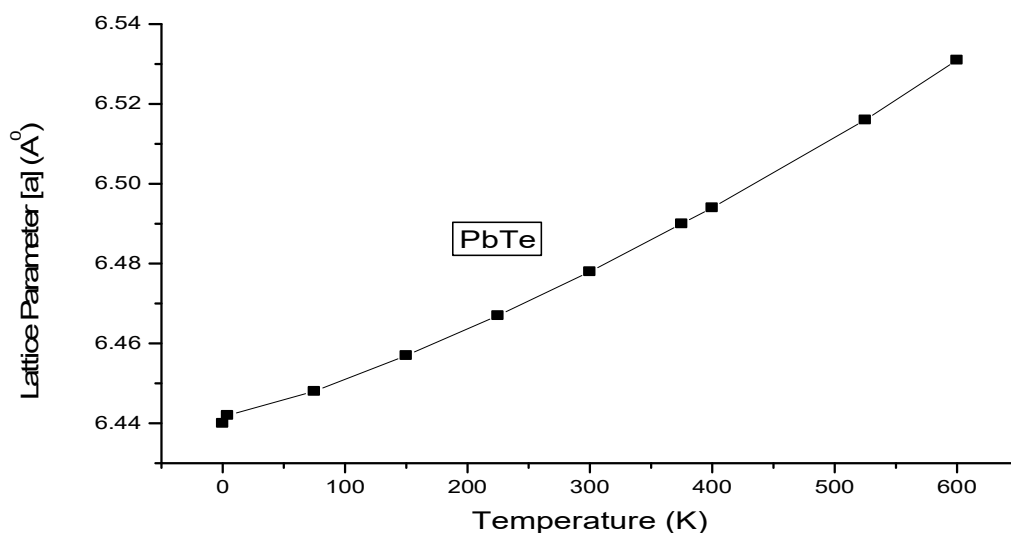


FIG. 3. Lattice parameter with temperature for PbTe.

Results and Discussion

In this method, the lattice parameter and nanoparticle size in lead chalcogenides [(PbX, X = S, Se and Te)] have been studied under the effect of temperature. We have studied the structural and electronic properties and calculated the lattice parameter and nanoparticle size of given compounds at different temperatures. The values of lattice parameter and nanoparticle size in various temperatures are shown in Tables 1 and 2, respectively. The

variations of lattice parameter with temperature are predicted in Fig. 1, Fig. 2 and Fig. 3 for PbS, PbSe and PbTe, respectively. The values of lattice parameter are a linear function of temperature. The fitting parameters have been taken different for different compounds. During the electronic transition, the values of nanoparticle size have been calculated and are shown in Table 2. Our calculated values of Tables 1 and 2 are in close agreement with experimental results.

References

- [1] Smelyansky, V.I. and Tse, J.S., *Physical Review B*, 52 (7) (1995) 4658.
- [2] Paul, A. and Klimeck, G., *Applied Physics Letters*, 98 (21) (2011) 212105.
- [3] Albanesi, E.A., Okoye, C.M.I., Rodriguez, C.O. et al., *Physical Review B: Condensed Matter and Materials Physics*, 61 (24) (2000) 16589.
- [4] Grzechnik, A. and Friese, K., *Journal of Physics Condensed Matter*, 22 (9) (2010) 095402.
- [5] Rousse, G., Klotz, S., Saitta, A.M. et al., *Physical Review B*, 71 (22) (2005) 224116.
- [6] Ovsyannikov, S.V., Shchennikov, V.V., Manakov, A.Y. et al., *Physica Status Solidi (B) Basic Research*, 244 (1) (2007) 279.
- [7] Panda, B.K. and Padhi, H.C., *Physica Status Solidi B*, 166 (2) (1991) 519.
- [8] Chattopadhyay, T., Werner, A., von Schnering, H.G. and Pannetier, J., *Revue de Physique Appliquee*, 19 (9) (1984) 807.
- [9] Chattopadhyay, T., von Schnering, H.G., Grosshans, W.A. and Holzappel, W.B., *Physica B+C*, 139-140 (1986) 356.
- [10] Beeri, O., Rotem, O., Hazan, E., Katz, E.A., Braun, A. and Gelbstein, Y., *Journal of Applied Physics*, 118 (11) (2015) 115104.
- [11] Vizel, R., Bargig, T., Beeri, O. and Gelbstein, Y., *Journal of Electronic Materials*, 45 (3) (2016) 1296.
- [12] Hazan, E., Mandar, N., Parag, M., Casian, V., Ben-Yehuda, O. and Gelbstein, Y., *Advanced Electronic Materials*, 1 (11) (2015) 1500228.
- [13] Peng, X., Manna, L., Yang, W., Wickham, J., Scher, E., Kadavanich, A. and Alivisatos, A.P., *Nature*, 404 (2000) 59.
- [14] Peng, Z.A. and Peng, X., *J. Am. Chem. Soc.*, 123 (2001) 183.
- [15] Schaller, R.D. and Klimov, V.I., *Phys. Rev. Lett.*, 92 (2004) 186601.
- [16] Ellingson, R.J., Beard, M.C., Johnson, J.C., Yu, P., Micic, O.I., Nozik, A.J., Shabaev, A. and Efros, A.L., *Nano Lett.*, 5 (2005) 865.
- [17] Sadao, A., "Properties of Group-IV, III-V and II-VI Semiconductors", (Wiley, New York, 2005).
- [18] Alivisatos, A.P., *Science*, 271 (1996) 933.
- [19] Madelung, O., Rössler, U. and Schulz, M., *Landolt-Börnstein III/41C: 1998, Non-Tetrahedrally Bonded Elements and Binary Compounds*, Springer Verlag, Berlin, Germany (1998).
- [20] Bencherif, Y., Boukra, A., Zaoui, A. and Ferhat, M., *Materials Chemistry and Physics*, 126 (3) (2011) 707.
- [21] Ahuja, R., *Physica Status Solidi (B) Basic Research*, 235 (2) (2003) 341.
- [22] Hummer, K., Gruneis, A. and Kresse, G., *Physical Review B: Condensed Matter and Materials Physics*, 75 (19) (2007) 195211.
- [23] Pei, Y.Z., Shi, X.Y., LaLonde, A., Wang, H., Chen, L.D. and Snyder, G.J., *Nature*, 473 (2011) 66.
- [24] Gibbs, Z.M., Kim, H., Wang, H., White, R.L., Drymiotis, F., Kaviani, M. and Jeffrey Snyder, G., *Applied Physics Letters* 103 (2013) 262109.
- [25] Heremans, J.P., Jovovic, V., Toberer, E.S., Saramat, A., Kurosaki, K., Charoenphakdee, A., Yamanaka, S. and Snyder, G.J., *Science*, 321 (2008) 554.
- [26] Tian, Z.T., Garg, J., Esfarjani, K., Shiga, T., Shiomi, J. and Chen, G., *Phys. Rev. B*, 85 (2012) 184303.
- [27] Bozin, E.S., Malliakas, C.D., Souvatzis, P., Proffen, T., Spaldin, N.A., Kanatzidis, M.G. and Billinge, S.J.L., *Science*, 330 (2010) 1660.
- [28] Miller, A.J., Saunders, G.A. and Yagci, Y.K., *J. Phys. C: Solid State Phys.*, 14 (11) (1981) 1569.
- [29] Dornhaus, R., Nimtz, G. and Schlicht, B., *Springer Tr. Mod. Phys.*, 98 (1983) R5.
- [30] Madelung, O., Schultz, M. and Weiss, H., "Group III Semiconductors", (Springer, Berlin, 1982).

Magnetization and Magnetic Susceptibility of GaAs Quantum Dot with Gaussian Confinement in Applied Magnetic Field

M. Ali, M. Elsaid and A. Shaer

Physics Department, Faculty of Science, An-Najah National University, Nablus, West Bank, Palestine.

Received on: 02/03/2019;

Accepted on: 25/6/2019

Abstract: We present a theoretical study of the magnetization (M) and the magnetic susceptibility (χ) of single electron Gaussian quantum dot (GQD) presented in a magnetic field. We solve the Hamiltonian of this system including the spin by using exact diagonalization method. All the energy matrix elements are obtained in closed analytic form. We investigate the effects of temperature, magnetic field and confining potential depth on the behavior of magnetization and magnetic susceptibility of the quantum dot. Comparisons show that our results are in very good agreement with reported works.

Keywords: Gaussian quantum dot, Magnetic field, Exact diagonalization method, Magnetization, Magnetic susceptibility.

PACS: 73.21.La, 65.80.-g

1. Introduction

The study of quantum dot (QD) structures has received great attention in recent years due to their physical properties and great potential device applications, such as quantum dot lasers, solar cells, single electron transistors and quantum computers [1- 5]. The introduction of a magnetic field perpendicular to the dot plane introduces an additional structure on the energy levels and correlation effects of the interacting electrons confined in a quantum dot.

Different authors had solved the QD Hamiltonian with parabolic potentials by using analytical and various numerical methods [6-18]. The Gaussian potential has been proved to be an effective potential in many branches of physics. It has been solved approximately for a single particle problem by many authors [19-27]. The exact diagonalization and variational methods have been used to study the electronic, thermodynamic and magnetic properties of single and coupled QDs [28-35].

The purposes of this work are: first, to calculate the statistical energy $\langle E \rangle$ of a single electron confined in a Gaussian quantum dot (GQD) by solving the QD Hamiltonian using exact diagonalization method; second, the obtained statistical energy will be used to investigate the dependence of magnetization (M) and magnetic susceptibility (χ), as thermodynamic quantities, on magnetic field strength (B), temperature (T) and confining potential depth (V_0), taking into account the presence of the spin (S).

The structure of this paper is organized as follows: the Hamiltonian theory and computation method of a single electron in GQD are presented in section 2. In section 3, we show how to calculate magnetization and magnetic susceptibility from the mean energy expression. The final section is devoted to numerical results and discussion.

2. Theory

The theory in this research consists mainly of three main parts: the two-dimensional (2D) Hamiltonian model, the exact diagonalization technique and the calculation of magnetic properties, such as statistical energy, magnetization and magnetic susceptibility.

Quantum Dot Hamiltonian

The Hamiltonian of a single electron system in an external magnetic field with the presence of Gaussian confinement potential is given as:

$$\hat{H} = \frac{1}{2m^*} \left(\vec{P} + \frac{e}{c} \vec{A} \right)^2 + V(\vec{\rho}) \quad (1)$$

where $\vec{\rho}$ refers to the position vector of an electron, \vec{P} is the momentum operator, m^* is the electron effective mass and \vec{A} is the vector potential corresponding to the applied magnetic field \vec{B} along z-direction including the spin Zeeman term. The magnetic field is given by $\vec{B} = \vec{\nabla} \times \vec{A}$ and $V(\vec{\rho})$ is the confining potential taken as Gaussian potential,

$$V(\rho) = -V_0 e^{-\frac{\rho^2}{2R^2}} \quad (2)$$

The Hamiltonian can be rewritten as:

$$\hat{H} = -\frac{\hbar^2}{2m^*} \nabla_{\rho}^2 + V(\rho) + \frac{1}{8} m^* \omega_c^2 \rho^2 + \frac{1}{2} \hbar \omega_c (\hat{L}_z + g \hat{S}_z) \quad (3)$$

where \hat{L}_z is the z component of the angular momentum of the electron, ω_c is the cyclotron frequency given by $\omega_c = eB/m^*$, where B is the strength of the applied magnetic field, R is the quantum dot radius, V_0 is the depth of the confining potential and g^* is the effective Lande g-factor which equals -0.44 for GaAs.

Exact Diagonalization Method

The Gaussian potential term makes the analytical solution of this system not possible. We intend to solve the Hamiltonian by using the exact diagonalization method. The bases are taken to be Fock-Darwin states [21, 36], given as:

$$|nm_z\rangle = \frac{\alpha}{\sqrt{\pi}} \left(\frac{n!}{(n+|m_z|)!} \right)^{\frac{1}{2}} (\alpha \rho)^{|m_z|} L_n^{|m_z|}(\alpha^2 \rho^2) e^{-\frac{1}{2} \alpha^2 \rho^2} e^{i m_z \phi} \chi(\sigma) \quad (4)$$

with

$$\alpha = \sqrt{\frac{m^* \omega}{\hbar}} \quad (5)$$

where n is the radial quantum number, m_z is the azimuthal angular momentum quantum number, $L_n^{|m_z|}$ is the associated Laguerre polynomial and $\chi(\sigma)$ is the eigenstate of the spin operator \hat{S}_z .

The Hamiltonian can be rewritten as $\hat{H} = \hat{H}_0 + \hat{H}_1$; where

$$\hat{H}_0 = -\frac{\hbar^2}{2m^*} \nabla_{\rho}^2 + \frac{1}{2} m^* \omega^2 \rho^2 + \frac{1}{2} \hbar \omega_c (\hat{L}_z + g \hat{S}_z) \quad (6)$$

$$\hat{H}_1 = -\frac{1}{2} m^* \omega_0^2 \rho^2 - V_0 e^{-\frac{\rho^2}{2R^2}} \quad (7)$$

and ω^2 is the effective frequency, defined as:

$$\omega^2 = \omega_0^2 + \frac{1}{4} \omega_c^2 \quad (8)$$

where \hat{H}_0 represents the harmonic oscillator Hamiltonian with well-known eigenstates $|nm_z\rangle$ and with energies of $E_n = (2n + |m_z| + 1) \hbar \omega + \frac{1}{2} \hbar \omega_c (m_z + g S_z)$.

We can write the matrix elements of the complete Hamiltonian \hat{H} in terms of these bases $|nm_z\rangle$ using Eq. 4, as:

$$\begin{aligned} \langle n' m_z | \hat{H} | n m_z \rangle &= \langle n' m_z | \hat{H}_0 | n m_z \rangle + \langle n' m_z | \hat{H}_1 | n m_z \rangle \\ &= (2n + |m_z| + 1) \hbar \omega + \frac{1}{2} \hbar \omega_c (m_z + g S_z) + \langle n' m_z | \\ &\quad - V_0 e^{-\frac{\rho^2}{2R^2}} | n m_z \rangle - \langle n' m_z | \frac{1}{2} m^* \omega_0^2 \rho^2 | n m_z \rangle \end{aligned} \quad (9)$$

The matrix element for the Gaussian confinement potential $\langle n' m_z | -V_0 e^{-\frac{\rho^2}{2R^2}} | n m_z \rangle$ can be evaluated in a closed form by using the following Laguerre relation [16]:

$$\int_0^{\infty} t^{\alpha-1} e^{-pt} L_m^{\lambda}(at) L_n^{\beta}(bt) dt = \frac{\Gamma(\alpha)(\lambda+1)_m (\beta+1)_n p^{-\alpha}}{m! n!} \sum_{j=0}^m \frac{(-m)_j (\omega_j)}{(\lambda+1)_j j!} \left(\frac{a}{p}\right)^j \sum_{k=0}^n \frac{(-n)_k (\alpha+j)_k}{(\beta+1)_k k!} \left(\frac{b}{p}\right)^k \quad (10)$$

This closed form reduces significantly the computation time needed in the diagonalization process.

Statistical Energy, Magnetization and Magnetic Susceptibility

We have used computed energies of the GQD system as essential data to calculate the statistical average energy as:

$$\langle E(T, B, R, V_o) \rangle = \frac{\sum_{\alpha=1}^N E_{\alpha} e^{-\frac{E_{\alpha}}{k_B T}}}{\sum_{\alpha=1}^N e^{-\frac{E_{\alpha}}{k_B T}}} \quad (11)$$

which describes the mean thermal energy of the electron.

The magnetization of the GQD system is evaluated as the magnetic field partial derivative of the mean energy of the GQD.

$$M(T, B, R, V_o) = \frac{-\partial \langle E(T, B, R, V_o) \rangle}{\partial B} \quad (12)$$

The magnetic susceptibility of the GQD system is evaluated as the second magnetic field derivative of the mean energy of the DQD.

$$\chi(T, B, R, V_o) = -\frac{\partial^2 \langle E(T, B, R, V_o) \rangle}{\partial^2 B} \quad (13)$$

3. Results and Discussion

We present our computed results for the energy spectra by solving the single electron GQD Hamiltonian using numerical diagonalization method and Fock-Darwin bases. The material parameter for GaAs medium is taken to be $m^* = 0.067m_0$; the effective Rydberg of $R^* = 5.83\text{meV}$ and Bohr radius of $a^* = 9.8\text{ nm}$ are used as energy and length, respectively. The energy spectra, E_n , are essential input data to calculate magnetization and magnetic susceptibility. Diagrams were used to illustrate the results.

Quantum Dot Energy Spectra

First, we calculate the ground state energy of the QD for fixed potential height (V_0) and different QD radii, as displayed in Fig. 1.

We show in Fig. 2 the ground state and few excited state energies of the Gaussian QD *versus* the magnetic field B. The figure shows clearly the effects of the Zeeman and the spin terms on each particular state. As the magnetic field increases, the spin and Zeeman terms show significant energy contribution effects. These results are in full agreement with the previous published results of Boyacioglu and Chatterjee [38].

Next, we found the average thermal energy of the ground state of the QD as in Fig. 3. This figure describes the average thermal energy $\langle E \rangle$ *versus* the magnetic field for GQD, taking into account the effect of the electron spin term.

Fig. 3 shows that at low temperature of 5mK, the energy decreases as the magnetic field increases, because at low temperatures, the thermal energy contribution is small, so the negative energy contribution due to the spin term ($\omega_c g^* \hat{S}_z$) is significant and reduces the statistical energy; this behavior continues up to $B \approx 4\text{ T}$, then the energy starts increasing as the magnetic field increases. As the temperature increases, from 5mK to 10 and 20 K, the ground state energy curve of the QD shows a great enhancement. This behavior is due to the significant increment in the thermal energy contribution.

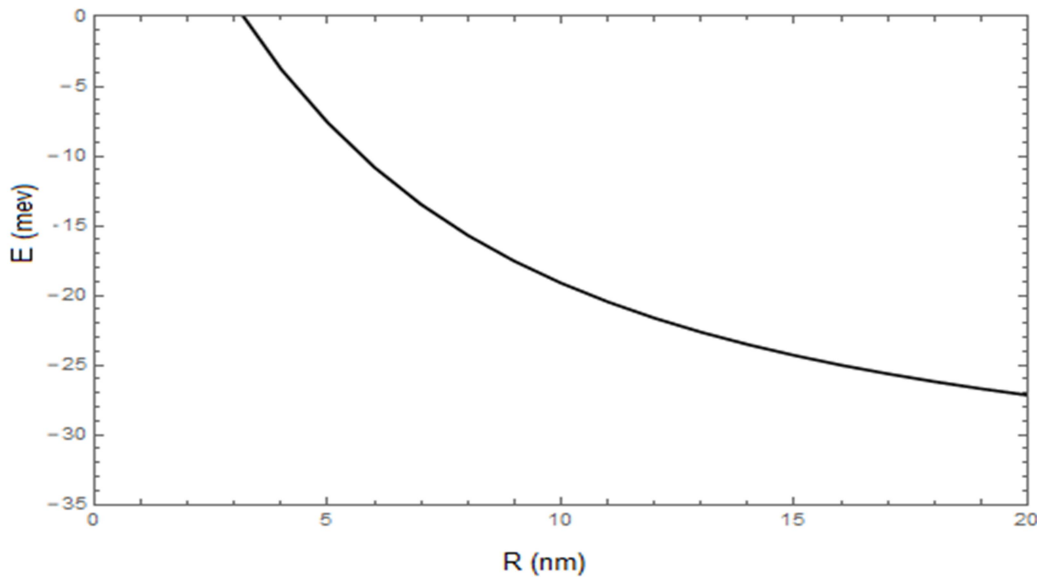


FIG. 1. The calculated ground state energy of a single electron quantum dot as a function of the quantum dot size R at zero magnetic field $B = 0$ and $V_0 = 36.7\text{meV}$.

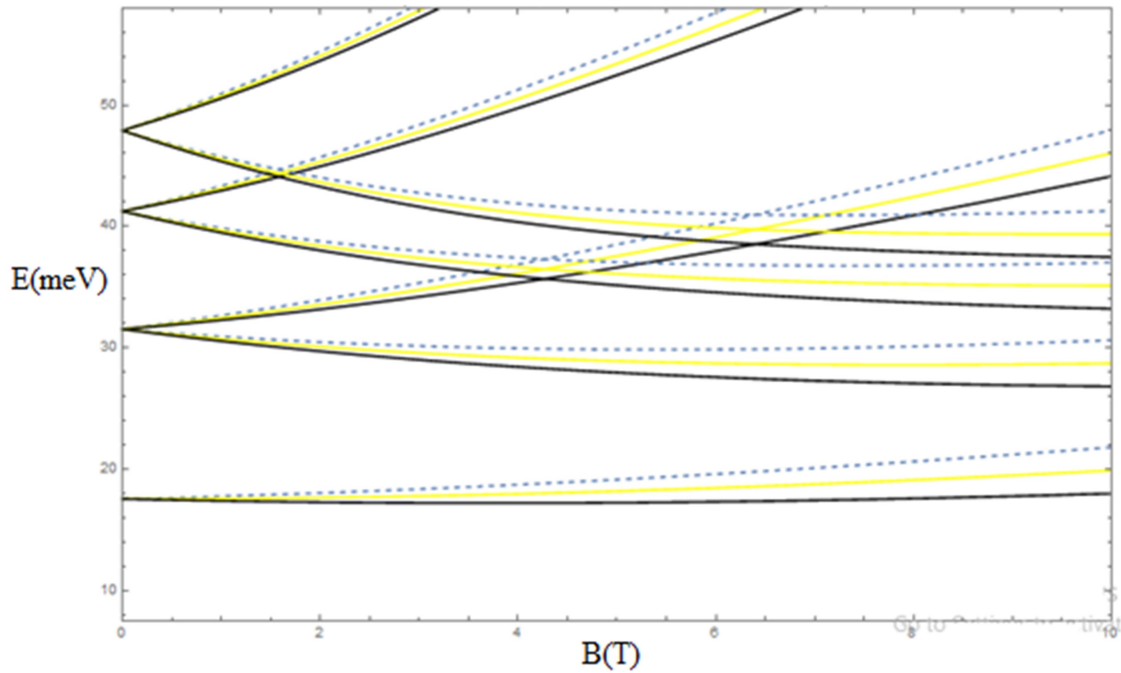


FIG. 2. Computed ground and first few excited energy states of one electron GQD *versus* the magnetic field at $V_0 = 36.7$ meV and $R = 10$ nm. The dashed curve is for $S = -1/2$ and the solid curve is for $S = 1/2$.

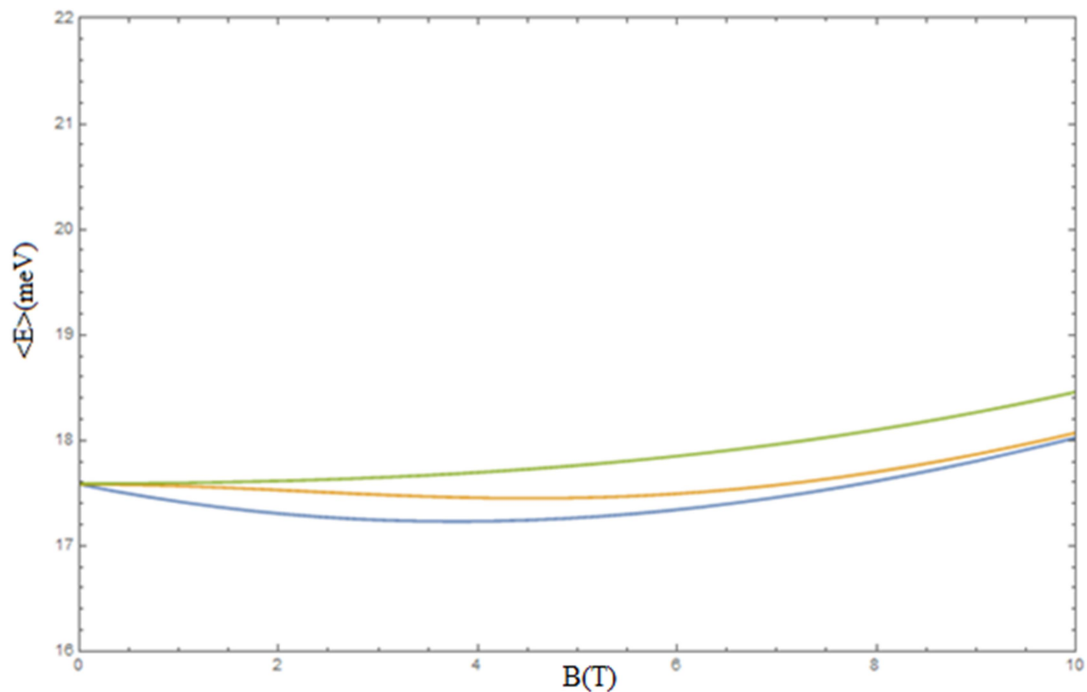


FIG. 3. The average thermal energy *versus* the strength of the magnetic field B at $V_0 = 36.7$ meV, $R = 10$ nm, $g^* = -0.44$ and $T = 5$ mK, 10 and 20 K, from bottom to top.

In Fig. 4, we show the dependence of the convergence of our GQD energy spectra on the temperature by plotting the average energy *versus* the temperature at constant $B = 2$ T for $R = 10$ nm and $V_0 = 36.7$ meV and various numbers of bases (n) used in the exact diagonalization process. It is clear from the figure that, to reach

numerical stability, we need more bases as the temperature increases. To achieve very good numerical stability calculations, we raised the number of bases to more than 90, at high temperature, as shown. This behavior is also supported by the results of a recent work reported by Nammias [34].

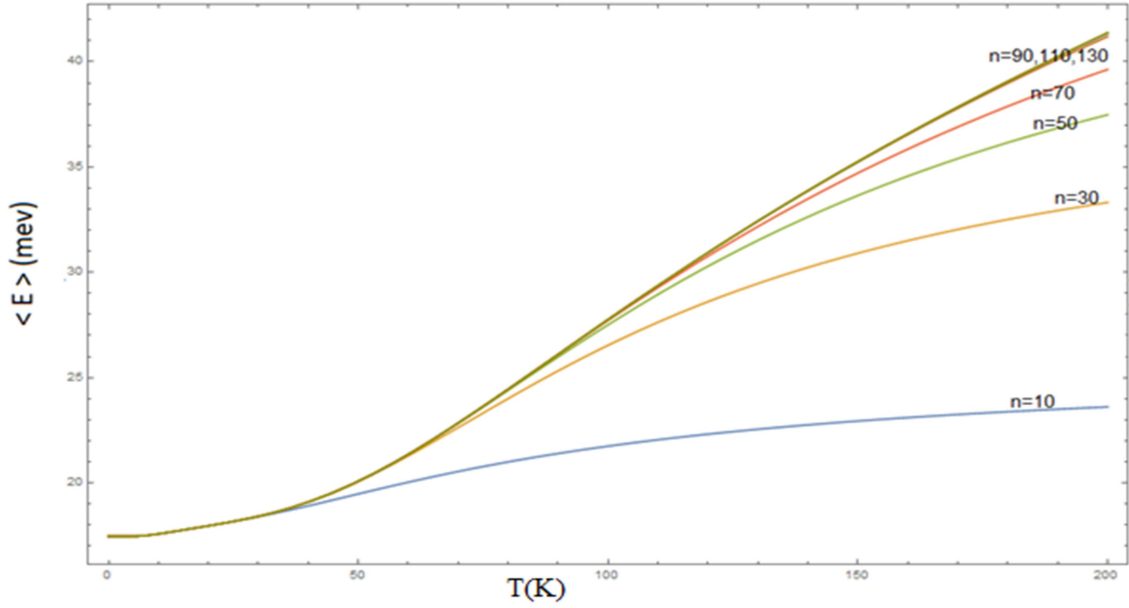


FIG. 4. Average thermal energy $\langle E \rangle$ against temperature T at $V_0 = 36.7$ meV, $R = 10$ nm, $g^* = -0.44$, $B = 2$ T and $n = 10, 30, 50, 70, 90, 110$ and 130 .

Magnetization

In this section, we will present and discuss the computed results for the behavior of magnetization (M) as a function of QD physical parameters of a single electron QD confined by a Gaussian potential. Magnetization was calculated by using the computed eigenenergies of a confined electron in a QD, as essential input data.

In Fig. 5, we present the dependence of M on B for fixed values of the confinement depth V_0 and quantum dot radius R , at different temperatures, T .

By focusing on the results obtained in the figure, we observe that at low temperatures ($T=5$ mK, 5 K and 10 K), magnetization M has the following behavior: magnetization increases as the magnetic field B increases, reaching a peak value, then it starts decreasing. As the temperature increases, the peak value in the magnetization curve decreases and the curve becomes flat. For example, at high temperatures of $T=20$ K and 30 K, the thermal energy ($E_{th} = k_B T$) becomes very significant and in this case, it affects greatly the average energy behavior of the system, as shown in Fig. 3. This leads to a linear decrease in the magnetization curve against the magnetic field.

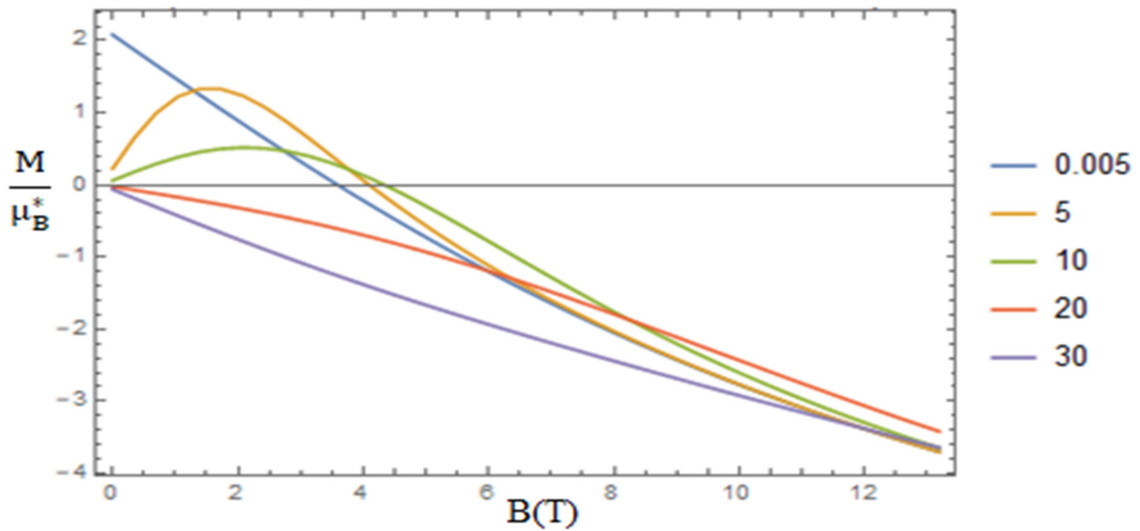


FIG. 5. Magnetization, per effective Bohr magneton $\frac{M}{\mu_B^*}$, against the strength of the magnetic field B at $V_0 = 36.7$ meV, $R = 10$ nm and $T = 0.005, 5, 10, 20$ and 30 K.

Fig. 6 shows the effect of the confining potential depth V_0 on the variation of the magnetization curve. As the potential depth V_0 increases, magnetization increases. This behavior of magnetization is due to the negative energy contribution of the Gaussian potential

$(-V_0 e^{-\rho^2/2R^2})$ to the statistical energy $\langle E \rangle$ of the QD. The reduction in the statistical energy leads to an enhancement in magnetization, where $M(T, B, R, V_0) = \frac{-\partial \langle E(T, B, R, V_0) \rangle}{\partial B}$.

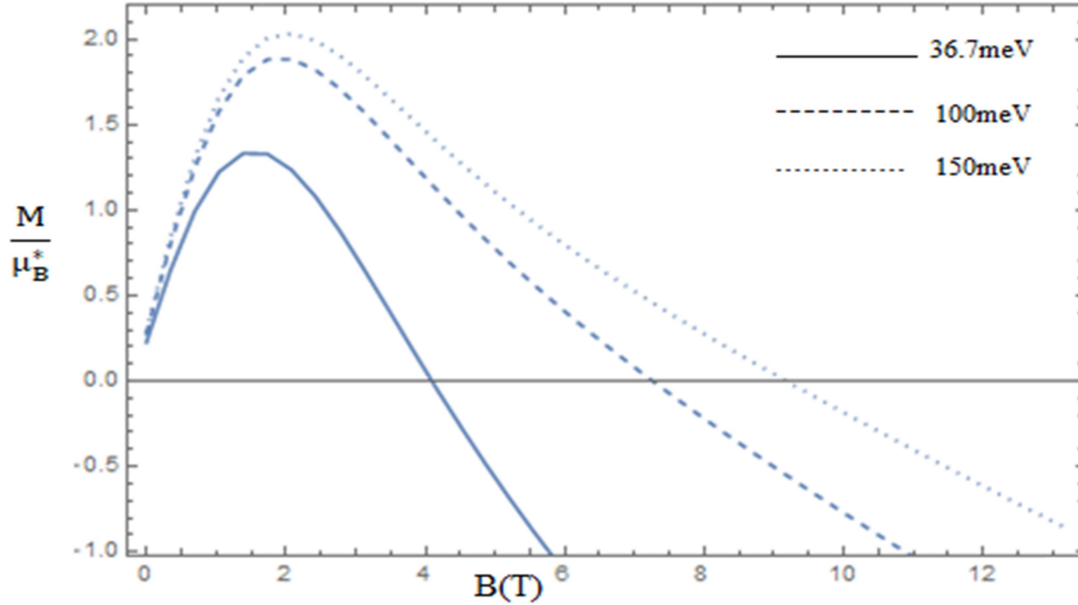


FIG. 6. Magnetization, per effective Bohr magneton $\frac{M}{\mu_B}$, versus the strength of the magnetic field B at $V_0=36.7$, 100 and 150 meV, $R=10$ nm and $T=5$ K.

Magnetic Susceptibility

This section is devoted for the variation of magnetic susceptibility χ as a function of magnetic field B , temperature T , quantum dot radius R and confining potential depth V_0 , of a single electron QD confined by a Gaussian potential. The magnetic susceptibility of the GQD system is evaluated as the second magnetic field derivative of the mean energy of the GQD, as given in Eq. (13); $\chi(T, B, R, V_0) = -\frac{\partial^2 \langle E(T, B, R, V_0) \rangle}{\partial^2 B}$.

In Fig. 7, we present the dependence of magnetic susceptibility on magnetic field B for fixed values of confining potential depth $V_0 = 36.7$ meV and quantum dot radius $R = 10$ nm, at

different temperatures $T = 5$ mK, 5, 10 and 20 K. The figure shows clearly a great change in the behavior of the magnetic susceptibility curves, at each temperature, as we increase the magnetic field strength B . At low temperatures ($T = 5$ mK and 5 K), it is found that at particular values of magnetic field strength, magnetic susceptibility (χ) flips its sign from positive ($\chi > 0$) to negative ($\chi < 0$); equivalent to a phase change in the QD-media from paramagnetic to diamagnetic. However, at higher temperatures ($T = 10$ K, 20 K), it is observed that the sign of the magnetic susceptibility of the system is negative ($\chi < 0$) for the entire magnetic field range.

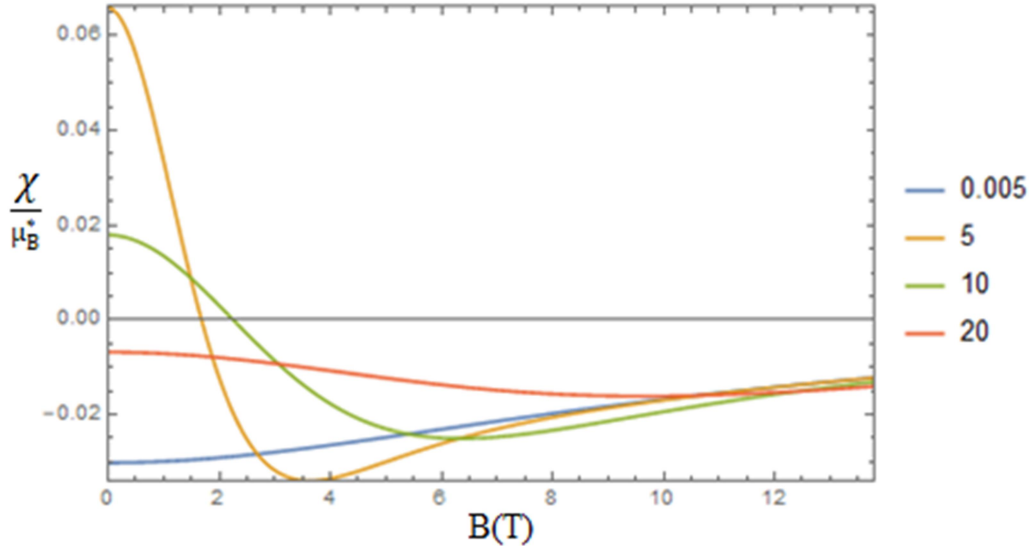


FIG. 7. Magnetic susceptibility, per effective Bohr magneton $\frac{\chi}{\mu_B^*}$, versus the strength of the magnetic field B at $V_0 = 36.7\text{meV}$, $R = 10\text{ nm}$ and $T = 0.005, 5, 10$ and 20K .

Conclusion

The exact diagonalization method has been used to solve the QD Hamiltonian and calculate eigenenergies' spectra, magnetization (M) and magnetic susceptibility (χ) of a single GaAs quantum dot with Gaussian confinement, as a function of the magnetic field strength (B), QD radius (R), confining potential (V_0) and temperature (T). In this work, we have shown the dependence of the energy on the QD radius (R). Next, we have calculated the statistical energy $\langle E \rangle$, taking into account the presence of

the spin (S). The QD-energy results are displayed against the physical parameters of the QD: magnetic field strength (B), QD radius (R), temperature (T) and confining potential (V_0). In addition, we have studied the dependence of magnetization and magnetic susceptibility of the system on the external magnetic field, temperature and confining potential of the GQD. It is found that at certain values of T and V_0 , the QD-system has a magnetic phase change from diamagnetic to paramagnetic.

References

- [1] Ashoori, R.C. et al., Phys. Rev. Lett., 71 (1993) 613.
- [2] Ciftja, O., Phys. Scr., 88 (2013) 058302.
- [3] Kastner, M.A., Rev. Mod. Phys. 64 (1992) 849.
- [4] Loss, D. and Divincenzo, D.P., Phys. Rev. A, 57 (1998) 120.
- [5] Burkard, G., Loss, D. and Divincenzo, D.P., Phys. Rev. B, 59 (1999) 2070.
- [6] Shaer, A., Elsaid, M.K. and Elhasan, M., J. J. Phys., 9 (2016) 87.
- [7] Wagner, M., Merkt, M.U. and Chaplik, A.V., Phys. Rev. B, 45 (1992) 1951.
- [8] Taut, M., J. Phys. A: Math. Gen., 27 (1994) 1045.
- [9] Ciftja, O. and Kumar, A.A., Phys. Rev. B, 70 (2004) 205326.
- [10] Ciftja, O. and Golam Faruk, M., Phys. Rev. B, 72 (2005) 205334.
- [11] Kandemir, B.S., Phys. Rev. B, 72 (2005) 165350.
- [12] Kandemir, B.S., J. Math. Phys., 46 (2005) 032110.
- [13] Elsaid, M., Phys. Rev. B, 61 (2000) 13026.
- [14] Elsaid, M., Superlattices Microstruct., 23 (1998) 1237.
- [15] Dybalski, W. and Hawrylak, P., Phys. Rev. B, 72 (2005) 205432.
- [16] Nguyen, N.T.T. and Das Sarma, S., Phys. Rev. B, 83 (2011) 235322.

- [17] Maksym, P.A. and Chakraborty, T., *Phys. Rev. Lett.*, 65 (1990) 108.
- [18] Helle, M., Harju, A. and Nieminen, R.M., *Phys. Rev. B*, 72 (2005) 205329.
- [19] Bessis, N., Bessis, G. and Joulakian, B., *J. Phys. A*, 15 (1982) 3679.
- [20] Lai, C.S., *J. Phys. A*, 16 (1983) L181.
- [21] Boyacioglu, B. and Chatterjee, A., *Physica E*, 44 (2012) 1826.
- [22] Boda, A. and Chatterjee, A., *Superlattices Microstruct.*, 97 (2016) 268.
- [23] Khordad, R., *Physica B*, 407 (2012) 1128.
- [24] Gharaati, A. and Khordad, R., *Superlattices Microstruct.*, 48 (2010) 276.
- [25] Al-Hayek, I., Sandouqa, A.S., *Superlattices Microstruct.*, 85 (2015) 216.
- [26] Hong, Z., Li-Xue, Z., Xue, W., Chun-Yuan, Z. and Jian-Jun, L., *Chin. J. Phys. B*, 20 (2011) 037301.
- [27] Xie, W., *Superlattices Microstruct.*, 48 (2010) 239.
- [28] Hjaz, E., Elsaid, M.K. and Elhasan, M., *J. Comput. Theor. Nanosci.*, 14 (2017) 1700.
- [29] Bzour, F., Elsaid, M.K. and Shaer, A., *Applied Physics Research*, 9 (2017) 77.
- [30] Elsaid, M. and Hijaz, E., *Acta Phys. Pol. A*, 131 (2017) 1491.
- [31] Elsaid, M., Hjaz, E. and Shaer, A., *Int. J. Nano. Dimens.*, 8 (2017) 1.
- [32] Shaer, A., Elsaid, M. and Elhasan, M., *Turk. J. Phys.*, 40 (2016) 209.
- [33] Shaer, A., Elsaid, M.K. and Elhasan, M., *Chin. J. Phys.*, 54 (2016) 391.
- [34] Nammas, F.N., *Physica A: Statistical Mechanics and Its Applications*, 508 (2018) 187.
- [35] Baghdasaryan, D.A., Hayrapetyan, D.B., Kazaryan, E.M. and Sarkisyan, H.A., *Physica E*, 101 (2018) 1.
- [36] De Groot, J.J.S., Hornos, J.E.M. and Chaplik, A.V., *Phys. Rev. B*, 46 (1992) 12773.
- [37] Boyacioglu, B. and Chatterjee, A., *Int. J. Mod. Phys. B*, 26 (2012) 1250018.

JRTR, the First Research Reactor in Jordan: Results of Commissioning in Light of Safety Enhancement Following Fukushima-Daiichi Accident

Khalifeh AbuSaleem^{a,b}

^a Jordan Atomic Energy Commission (JAEC), Shafa Badran, Amman 11934, Jordan.

^b Department of Physics, The University of Jordan, Amman 11942, Jordan.

Received on: 05/01/2019;

Accepted on: 27/6/2019

Abstract: The Jordan Research and Training Reactor (JRTR) is a multipurpose, 5 MWth upgradable to 10 MWth reactor. Currently, the JRTR is in the operational phase. Prior to the start of JRTR operation, a set of commissioning tests have been performed. The IAEA safety guide NS-G-4.1 has been followed. The commissioning process was divided into three main stages with hold points at the end of each stage. These stages are; tests prior to fuel loading, fuel loading tests and initial criticality tests which include low power tests. The last stage constitutes power ascension tests and power tests up to rated full power. The performed tests proved that all design and performance parameters have been achieved. For instance, the thermal power of 5 MW, maximum thermal neutron flux of 1.5×10^{14} (n/cm².s) and negative reactivity feedback have been achieved. The safety of the JRTR was under extensive inspection from all involved parties. Particular attention has been paid to the lessons learned from the Fukushima-Daiichi accident and the recommendations made by the national regulator, the IAEA, the consultants and the owner. For instance, all safety aspects of the JRTR fall under the category of SC-3 according to the ANSI/ANS 51.1 classification system of nuclear reactors. As examples, the Reactor Structure Assembly (RSA), Primary Cooling System (PCS), Second Shutdown Drive Mechanism/ Control Rod Drive Mechanism (SSDM/CRDM), Reactor Protection System (RPS), Confinement Isolation Dampers, Siphon Breaking Valves and UPS have been classified as Safety Class (SC-3) components. Design changes of systems and equipment due to the reinforced international safety norm, addition, expansion and modification of facilities have been implemented. The quality class of several components, such as Process Instrumentation and Control System (PICS), Radiation Monitoring System (RMS), Information Processing System (IPS) and Operator Work Station (OWS), has been upgraded. Moreover, expansion and modification of facilities to accommodate systems and equipment have been applied. The seismic monitoring system has been improved by upgrading the quality class and by adding a function generating the automatic seismic trip signal when a seismic motion exceeds Operating Basis Earthquake (OBE). Pool liner integrity has been also enhanced. Furthermore, the emergency conditions have attracted special attention. The emergency water storage capacity has been increased and two mobile diesel generators have been placed in a building of seismic category I. This paper is divided into two main parts. The first part presents the commissioning stage of the JRTR as well as the final results and conclusions. The second part describes the safety aspects and the improvements made taking the lessons learned from the Fukushima-Daiichi accident into account.

Keywords: JRTR, Research reactor, Reactor commissioning, Reactor safety.

Introduction

Similar to the goals of commissioning process for all research reactors, the objectives of commissioning of the JRTR are clear and definitive. These include: verifying that the SSCs are commensurate with their importance to safety, demonstrating that the design requirements are met as stated in the Safety Analysis Report [1], providing basic data for safe and reliable operation, verifying that documentation is adequate for full facility operation, providing operation staff with the chance of education for the validity of the reactor operation procedures and providing the end-users with a clear idea about the facility characteristics [2]. It is needless to say that one of the most important objectives of reactor commissioning is to verify the adequacy of facility operation under all anticipated operational modes. The commissioning of the JRTR is significant and of a panoramic importance, as several lessons have been learned from Fukushima-Daiichi accident. Commissioning is a true chance for testing the measures of safety that have been implemented as a result of the discussions between the involved parties. It is important to highlight that the reactor design, development, utilization, nuclear and radiation safety and nuclear security comply with the Jordanian laws and regulations at work. Additionally, the applicable standards and guidelines as set in the International Atomic Energy Agency (IAEA) Safety Requirements, NS-R-4 [3], US NRC report NUREG 1537 PART 1 [4] and Korean regulations and guidelines are used as a top tier requirement. In this context, the concept of defence in depth is applied in the design to provide protection against various reactor transients, including transients resulting from equipment failure and human error and from internal or external events that could lead to a Design Basis Accident (DBA). Particularly, the design of the JRTR satisfies the following criteria:

- The use of conservative design margins, the implementation of a quality assurance program and the organization of surveillance activities;
- The provision of successive physical barriers to the release of radioactive material from the reactor;
- Application of the single failure criterion by ensuring the fulfillment of each of the basic safety functions. The three basic safety functions are: shutting down the reactor, cooling, in particular the reactor core, and confining radioactive material. The essential characteristic functions associated with Systems, Structures and Components (SSCs) must ensure the safety of the reactor. In normal operation, the equipment needed to perform safety functions consist of the operating systems, which must be supplemented by other engineered safety features to perform their functions for anticipated operational occurrences and in DBAs;
- In the design of the safety systems, including engineered safety features that are used to achieve the three basic safety functions, the single failure criterion must be applied;
- Acceptance criteria are established for operational states and for DBAs. In particular, the DBAs considered in the design of the JRTR and selected Beyond Design Base Accidents (BDBAs) have been identified for establishing acceptance criteria. For the design of SSCs, acceptance criteria in the form of engineering design rules have been used;
- Shutting down the reactor and maintaining it in a safe shutdown state for all operational states or DBAs;
- Providing for adequate removal of heat after shutdown, in particular from the core, is included in DBAs;
- Confining radioactive material in order to prevent or mitigate its unplanned release to the environment;
- Inherent safety features, like the appropriate choice of materials and geometries to provide prompt negative coefficients of reactivity have been implemented during the design;
- The use of on-site and off-site emergency plans aimed at mitigating the consequences to the public and the environment in the event of a substantial release of radioactive effluents.

Commissioning of the JRTR

Commissioning Plan

Based on the guidelines of research reactor commissioning in Ref. [2], the commissioning plan of the JRTR has been envisaged to address the objectives of commissioning [5]. The plan defines the objectives of commissioning and the main chapters describe commissioning organization, stages, schedule, management, quality assurance, operational limits and conditions, radiation protection and emergency and security management during commissioning. For the purpose of conducting commissioning activities, the commissioning organization structure has been set. The structure clearly defines the commissioning groups, the functional responsibilities, levels of authority, approval channels and interfaces between the participating groups. Therefore, the organization structure of commissioning has been designed and implemented during the commissioning stage. The organization chart is presented in Fig. 1. It is composed mainly of the management group,

commissioning group, reactor operation group, construction group, quality assurance group, safety and security group and safety committee. The functions and duties are clearly defined in the commissioning plan. For example, the management group, which is chaired by the JAEC Project Manager (PM) consists of KAERI PM who chairs the commissioning safety group, DAWEEO site PM, and JAEC reactor manager. The responsibility of this group is to provide strategic oversight and resources for commissioning, which includes: authorizing the official start of commissioning and declaring the acceptance of commissioning results, reviewing the commissioning plan and monitoring its implementation, following the NCRs and the appropriate corrective actions and coordinating between the commissioning groups. The group also plays a vital role in providing resources and making lines of communication between all relevant groups and parties. For details on the functions and responsibilities, the reader may refer to Ref. [5].

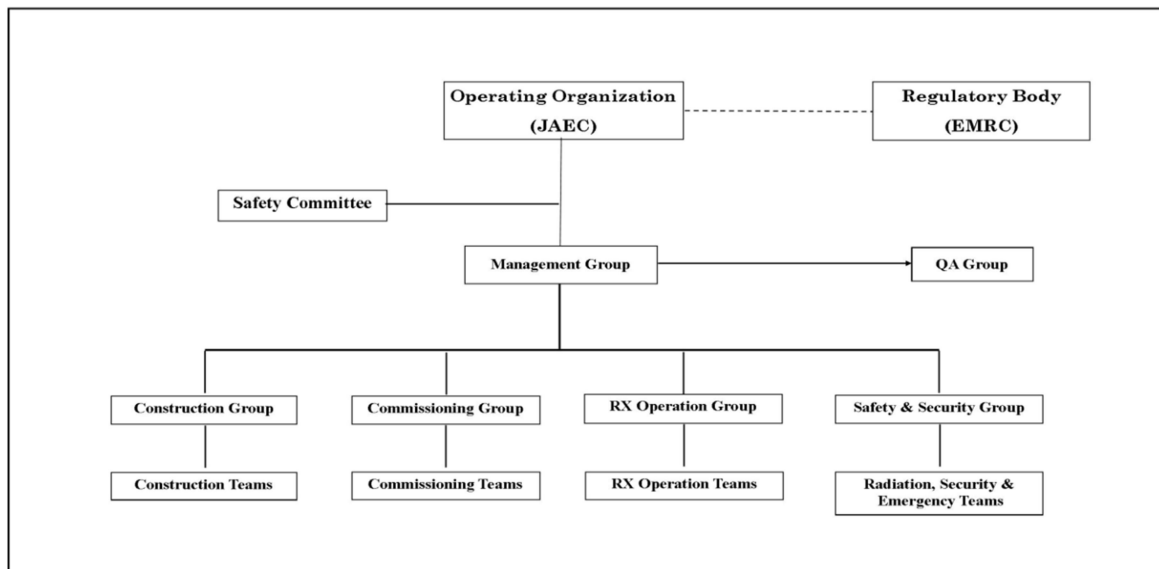


FIG. 1. JRTR commissioning organization structure.

Commissioning Experiments and Results

Following the commissioning plan described in [5], the commissioning activities have been divided into several stages. Preloading commissioning, Stage A, consists of three main stages: Stage A1, Construction Acceptance Tests (CATs), consists of tests distributed over the mechanical, electrical and I&C tests [6], while Stage A2, Flushing and System Performance Tests (SPTs), consists of flushing of the fluid

systems and SPT for the systems reported in Reference [7] and finally Stage A3 [8], which consists of Integrated System Tests (ISTs). This latter stage A3 focuses on the simulation of the reactor operation during power and training modes. These two modes have been tested using simulated reactor power signals. A loss of power scenario also was simulated in this stage A3.

Table 1 presents the major planned hot commissioning experiments. Some of these

experiments belong to the fuel loading and low-power tests (B1 and B2 stages). Other experiments are planned for the power ascension and full power tests (C1 and C2 stage). The initial JRTR core constitutes of 18 FAs with

various uranium densities distributed around the core, as shown in Fig. 2. In this report, a summary of the main hot commissioning tests is presented.

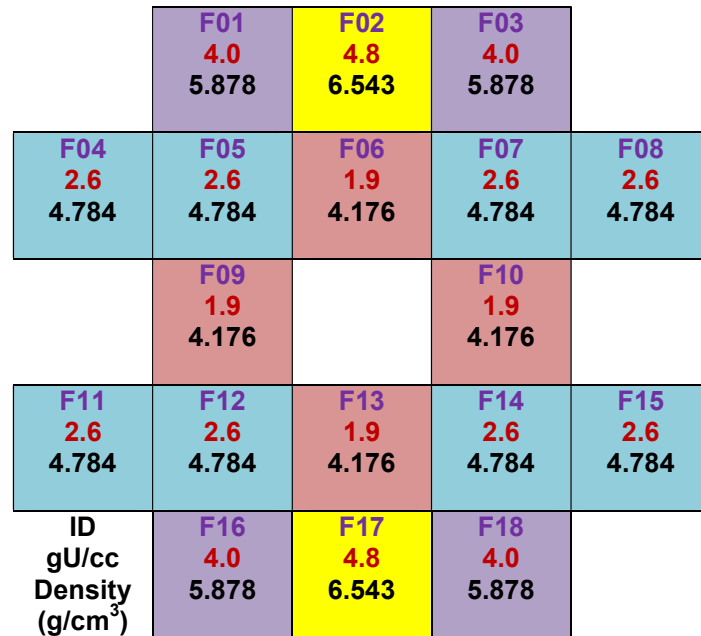


FIG. 2. Sketch diagram representing the JRTR core.

NOTE: Fuel assemblies with identification number and uranium density are illustrated.

TABLE 1. Planned tests for the hot commissioning phase.

NOTE: The stage in which each test is conducted is indicated.

Test	Stage
Fuel loading and approach to criticality	B1
Excess reactivity measurement	B1
CAR/SSR rod worth measurement	B2
Measurement of kinetic parameters	B2
Measurement of void reactivity coefficient	B2
Measurement of flux distribution	B2
Measurement of isothermal temperature reactivity coefficient	B2
Training mode operation	B2
Natural circulation test	C1
Neutron power calibration	C1
Measurement of power reactivity coefficient	C2
Measurement of xenon reactivity	C2
Shutdown and monitoring capability of the SCR	C2
Cooling performance test of PCS and HWS heat exchangers	C2
Cooling tower capacity test	C2
Thermal neutron flux at IR0	C2
NAAF performance test	C2
RI production test	C2
Loss of primary flow test	C2
Loss of normal electric power test	C2
Radiation surveys to determine shielding effectiveness	C1,C2
I&C function tests during operation	C2

Fuel Loading and Approach to Criticality

The test aims at reaching the initial critical core using the 1/M (inverse multiplication) method by insertion of external neutron source in the subcritical core and replacing aluminum dummy fuel assemblies in the core with actual fuel assemblies one by one. For details on the process, the reader can refer to Ref. [9]. The initial critical core is defined as the core having the minimum number of fuel assemblies necessary to achieve criticality. This initial critical core will be expanded to the first cycle operation core by loading additional fuel assemblies at the next test "excess

measurement". The fuel assembly density and order of insertion for the initial core is presented in Table 2. The test also checks whether the initial criticality can be achieved at the initial critical core predicted by calculation.

The results of the test are shown in Fig. 3. In the figure, the count rate of the BF3 detector (counts per second) as a function of time (second) for the CAR position at 570.1 mm for the initial core of 14 fuel assemblies is presented. The reactivity (ρ) is also shown in the figure. The minimum critical core consists of 14 fuel assemblies as presented in Table 2 and the critical CAR position is 570.1 mm.

TABLE 2. Fuel assemblies including the uranium density (gm/cm^3) and order of loading for the initial critical core.

Fuel assembly	Uranium density (g/cm^3)	Order of insertion
F07	2.6	1
F12	2.6	2
F14	2.6	3
F05	2.6	4
F13	1.9	5
F06	1.9	6
F10	1.9	7
F09	1.9	8
F02	4.8	9
F17	4.8	10
F03	4	11
F16	4	12
F01	4	13
F18	4	14

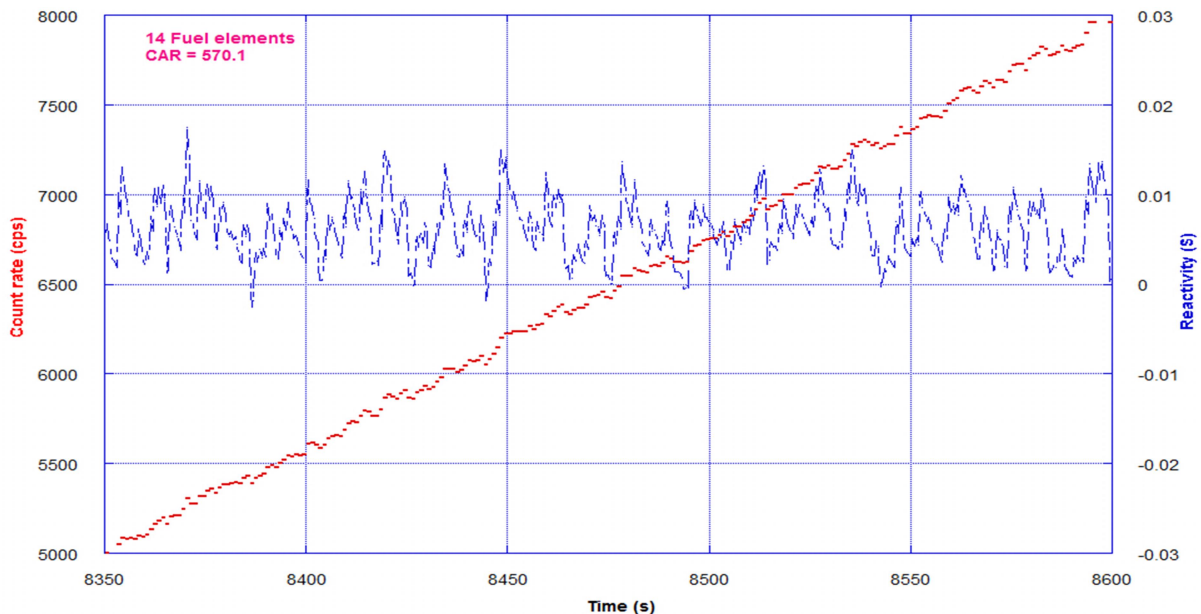


FIG. 3. Count rate of the BF3 detector (cps) as a function of time (s) of the initial core.

NOTE: The initial core is composed of 14 fuel assemblies with a CAR position of 570.1 mm. The reactivity (ρ) is also shown in the figure.

Measurement of Excess Reactivity

The main objective of this test is to measure the inserted reactivity to the first initial operational core by loading additional fuel assemblies to the minimum critical core [10]. In addition, this test confirms that the shutdown margin for the first cycle core satisfies the design specifications. It is worth mentioning that the reactivity (ρ) is defined in connection with the effective neutron multiplication factor (k_{eff}) as follows:

$$\rho = \frac{(k_{eff} - 1)}{k_{eff}}$$

TABLE 3. Measured CAR critical position and total worth for each additional FA after reaching the initial criticality.

NOTE: The last column presents the percentage difference between the measured and the simulated CAR worth.

Additional FA, sequence	Measured CAR position (mm)	Total CAR worth (\$)	% Diff. from the calculated
Critical core, 14	566.6	0.8958	16.09
FA15,1	454.8	2.4866	14.62
FA16,2	399.4	2.150	13.40
FA17,3	346.1	2.8473	13.09
FA18,4	311.5	2.167	11.85

Measurement of Power Reactivity Coefficient

The objective of this test is to evaluate power coefficient of reactivity by measuring the reactivity variation in response to the reactor power change from zero to full power, as well as during the inverse case [11]. When the reactor power is varied, the reactivity change in response is compensated by the change of critical CAR position. Therefore, the power defect can be determined by the reactivity change, which is measured from the change of critical CAR position. Among other factors, if the power is rapidly raised and then descended after a short time of operation at full power, the change of core temperature with fixed core inlet temperature is the major factor determining the power defect. The core temperature is directly affected by the change of the inlet temperature. To minimize the effect of other factors, the reactor power is raised from zero to full power, as well as during the reverse case as fast as possible. The reactivity change in response to the reactor power variation can be measured by adjusting the inlet temperature [11]. The power reactivity coefficient is defined as the reactivity variation per unit power. For the JRTR case, it can be found from:

The fuel assemblies are added to the minimum critical core one by one according to the predetermined fuel loading sequence until the core is fully loaded. Whenever a fuel assembly is added into the core, CARs are withdrawn step by step to approach criticality and 1/M is measured when all CARs are at the same height. The CAR worth, which is a reactivity change caused by a perturbation in a core, is measured from the critical CAR position of the current core to the previous one and hence, the excess reactivity of the new core is determined. The results of this test are presented in Table 3.

$$\frac{\partial \rho}{\partial P} \Delta P = (\rho - \rho_0) - \frac{\partial \rho}{\partial C} \Delta C - \frac{\partial \rho}{\partial X} \Delta X - \frac{\partial \rho}{\partial T} \Delta T$$

where: ρ , ρ_0 , P , C , X and T are reactivity, initial reactivity, power, CAR position, Xenon concentration and inlet coolant temperature, respectively.

Fig. 4 qualitatively shows the measured power defect at the indicated power values during the ascending and descending of power. 10 kW is the reference power defect at zero. These plots have been qualitatively constructed based on the experimental plots in graphs 6 and 7 in ref. [12]. As the figures indicate, power defects measured during power descension are larger than those of power ascension; this behavior can be corroborated to more than one reason, where the relatively rapid rise of core inlet temperature during the 5 MW operation can be one of the reasons [12]. However, during this experiment, the measured power coefficients are confirmed negative for the entire power range. However, the uncertainty in the presented data was not discussed. In the present work, the uncertainty is presented in the last column in Table 4, which gives confidence to the measured parameters.

TABLE 4. Measured power defect during power descending and ascending.

NOTE: The data has been reproduced from the plots in Figures 6 and 7 in Ref. 12. The last column presents the uncertainty as derived in this work.

Descending Power		
Power (MW)	Weighted Average of Reactivity Effect (ρ)	Uncertainty
0.1	-0.00037	± 0.00008
1	-0.01001	± 0.00076
5	-0.08453	± 0.0021
Ascending Power		
3	-0.0425	± 0.00095
5	-0.05713	± 0.00125

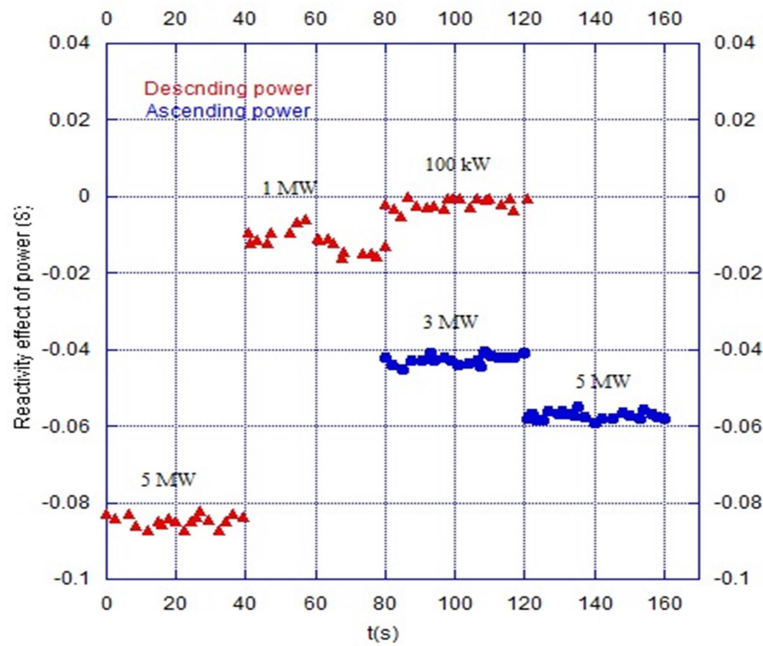


FIG. 4. Qualitative description of the measured power defect as a function of time.

NOTE: The plots represent the measurements during the indicated power values for the ascending and descending of power. The figure has been reproduced from the data presented in Figs. 6 and 7 in Ref. 12.

Thermal Neutron Flux Measurement at IR0

This test is to measure the peak thermal neutron flux at the central irradiation location (IR0) of the JRTR core in order to verify the design criteria. The thermal neutron flux is measured through neutron activation of a cobalt wire contained in a capsule [13]. To perform the irradiation, the capsule is inserted into the expected highest thermal flux position in the IR0 irradiation location. The wires are irradiated for around half an hour when the reactor is operated at the highest nominal power of 5 MW [13]. After irradiation is completed, the reactor is shut down by cutting the electric power for the “loss of normal electric power test”. The irradiated rig is moved to the hot cell to cool off for around one day. The cobalt wires are taken out of the capsules to measure the absolute induced

gamma-ray radioactivity. The wires have been cut to smaller pieces in order to measure the activity of each piece separately.

The number of activated ^{60}Co nuclei $N(t_i)$ is calculated from:

$$N(t_i) = e^{-\lambda t_i} \int_0^{t_i} R(t) e^{\lambda t} dt$$

where $R(t)$ is the measured reaction rate, which is proportional to the reactor power.

For the determination of ^{60}Co activity, the 1332.501 keV peak areas have been used. Fig. 5 and Table 5 present the measured thermal neutron flux as a function of distance from the center of the fuel element and the deduced activities from the least-squares fit of the data

points. As it is evident, the measured flux at the center of the radioisotope production rig is $\sim 1.72 \times 10^{14}$ n/cm².s, which is better than the designed flux of 1.45×10^{14} n/cm².s [14]. Additionally, the linear fit of the data points gives the value of 1.832×10^{14} n/cm².s at the

center of the core, which is even better than the predicted one. The last column in Table 5 presents the new thermal activities at the points of interest. However, it is obvious that the thermal flux is decreasing as a function of distance from the center of the fuel element.

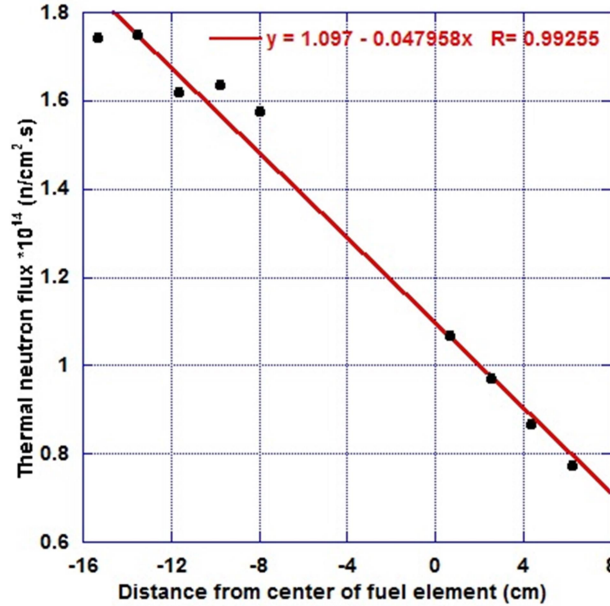


FIG. 5. Deduced thermal neutron flux as a function of distance from the center of the fuel element.

NOTE: The figure represents the measured values as reported in Ref. [14]. The linear fit, the straight line equation and the residue as deduced in the present analysis are also shown.

TABLE 5. Deduced thermal neutron flux as a function of distance from the center of fuel element as reported in Ref. [14].

NOTE: The last column presents the thermal neutron flux as deduced in the present work from the straight line fit.

Distance from vertical center of fuel (cm)	Deduced thermal neutron flux $\times 10^{14}$ (n/cm ² .s)	Thermal flux from linear fit $\times 10^{14}$ (n/cm ² .s)
-15.33	1.743	1.832
-13.49	1.751	1.744
-11.65	1.620	1.656
-9.81	1.636	1.586
-7.97	1.576	1.479
0.67	1.068	1.065
2.51	0.9707	0.977
4.35	0.8674	0.888
6.19	0.7736	0.800
8.03	0.7148	0.712

Neutron Activation Analysis Facility (NAAF) Performance Test

The purpose of this test is to check the performance of the NAAF when the reactor is operating at full power. In particular, the test is designed to verify that the performance of the Pneumatic Transfer Systems (PTSs) and the γ spectrometer meets the design requirements. In

addition, the test will enable to generate key data for the operation of the NAAF and demonstrate that actual NAA can be carried out [15]. The test comprises of transferring and retrieving the tested samples using the three PTSs and measuring the time of each process.

An appropriate weight of Standard Reference Material (SRM) samples has been irradiated for

sufficient times in the NAA1, NAA2 and NAA3 locations. The analysis was carried out using Ge-based spectroscopy system looking for short, medium and long-lived radioisotopes. The measurement results have been compared with certified/reference values.

The conclusion of this test can be summarized as follows: all three PTS lines function as designed. The gamma spectrometry system also functions well. NAA1 provides a high neutron flux with relatively hard spectrum. NAA2 and NAA3 locations provide well-thermalized neutron spectrum with reasonable flux level for the NAA. The JRTR facility can be used for NAA in JRTR with acceptable accuracy [15].

Radioisotope Production Test

The purpose of this test is to check the performance for the production of ^{192}Ir , ^{99}Mo and ^{131}I isotopes at full power operation. This test verifies the maximum radioactivities of a target capsule for ^{192}Ir , ^{131}I and ^{99}Mo that can be produced at JRTR as proposed [16].

The radioisotope production facility of the JRTR has been designed to be capable of producing more than 2000 Ci of ^{192}Ir every two weeks, 10 Ci of ^{131}I a week and 5 Ci of ^{99}Mo a week when the reactor is operating at full power. The neutron activation was carried on ^{192}Ir discs of 3 mm in diameter and 0.25 mm in thickness. For the production of ^{131}I isotope, TeO_2 target with purity higher than 99.9% was irradiated and for the production of ^{99}Mo isotope, MoO_3 targets were used. The details of material, preparation and irradiation procedures are presented in ref. [16].

During the test, it was possible to produce more than 2716 Ci of ^{192}Ir , 14.54 Ci of ^{131}I and more than 8 Ci for ^{99}Mo . The results of these tests demonstrate that the RI facility works as designed.

Conclusions of Commissioning

The JRTR commissioning plan included three main stages. The tests prior to fuel loading, fuel loading tests and initial criticality tests which include low-power tests. The last stage constitutes power ascension tests and power tests up to the rated full power. All planned experiments have been conducted successfully. These experiments verified the design

parameters of the reactor. Particularly, the nominal power, the reactivity feedback, the thermal neutron flux, the radioisotope production facility capability and the performance of the neutron activation facility have been verified to function as designed. Moreover, in some cases, like the thermal neutron flux peak, the radioisotope production capability has exceeded the design prediction. Therefore, the JRTR has been successfully commissioned and is ready to be utilized.

Safety Enhancement of the JRTR in Light of Fukushima-Daiichi Accident

Not like power reactors, the JRTR works under normal temperature and pressure conditions. Therefore, according to the ASMI/ANSI code 51.1 and addenda [17], the Structures, Systems and Components (SSCs) of Safety Class-1 SC-1 and SC-2 are not applicable to the JRTR. Hence, only SC-3 is applicable to the JRTR. For the JRTR, the main nuclear safety functions of the SSC are to [17]:

- Provide secondary containment for the radioactive material holdup, isolation or heat removal with high reliability;
- Remove radioactive material from the atmosphere of confined spaces outside primary containment containing SC-3 equipment;
- Provide or maintain sufficient reactor coolant inventory for core cooling;
- Maintain geometry within the reactor to ensure core reactivity control or core cooling capability;
- Structurally load-bear or protect SC-3 equipment;
- Provide radiation shielding for the control room or offsite personnel;
- Ensure nuclear safety functions provided by SC-3 equipment (e.g., heat removal or provide lubricant for pumps and heat exchangers);
- Provide actuation or motive power for SC-3 equipment;
- Provide information or control to ensure capability for manual or automatic actuation of nuclear safety functions required of SC-3;
- Provide a manual or automatic interlock function to ensure or maintain proper performance of nuclear safety functions required of SC-3 equipment;

- Provide an acceptable environment for SC-3 equipment and operating personnel.

Safety Classification System of the JRTR

The safety classification of the JRTR is based on the classification system presented in Ref. [17]. The SC-3 or NNS classes have been implemented in the JRTR design and relied upon to accomplish nuclear safety functions. The Non-Nuclear Safety (NNS) is defined for equipment not included in any of the SC-3 equipment and is not relied upon to perform a nuclear safety function.

The quality class is designated to design, fabricate, install and test the safety related to the SSCs in accordance with the standards that are appropriate for their intended safety function. Quality classification is generally consistent with safety classification. The quality classification of the SSCs depends on the ASME NQA-1 that classifies the quality to Q, T or S classes [18]. It is worth mentioning that all SC-3 components have been classified as Q class, Seismic Category-I and Class-1E as an applicable electric class.

For SC-3 components, quality assurance program requirements in ANSI NQA-1 [18], or another equivalent program, are applied. Quality

class T is applied to SSCs whose functioning is essential for the normal operation of the reactor, or the failure of which could affect the reliability of the safety class equipment. For this quality class T, selected QA program requirements of quality class Q or QA program requirements of applicable codes and standards are implemented. Quality class S is applied to all SSCs that are not classified as quality class Q or T.

Three seismic categories have been adopted for the SSCs that are essential for the safety of the reactor. SSCs that are required to maintain their integrity and function during and after Safe Shutdown Earthquake (SSE) are categorized as Seismic Category I. SSC components that are required to maintain their structural integrity under load induced by SSE are categorized as Seismic II. Seismic Category III includes SSCs that are not included in either category I or II.

The SSCs that are related to safety functions are classified as electrical class (1E) or electrical non-class 1E (Non-1E). These terms are defined in IEEE Std. 100 [19]. Table 6 presents a partial list of the safety classification system of the JRTR. The table introduces the safety, seismic, quality and electrical classes of the main SSCs.

TABLE 6: Partial list of JRTR SSCs according to safety class, seismic category, quality class and electric class.

System	Safety Class	Seismic Category	Quality Class	Electric Class
Reactor Building Structure	3	I	Q	NA
Reactor Concrete Island	3	I	Q	NA
Reactor Pool Liner	3	I	Q	NA
Fuel Assembly	NA	I	Q	NA
Reactor Structure Assembly	3	I	Q	NA
CRDM	3	I	Q	NA
Spent Fuel Storage Rack	NNS	I	Q	NA
Primary Cooling System	3	I	Q	NA
Secondary Cooling System	NNS	Non	S	NA
Alternative Protection System	NNS	Non	T	Non-1E

Enhancement of the SSCs of the JRTR

After Fukushima Daiichi accident, which was classified by the Japanese Nuclear and Industrial Agency to level 7 at the International Nuclear Event Scale [20], the IAEA revised the safety standards to enhance the safety of nuclear installations. The revised safety standards can be found in the publications of the IAEA. These revised standards can be featured by the following:

- Preventing unacceptable radiological consequences to the general public and environment (Criteria for Beyond Design Basis Accident);
- Preventing long-term off-site contamination (alleviate severe accident);
- Preventing severe accidents and reinforcing design bases.

The JRTR, which was under construction during the Fukushima-Daiichi accident, has been affected by the new international safety standards and norms. However, it is worth to note that the JRTR site is far from the sea shore and cannot be affected by a tsunami. In addition, the core of the reactor is always under a sufficiently large pool of demineralized water compared to the generated heat and always safely cooled naturally and therefore, a similar accident to the Fukushima-Daiichi accident cannot occur. Nevertheless, all recommendations and lessons learned from the Fukushima-Daiichi accident have been adopted and implemented to improve the safety of the JRTR. In the following section, there are examples on the improvements that have been implemented to the JRTR components.

Alternative Protection System (APS)

In the Preliminary Safety Analysis Report (PSAR) [21], the APS was classified as a Non-Nuclear Safety system. However, it is described in the PSAR to act as a diverse protection system to perform prevention and mitigation of anticipated transient without scram. The APS also mitigates the effect of the failure of the Reactor Protection System (RPS). Therefore, the APS has been upgraded to an item important to safety, unlike the original design.

Automatic Seismic Trip System (ASTS)

In the JRTR, the ASTS is the only system that is responsible of safely tripping the reactor, which is in accordance with the NS-R-4 safety standards on the Postulated Initiating Events (PIEs). For this purpose, the system is equipped with 4 seismic sensors and the trip logic is 2 out of 4. Therefore, the seismic monitoring system has been upgraded in terms of the quality class of hardware and software. In addition, a function generating the automatic seismic trip signal when a seismic motion exceeds OBE (Operation Bases Earthquake) has been added. Moreover, the system has been classified as T-class, seismic category I and Non-1E. Additional UPS also has been built in the cabinet so as to store the earthquake-related data.

Emergency Water Supply System (EWSS)

The EWSS is designed to cover the reactor core with water when multiple ruptures of a beam tube occur in order to cool the core for a sufficient period of time. The EWSS injects, by

gravity, the demineralized water from the Demineralized Water Supply Tank (DWST), into the reactor outlet Primary Cooling System (PCS) pipe by opening two parallel Motor Operated Valves (MOVs). Since the multiple ruptures of a beam tube were classified as BDBA, the EWSS was originally classified as a non-nuclear safety system. However, the injection line of the EWSS penetrates the reactor pool liner and is connected to the reactor outlet PCS pipe, which is classified as safety class 3. Since the structural integrity of the injection line part that penetrates the pool liner must be maintained during the motion of the MOVs, the portion of the system between the flow orifice outside the reactor pool and the injection nozzle inside the reactor pool has been classified as a safety class 3 in accordance with case 6(c) of Sec. 3.3.2 Safety Class Interfaces of ANSI 51.1 and has been upgraded to seismic category I, including the MOVs.

Radiation Monitoring System (RMS)

In open-pool type research reactors, most of the critical radiation accidents are closely related to the pool and connected to the primary cooling system. Therefore, the JRTR has been equipped with RMS. The RMS components that are classified to SC-3 are the Reactor Gamma Monitoring System (RGMS), the PCS neutron monitoring system, the PCS gamma monitoring system and the pool radiation monitoring system. The RMS also has been enhanced by adding general-purpose RMS channels, for local radiation dose rate locations that are routinely occupied by operating personnel and other places where changes in radiation levels may occur. These have been classified as NNS and quality class T.

Pool Liner Integrity Enhancement

The stainless steel liner plate of the reactor pool covers the entire internal surface of the pool. The main function of this liner plate is to provide a leak-tight barrier against any possible leakage of pool water. It is worth mentioning that the non-destructive test during the fabrication and installation of pool liner was not possible due to technical reasons. Therefore, the internal integrity of the welded joints has been confirmed by the following additional tests:

- In addition to their qualification tests in accordance with the fabrication procedure, the welders were subjected to practical tests and accordingly certified. Also, weld verification testing was doubly performed.
- For each welding posture of welding angle, a test sample was attached to the actual welding part and welded together with the original part in sequence. Then, the sample was tested to verify integrity.

Air Discharge System (ADS)

In all conditions, the ADS keeps the pressure inside the reactor building negative compared to the outside, so that the air leakage from the reactor building is prevented. In case of emergency, the purpose of the system is to reduce the public dose and to give the management the proper tools to control the path of the released gases [22]. The main components of the system are the building, the filter train, the exhaust fan, the isolation valve, RMS for noble gas, ... etc. Since the ADS is installed in a separate building outside the reactor building and the system should not affect the safety features of the reactor building, safety class (SC-3) valves have been installed at the reactor building penetrations for air exhaust and these are kept closed during normal conditions. Thereby radioactive material leakage to the environment is reduced and monitored. The

exhaust duct is also connected to the reactor stack. Additionally, the ADS building and piping have been upgraded from Seismic class II to I. All other components of the system are classified as NNS, T and II for safety class, quality class and seismic class, respectively. HEPA filter and activated carbon filter are included in the system and hence, the majority of particles and halogens can be filtered out. Because most of the released radioactive material is noble gas, a noble gas radiation monitor has been installed.

Two Mobile Diesel Generators

In addition to the main, 1000 kVA diesel generator, two mobile diesel generators for supplying the necessary power to the load under the emergency situation have been added to the plant. These are with an output of 300 kVA and are accommodated in the ADS building, which is independent of the reactor and is designed to a seismic category I, having sufficient space and an independent entrance for maneuvering the generators.

Additional Upgrades

Other components and equipment have been added to the facility. To accommodate these additions, the total area of the facility has been increased. Summary of the major additions to the building and systems can be found in Table 7.

TABLE 7. Summary of major additions to the JRTR buildings and systems.

Description		Original Proposal	Additional Upgrades
Buildings	Reactor Building	6-story building for the reactor confinement	- Reactor confinement was enlarged from 2,100 m ² to 2,260 m ² . - Additional air lock door.
	Service Building	5-story building consisting of auxiliary areas for operation and RI production	Auxiliary areas were enlarged from 4,700 m ² to 5,600 m ² .
	ADS Building		2-story building containing air discharge system (ADS) and two mobile diesel generators.
	Cooling Tower and Others	- 1 cooling tower with 3 fans - 1 pump house - 1 diesel generator building - 1 fire water tank - 1 stack structure	- 5 closed-type mechanical cooling towers. - 2 Fire water tanks. - 4,700 ton water storage tank.

Description		Original Proposal	Additional Upgrades
Systems	Reactor System	<ul style="list-style-type: none"> - Reactor core and core containing structures - Reactor Protection System - Seismic Monitoring System - Reactor Control and Monitoring System - Radiation monitoring system, ... etc. 	<ul style="list-style-type: none"> - Automatic Seismic Trip System (ASTS). - Quality class upgrading of I&C.
	Primary Cooling System and Connected Systems		<ul style="list-style-type: none"> - Increase of Decay Tank capacity. - Position switches on flap valves. - Siphon break valves. - Reactor pool platform with guide tube. - Pool liner integrity enhancement.
	Supporting Systems	<ul style="list-style-type: none"> - Electrical System Including Emergency Power Supply System - Fire Protection System - Communication Systems - Lighting Systems - Compressed air system 	<ul style="list-style-type: none"> - 2 mobile diesel generators. - Additional field instruments. - Enhanced air compressor.
	HVAC	<ul style="list-style-type: none"> - Reactor building HVAC - RI building HVAC 	<ul style="list-style-type: none"> - Enlarged HVAC and firefighting system. - Air discharge system.
	Others	<ul style="list-style-type: none"> - Fuel and reactor component handling and storage system - Radiation shielding - Radwaste management systems 	<ul style="list-style-type: none"> - Additional seismic support for spent fuel storage rack. - Enhanced lifting utilities. - Additional elevator. - Enhanced spent resin handling. - Enhanced fresh resin handling. - Additional engineering.

Conclusion

Following the Fukushima-Daiichi accident, extensive studies and discussions between JAEC, KDC, Regulator, the IAEA and other consultants have been carried out reassessing the safety features of the JRTR and making sure that the facility implements the lessons learned from

the accident. As a result, several SSCs have been reclassified and upgraded in terms of either safety class, quality class or seismic class. Therefore, the JRTR and the associated facilities are safe during all anticipated operational conditions. In light of these upgrades, the facility has been successfully commissioned.

References

- [1] Final Safety Analysis Report, KDC Team (2014).
- [2] Safety Guide No. NS-G-4.1, Commissioning of Research Reactors, IAEA, (2006).
- [3] Safety of Research Reactors, No. NS-R-4, IAEA (2005).
- [4] Guidelines for Preparing and Reviewing Applications for the Licensing of Non-Power Reactors: Format and Content (NUREG 1537, Part 1), (1996).
- [5] JR-060-KA-443-001 Commissioning-Plan-R9, KDC Commissioning Team (2016), (JAEC internal report only).
- [6] Summary of CAT Results-Stage A1, KDC Commissioning Team (2016), (JAEC internal report only).
- [7] Summary of SPT Results-Stage A2, KDC Commissioning Team (2016), (JAEC internal report only).
- [8] Summary of IST Results-Stage A3, KDC Commissioning Team (2016), (JAEC internal report only).
- [9] JR-066-KC-443-003 R2 Fuel Loading and Approach to Criticality, KDC Commissioning Team (2016), (JAEC internal report only).
- [10] JR-066-KC-443-004 Excess Reactivity Measurement R3, KDC Commissioning Team (201), (JAEC internal report only).
- [11] JR-066-KC-443-013 Measurement of Power Reactivity Coefficient, KDC Commissioning Team (2015), (JAEC internal report only).
- [12] Summary of RPT Results (Commissioning Stage C2 for the JRTR), KDC Commissioning Team (2016), (JAEC internal report only).
- [13] JR-066-KC-443-015 Thermal Neutron Flux Measurement at IR0_R1, KDC Commissioning Team (2016), (JAEC internal report only).
- [14] RPT Report-Thermal Neutron Flux Measurement at IR0, KDC Commissioning Team (2016), (JAEC internal report only).
- [15] JR-066-KP-443-001 R0 NAAF Performance Test, KDC Commissioning Team (2016), (JAEC internal report only).
- [16] JR-066-KP-443-002 RI Production Test Rev.2, KDC Commissioning Team (2016), (JAEC internal report only).
- [17] Nuclear Safety Criteria for the Design of Stationary Pressurized Water Reactor Plants, ANSI N51.1-1983 (R1988).
- [18] ASMI NQA-1-2008, Quality Assurance Requirements for Nuclear Facility Applications.
- [19] Authoritative Dictionary of IEEE Terms, IEEE 1983Std. 100, (2000).
- [20] The International Nuclear and Radiological Event Scale (INES), IAEA publication.
- [21] Preliminary Safety Analysis Report (PSAR), KDC, (2011), (JAEC internal report only).
- [22] Technical Proposal for Air Discharging System, JR-000-KD-400-001 (2014), (JAEC internal report only).

Discrimination of Aerosol Types over Nairobi, Skukuza and Ilorin Using AOD-AE Clusters

S. B. Sharafa^a, B. I. Tijjani^b, R. Aliyu^c, T. H. Darma^b, H. T. Sulu^d and M. M. Bube^e

^aDepartment of Physics, Usmanu Danfodiyo University Sokoto, Sokoto, Nigeria.

^bPhysics Department, Bayero University Kano, Kano, Nigeria.

^cPhysics Department, Kano State University of Science and Technology Wudil, Kano, Nigeria.

^dPhysics/Electronics Unit, Umaru Ali Shinkafi Polytechnic, Sokoto, Nigeria.

^eDepartment of Management Information Systems, Usmanu Danfodiyo University Sokoto, Sokoto, Nigeria.

Received on: 03/02/2019;

Accepted on: 9/9/2019

Abstract: Climatology of aerosols, their trends and classification based on the long-term Moderate Resolution Imaging Spectroradiometer (MODIS) measurements (from February 2000 to July 2015) of aerosol optical depths at 550 nm (τ_{550}) and Angstrom exponent ($\alpha_{470-660}$) using the wavelengths of 470 and 660nm in Nairobi, Skukuza and Ilorin AERONET stations were analyzed in this work. The level-2 collection-6 Deep Blue (L2 C006 DB) of the parameters listed above from the aqua- (MYD04) and terra- (MOD04) MODIS of the study area were statistically analyzed using SPSS. To be able to understand the temporal variation in the characteristics of aerosols in the three stations and during each season separately, MODIS measurements of τ , retrieved for the study area, were compared with AERONET τ . Overall, aqua-MODIS τ corroborate the AERONET measurements well in Nairobi and Ilorin stations with underestimation of 29.80 % and overestimation of 2.90 % respectively, whereas Skukuza station has terra-MODIS τ as the best representation of the AERONET measurements with underestimation of 1.90 %. On seasonal bases, MODIS τ agree well with AERONET measurements during rainy season in Nairobi and Skukuza, with underestimation ranging between 17.20 % and 29.70 % and Ilorin station had overestimation of 7.20 % during dry seasons. Coupled with the fact that the coefficient of determination (R^2) > 0.50, the results suggest that both aqua- and terra-MODIS give a good estimate of τ . τ records presented a unique peak in Nairobi (June), Skukuza (October) and Ilorin (February), while the α monthly mean variability indicated a more complicated behavior with minimum values in Nairobi (June), Skukuza (June) and Ilorin (August). The maximum τ values occurred during dry seasons, while their minimum values occurred during rainy seasons or transition months. The α value showed an opposite behavior to that of τ such that the highest α values occurred during rainy seasons (or transition months) and the lowest values were observed during dry seasons. This behavior may be attributed to the domination of single-mode aerosol particles in each station. Lastly, τ and α values have been employed to identify several aerosol types seasonally and overall.

Keywords: Aerosol optical depth, Angstrom exponent, Terra and Aqua MODIS, AERONET, Validation, Discrimination.

Introduction

Aerosol particles influence climate by modifying both the global energy balance through absorption and scattering of radiation (direct effects) and the reflectance and persistence of clouds and the development and occurrence of precipitation (indirect effects). The term “aerosol” denotes a stable, sparse suspension of microscopic or sub-microscopic solid and/or liquid particles in air. Aerosol particles contribute to numerous other climatically important processes, including fertilization of land and oceans through the deposition of nitrates, iron and other nutrients, acidification of lakes and forests through the deposition of sulfates and nitrates and the reduction of snow and ice albedo through the deposition of black carbon [1]. Reduction in the intensity of a direct solar beam during its propagation through the atmosphere is determined by absorption and scattering processes. These two different mechanisms contribute to extinction of light in the atmosphere from a directly transmitted beam [2].

The Moderate-resolution Imaging Spectroradiometer (MODIS) level II aerosol product (MOD04/MYD04) is the best aerosol optical depth product suitable for near-real-time aerosol data assimilation [3]. MODIS currently provides the most extensive aerosol retrievals on a global basis, but validation is limited to a small number of ground stations [4]. To validate the aerosol retrieval parameters, ground-based measurement data is necessary. The aerosol optical properties retrieved using direct solar radiations from the sun-photometers of the Aerosol Robotic Network (AERONET) are free from surface reflectance error and cloud contamination. Therefore, AERONET dataset is widely used to evaluate the efficiency of satellite based aerosol retrieval algorithm as well as to develop a new algorithm [5]. Several approaches have been proposed for the validation of MODIS aerosol retrieval algorithm for the purpose of renovating and improvement [6,7,8,9]. Kaufman *et al.*[9] proposed the first algorithm which was later modified by Levy *et al.*[10] and Hsu *et al.*[11] by proposing two different methods for aerosol retrieval.

To quantify the effect of atmospheric aerosols, it is necessary to increase our understanding of the subject by studying the spatial and temporal variability of its different

properties [12]. Improvement in measurement capabilities of sensors has increased the amount of aerosol parameters retrieved from space-borne sensors. Several studies have demonstrated aerosol classification using various numbers of aerosol optical and physical parameters derived from passive satellite or ground-based measurements. For example, Kaufman *et al.*[13], Remer *et al.*[14] and Yu *et al.*[15,16] have used the aerosol size information contained in the wavelength dependence of τ retrieved from the space-borne MODIS to retrieve useful information on aerosol types and indeed to help distinguish natural from anthropogenic aerosols.

Discrimination of aerosol types is essential, because several aerosol types originate from different sources having different atmospheric impacts [17]. Aerosol discrimination based on τ_{550} and $\alpha_{470-660}$ scatter plot is useful in classifying different aerosols for a particular location through identifying and interpreting the level of density of τ_{550} and $\alpha_{470-660}$ (cluster) in the scatter diagram. The use of τ_{550} reveals the information about the aerosol density in an atmospheric column, while $\alpha_{470-660}$ gives information about aerosol size distributions. The τ_{550} and $\alpha_{470-660}$ values from the scatter plots can be interpreted together to identify the aerosol types and their frequencies in a particular location quantitatively. These, therefore, make regional studies important, because very different patterns in τ_{550} against $\alpha_{470-660}$ scatter plots have been observed by different authors from different regions of the world [18,19,20]. It is important to note that the $\alpha_{470-660}$ is commonly used due to its nearness to the peak of the solar spectrum and is thus associated with large radiative effect [12,21]. Granados-Munoz *et al.*[12] and Xin *et al.*[21] have used this angstrom values ($\alpha_{470-660}$) against τ_{550} to characterize and classify aerosols in different regions, because the two are indicative of turbidity condition and aerosol types.

The current study provides an attempt on the characterization of aerosols over AERONET stations in Nairobi (Kenya), Skukuza (South Africa) and Ilorin (Nigeria) using MODIS products for periods between the years 2000 and 2015. The study is based on two main objectives. The first is the validation of both aqua- and terra-MODIS τ_{550} with the same parameter from AERONET sensors, while the second is the utilization of τ_{550} and $\alpha_{470-660}$ climatology cluster

analysis to discriminate aerosol types found in the study area over the same period using satellite data.

Data and Methodology

Study Location and Data Acquisition

The connection of two air masses, the impact of which varies during the year with the north-south displacement of the intertropical convergence zone (ITCZ) controls the climate in

West Africa. During November–February, hot and dry continental air masses departing from the high-pressure system over the Sahara Desert offer ascent to dusty harmattan twists over the majority of West Africa. Moist central air masses which originate over the Atlantic Ocean bring annual rainfalls during the months from April to October [22]. The selected study location in West Africa is Ilorin (see Fig.1).

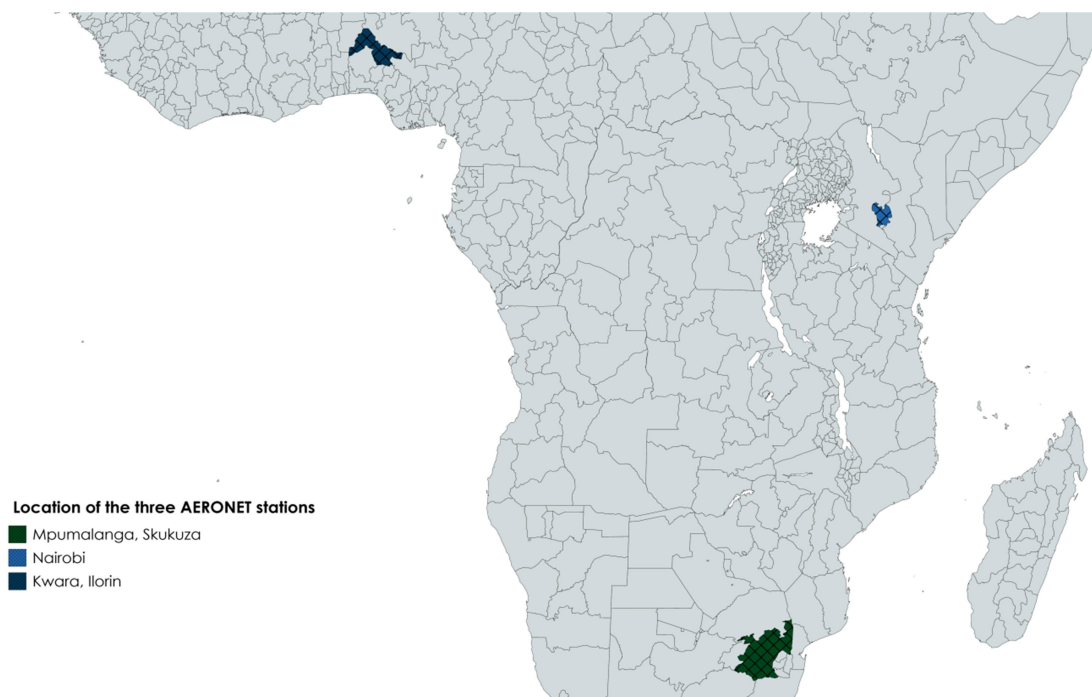


FIG. 1. The map of sub-Saharan Africa showing Skukuza, Nairobi and Ilorin.

East Africa covers different land forms that include glaciated mountains, semi-arid plateaus and coastal regions. The region also consists of inland plains together with forest covers which have been under threat of extinct in the recent past due to wood locking and deforestation. Moreover, the region experiences a distinct bimodal rainfall pattern; i.e., March-April-May (MAM) and September-October-November (SON) (wet season) characterized by low τ values due to enhanced scavenging of aerosols [23]. The bimodal rainfall pattern is influenced by the Inter Tropical Convergence Zone (ITCZ), global oceans, tropical high pressure systems, tropical Monsoons and cyclones [24]. On the contrary, high τ values are noted during dry season; i.e., December-January-February (DJF) and June-July-August (JJA). These high τ values are associated with enhanced aerosol emission from desert and biomass burning events with reduced scavenging of aerosols from the

atmosphere through dry deposition. The selected study location in East Africa is Nairobi (see Fig.1).

The meteorological situation in South Africa is subject to a strong seasonal variability. Above the central Highveld, the atmospheric circulation pattern is dominated by anticyclonic circulation during winter and frequent easterly disturbances during summer. Westerly disturbances take place approximately 20% of the time throughout the year. The precipitation is characterized by strong seasonal variation with practically all precipitation falling during the wet season typically starting in October and ending in March. The precipitation cycle strongly affects local pollutant concentrations *via* primary emissions from wild fires during the dry season, as well as wet scavenging by precipitation and clouds during the wet season [25]. The selected study location in South Africa is Skukuza (see Fig.1).

The climate of the three stations under consideration is mainly characterized by two seasons; namely, dry and rainy. In addition, each station is influenced by various natural and anthropogenic aerosols due to the respective

density of population and high pollution emission resulting in spatio-temporal variation [26]. The distribution of AERONET stations with level-2 data used for this work is shown in Table 1.

TABLE 1. Aeronet stations in the sub-Saharan Africa and their coordinates.

S/No.	Country	Aeronet station	Longitude	Latitude	Altitude	Rainy season	Region
1	Kenya	Nairobi	36°E	1°S	1650 m	March – May and Sept. – Nov.	East Africa
2	South Africa	Skukuza	31°E	24°S	150 m	October - April	South Africa
3	Nigeria	Ilorin	4°E	8°N	350 m	April - October	West Africa

MODIS

The Moderate Resolution Imaging Spectroradiometer (MODIS) is an instrument onboard NASA's Terra and Aqua satellites, which were launched in December 1999 and May 2002 [27], respectively. They are part of NASA's A-Train, a constellation of satellites that provide global daily coverage of the Earth's surface. The coordinated group of satellites allows for near-simultaneous observations of a wide variety of parameters to aid in understanding the Earth's climate. The A-Train is comprised of sun-synchronous near-polar orbiting satellites. Near-polar orbiting satellites pass nearly above the Earth's poles on each revolution and are synchronized with the sun, meaning that each successive orbital pass over the equator occurs at the same local time of the day and at a different longitude. The Terra satellite is on the descending orbit, crossing the equator at 10:30 a.m. local time and the Aqua satellite is on the ascending orbit, crossing the equator at 1:30 p.m. local time. Aqua and Terra fly approximately 700 km above the Earth's surface and with MODIS having a scan angle of $\pm 55^\circ$, MODIS views the Earth with an across-track swath of 2330 km and 10 km along-track. This allows for near global coverage on a daily basis with repeat orbits occurring every 16 days. MODIS is a radiometer that measures the spectral radiance reflected from the Earth-atmosphere system in 36 spectral bands or groups of wavelengths, from the solar to the thermal infrared (0.41 μm - 14.235 μm).

Of the 36 spectral bands, the aerosol retrieval makes use of 7 bands in the shortwave and several others for cloud screening. Processing of the spectral reflectance (R_λ) for use in aerosol retrieval requires several steps. In each MODIS scan (2330 km across-track and 10 km along-track), there are approximately 1354 pixels with

a 1 km channel resolution at nadir view. The number of pixels increases for higher resolution channels (250 m, 500 m). In order to process, the pixels are first averaged into 10 km² boxes with approximately 135 boxes per swath. Once averaged, R_λ are corrected for water vapor, ozone and carbon dioxide using ancillary datasets (MODIS atmospheric profile product (Level 2), allowing isolation of the aerosol signal. Following the correction, observations must be identified as cloudy or clear-sky. If identified as clear, the surface type is determined in order to account for differences in radiance reflection at the Earth's surface as well as differences in aerosol type. The boxes are screened for clouds using the MODIS cloud-mask (Level-2, 10 km² resolution) product. The cloud-mask product is also used for identification of the surface type. If any pixel within a 10 km² box is identified as land, the box is identified as land surface. Otherwise, a box is identified as ocean. Separate retrieval algorithms are used for ocean and land surfaces. A detailed description of pixel selection can be found in Remer *et al.* [14].

AERONET

The Aerosol Robotic Network (AERONET) is a network of approximately two hundred ground-based sun-photometers, which provide globally distributed and continuous observations of atmospheric aerosol properties (<http://aeronet.gsfc.nasa.gov/>) [28]. Observations are cloud-screened and include spectral aerosol optical depth (τ) and Angstrom exponents (α) as well as inversion products relating to aerosol size, such as aerosol optical depth due to fine aerosol and mean and standard deviation of the size distribution.

AERONET instruments measure the extinction of the direct solar beam in eight spectral bands; 340, 380, 440, 500, 670, 870, 940

and 1020 nm. Using the spectral extinction, the atmospheric optical depth is determined using the Beer-Lambert Law (Equation 1). Attenuation of the beam due to Rayleigh scattering and absorption by ozone and other gaseous pollutants is estimated and removed to isolate the aerosol optical depth. Measurements of aerosol optical depth by AERONET instruments are quite accurate because of the use of the direct solar beam. Possible offsets in solar channel calibration are expected to generate a wavelength-independent absolute uncertainty in AERONET τ at the level of ± 0.01 [28]. This is more accurate than MODIS τ observations, which require information about surface reflectance properties that are not well quantified. As a result of low uncertainty, AERONET measurements are commonly used for validation of aerosol forecasts and satellite observations. In addition to τ , AERONET reports α , calculated using AERONET τ values for all available wavelengths (870, 670, 500 and 440 nm).

$$I_{\lambda} = I_{\lambda_0} e^{-m\tau_{tot,\lambda}} \quad (1)$$

where I_{λ} is the observed spectral direct beam irradiance at wavelength λ , I_{λ_0} is the extraterrestrial solar spectrum corrected for the actual Sun-Earth distance, m is the optical air mass and $\tau_{tot,\lambda}$ is the wavelength-dependent total optical depth (Kaskaoutis and Kambezidis, 2006; Masoumi et al., 2010 (as seen in Al-Salihi [29])).

Methodology

Aerosol Robotic Network (AERONET) and Moderate Resolution Imaging Spectroradiometer (MODIS) data was used in this work. The data was downloaded from the website of Multi-sensor Aerosol Products Sampling System (MAPSS) (<http://giovanni.gsfc.nasa.gov/mapss/>). It provides a consistent sampling approach that enables easy and direct inter-comparison and ground-based validation of the diverse aerosol products from different satellite sensors in a uniform and consistent way [30].

To characterize inconsistencies and bridge the gap that exists between aerosol sensors, MAPSS was established. The platform has consistently been sampling and generating the spatial statistics (mean, standard deviation, direction and rate of spatial variation and spatial correlation coefficient) of aerosol products from multiple spaceborne sensors, including MODIS (on Terra and Aqua), Multi-angle Imaging

Spectroradiometer (MISR), Ozone Monitoring Instrument (OMI), Polarization and Directionality of Earth Reflectances (POLDER), Cloud Aerosol Lidar with Orthogonal Polarization (CALIOP) and Sea-viewing Wide-of-view Sensor (SeaWiFS). Samples of satellite aerosol products are extracted over Aerosol Robotic Network (AERONET) locations as well as over other locations of interest, such as those with available ground-based aerosol observations. In this way, MAPSS enables a direct cross-characterization and data integration between Level-2 aerosol observations from multiple sensors. In addition, the available well-characterized co-located ground-based data provides the basis for the integrated validation of these products [30].

The simplest method to quantify the changes in spectral τ is to estimate Ångström parameters (α and β) using Eq. (2) [31,32,33],

$$\tau_{ext}(\lambda) = \beta\lambda^{-\alpha_{ext}} \quad (2)$$

τ is a measure of aerosol loading. Pure atmospheric conditions should be between 0.04 and 0.06 [34]. Ångström exponent (α) provides information on the aerosol size distribution, while the Ångström turbidity coefficient (β) is linked to the columnar mass loading of coarse-mode aerosols.

High α and low β indicate higher quantity of fine mode aerosol concentration. The α value depends on aerosol size distribution and varies from 1 to 3 for fresh and aged smoke and for urban aerosol particles, while it is nearly zero for coarse-mode aerosols, such as dust and sea salt [35]. α can be calculated using Eq. (3) [33,36,37]:

$$\alpha = -\frac{\ln\left(\frac{\tau_1}{\tau_2}\right)}{\ln\left(\frac{\lambda_1}{\lambda_2}\right)} \quad (3)$$

where τ_1 is the aerosol optical depth (AOD) at a reference wavelength λ_1 and τ_2 is the AOD at another wavelength λ_2 .

Data Collection

For the purpose of this long-term analysis, the stations were selected purely based on the availability of an extensive data record. Specifically, calculation of the monthly mean of the parameters (both from AERONET and MODIS) using all-point measurements was carried out. A monthly mean was considered valid only if there are more than five measurements for that month. To ensure a continuous time series, it was required that the

data record should have at least 3 years of AERONET data measurements, with not less than nine monthly data points for each year during the period from 2000 to 2016.

The data collected was aerosol optical depth (τ). The Angstrom exponent (α) was calculated using Eq. (3). The study covers stations in Nairobi, Skukuza and Ilorin; these stations are ideally placed to study the spatio-temporal distribution of coarse (mineral dust) and fine (biomass burning) particles over the region.

Data Analysis

The level-02 collection-06 terra-MODIS aerosol data (MOD04_L2_C006) and level-02 collection-06 aqua-MODIS aerosol data (MYD04_L2_C006) extracted from the Deep Blue (DB) algorithm in MAPSS website was used in this analysis, from which the long-term (2000 – 2015) daily data was obtained. The daily data was used to compute the monthly and seasonal averages over the entire period of study. The dataset was divided into two groups (rainy and dry seasons) based on the seasonal variations used by Anuforom *et al.*[38]. Validation exercise was then carried out using the monthly mean data of τ_{550} from aqua- and terra-MODIS against AERONET after setting the intercept to zero. In choosing the best MODIS sensor for each station, two parameters were observed. One is the slope (which may suggest an overestimation or underestimation) of the regression analysis,

while the other is the coefficient of determination (R^2) which determines the correlation between the two parameters being compared. The large data density for the period makes it easy for the monthly cycle and distribution trends of the parameters to be distinguished. The quantitative analysis of the scatter plots of the $\alpha_{470-660}$ vs. τ_{550} was used for classification. The distribution patterns of different aerosols over the stations were equally investigated seasonally.

Using Table 2, the optical properties of aerosols found in the study area were quantitatively identified based on the scatter plots of the $\alpha_{470-660}$ vs. τ_{550} . It should be noted that because of the overlap between the discrimination parameters of urban and industrial (UI) aerosol and biomass burning (BB), the combination of the two (UI + BB) will be denoted by urban/industrial and biomass burning (UB) in some classifications. Continental aerosols (CAs) are used to denote aerosols such as sea salts, while desert dust (DD) denotes aerosols emanating from arid or desert areas. The distribution patterns of the different aerosols over the study region for the overall and seasonal data were determined. This method was applied to determine the aerosol types for different months and consequently seasons throughout the years.

TABLE 2. Threshold values of aerosol properties for different types of aerosol adopted in this study area.

Type	α	vs.	τ
CA	$\alpha < 0.9$		$\tau < 0.30$
DD	$\alpha < 0.7$		$\tau > 0.40$
BB	$\alpha > 1.0$		$\tau > 0.35$
UI	$\alpha > 1.0$		$\tau > 0.35$

Results and Discussion

Comparisons between τ from the AERONET and MODIS

Figs. 2, 3 and 4 show the correlation plots of both aqua- and terra-MODIS AOD (τ) retrievals against AERONET τ during the years from 2000 to 2015 at the AERONET stations in Nairobi, Skukuza and Ilorin.

Table 3 summarizes the results of the validation of both aqua- and terra-MODIS τ with AERONET τ at the three AERONET stations. It can be observed that aqua-MODIS τ data at

Nairobi station, being underestimated, is relatively better compared with AERONET τ than terra-MODIS τ . The station's aqua-MODIS τ had a lower underestimation (29.80 %) than its terra-MODIS counterpart (35.80 %). On the other hand, in Ilorin station, aqua-MODIS τ was overestimated (by 2.90 %), but better compared with AERONET τ than terra-MODIS τ . Conversely, terra-MODIS τ (also being underestimated by 1.90 %) was closely related to its AERONET counterpart at Skukuza station than aqua-MODIS τ .

Discrimination of Aerosol Types over Nairobi, Skukuza and Ilorin Using AOD-AE Clusters

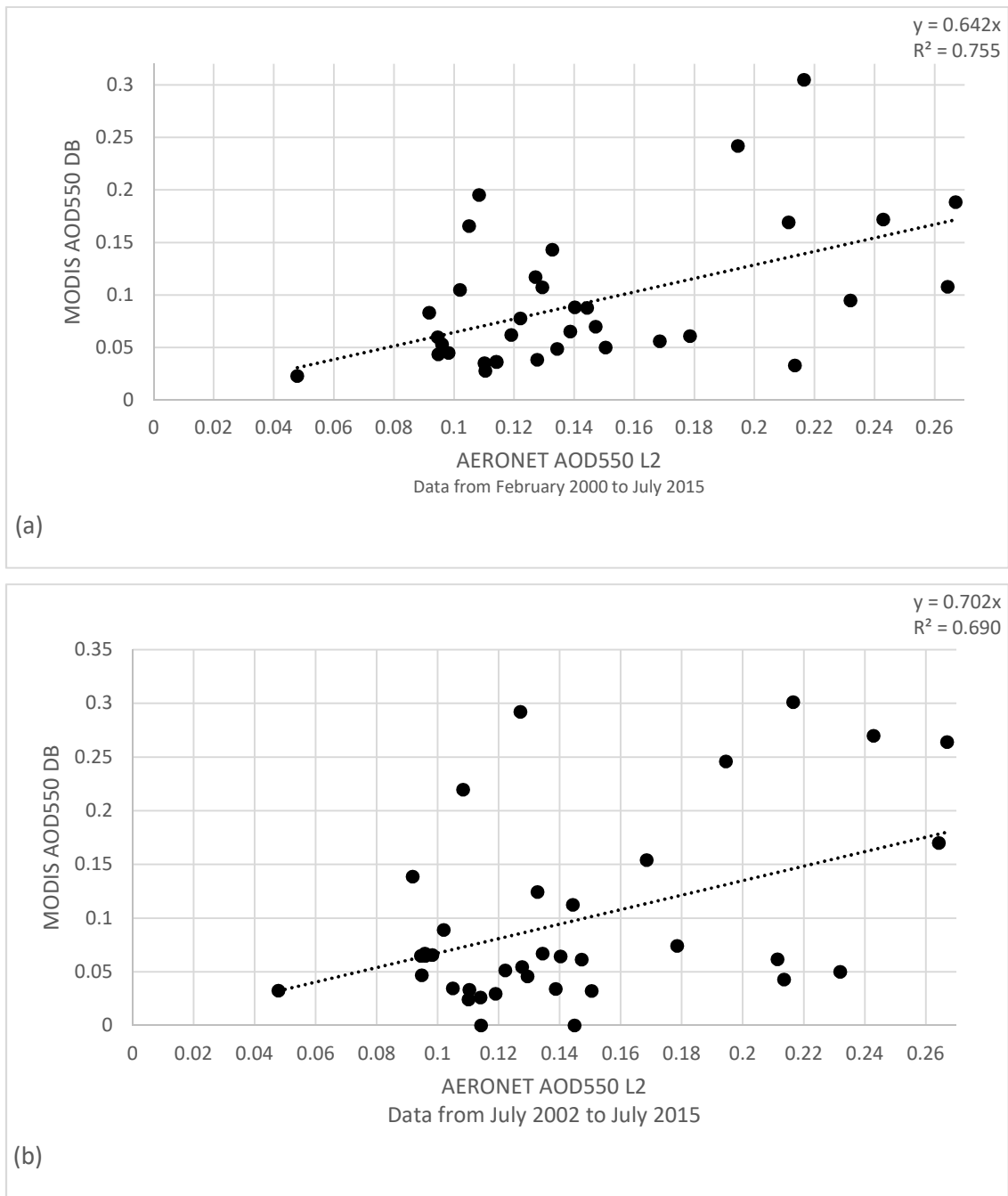


FIG. 2. Comparison of (a) aerosol optical depth (AOD) measured by AERONET and Terra-MODIS and (b) aerosol optical depth (AOD) measured by AERONET and Aqua-MODIS at Nairobi.

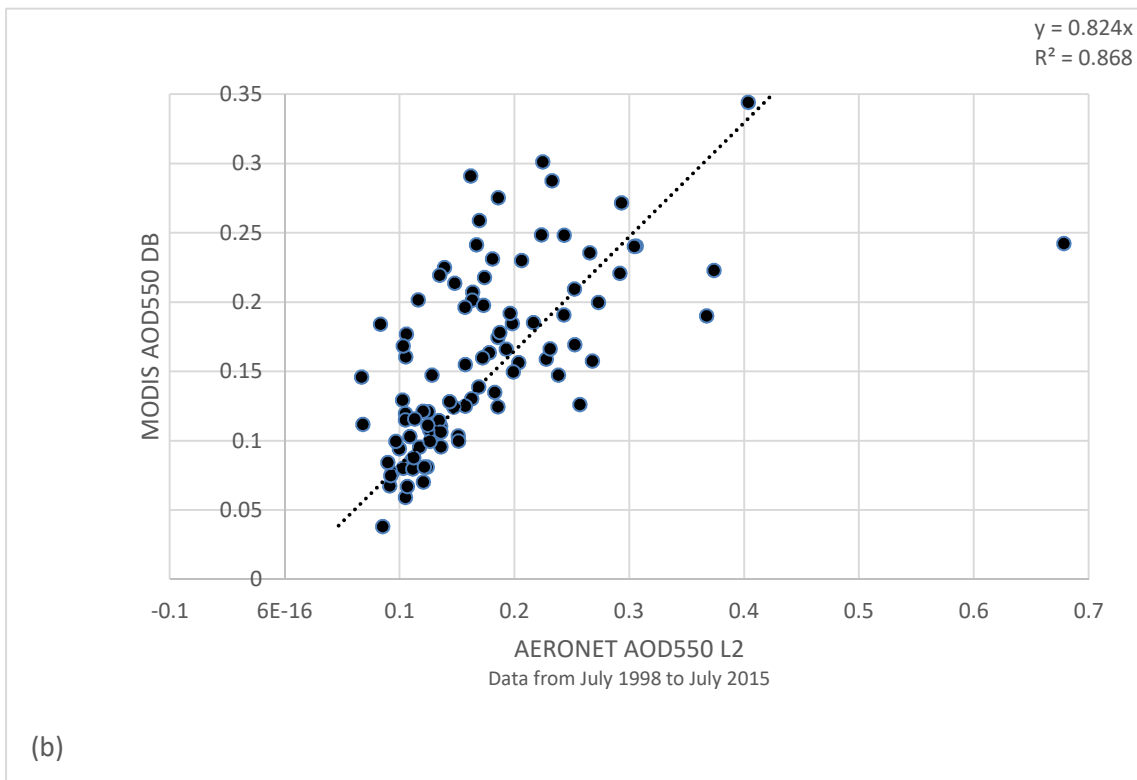
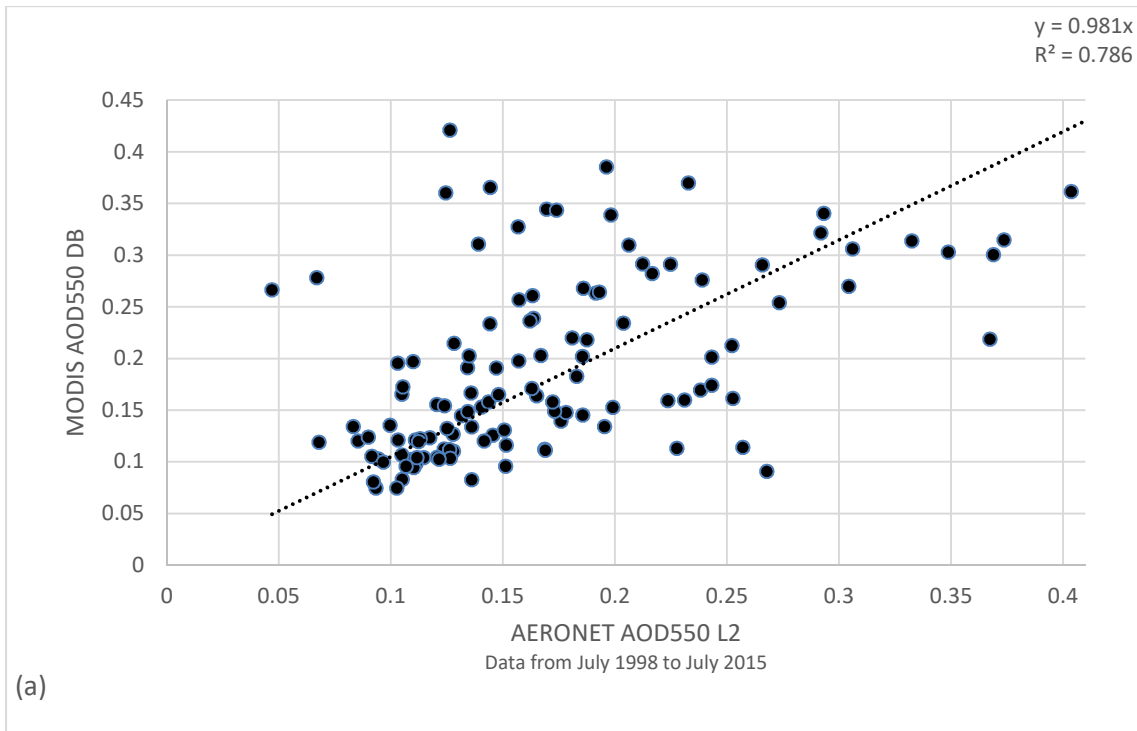


FIG. 3. Comparison of (a) aerosol optical depth (AOD) measured by AERONET and Terra-MODIS and (b) aerosol optical depth (AOD) measured by AERONET and Aqua-MODIS at Skukuza.

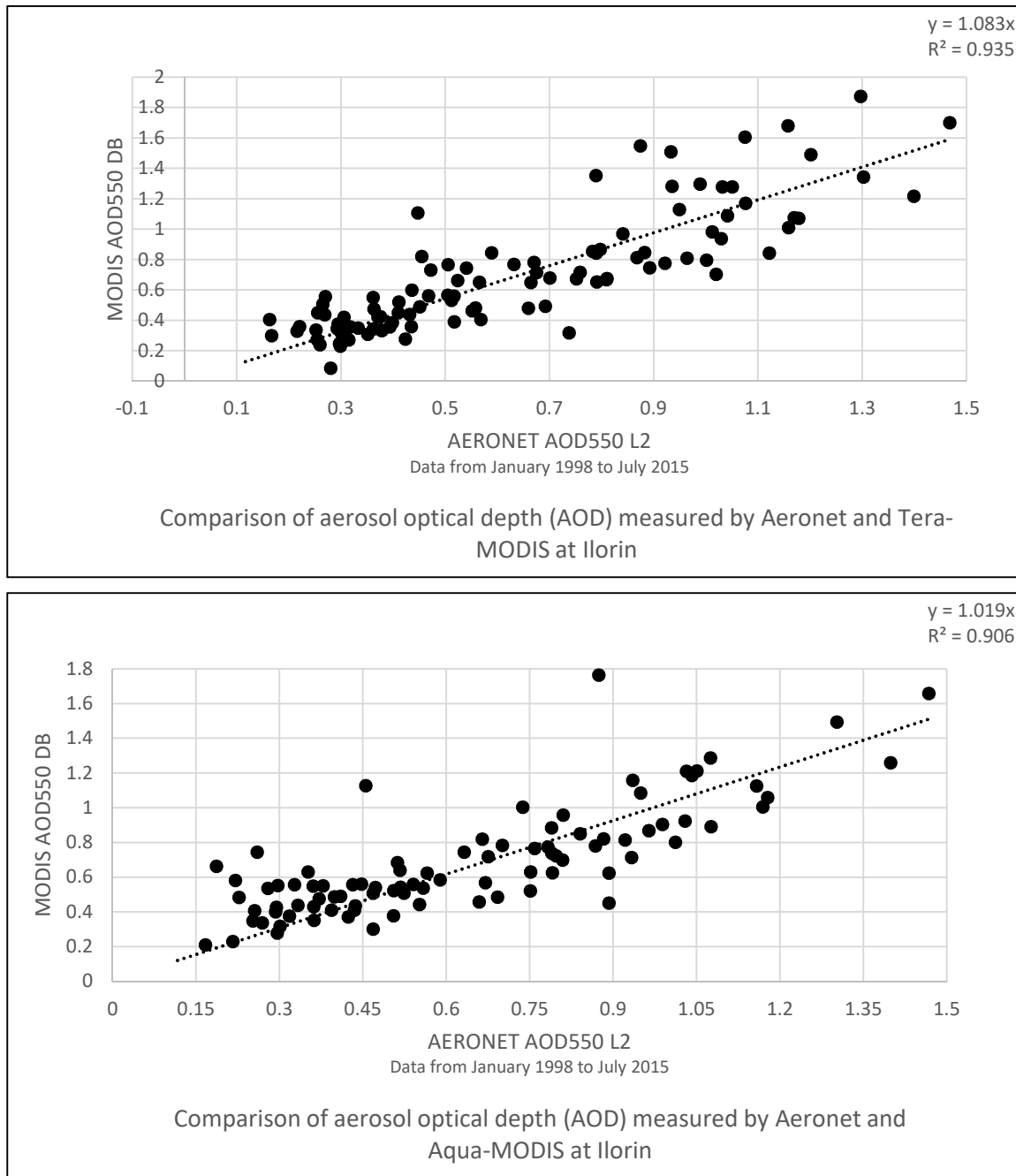


FIG. 4. Comparison of (a) aerosol optical depth (AOD) measured by AERONET and Terra-MODIS and (b) aerosol optical depth (AOD) measured by AERONET and Aqua-MODIS at Ilorin.

TABLE 3. The results of regression analysis for MODIS (aqua and terra) τ vs. AERONET τ for the years (2000 – 2015).

Case	Aqua-MODIS		Terra-MODIS	
	Slope	R ²	Slope	R ²
Nairobi	0.702	0.690	0.642	0.755
Skukuza	0.824	0.868	0.981	0.786
Ilorin	1.029	0.930	1.083	0.935

An R² (between 0.690 and 0.935) observed for the two MODIS sensors indicates that there is good agreement between MODIS and AERONET data. It also provides confidence that

aerosol optical and radiative properties over the study area can be analyzed using MODIS aerosol retrievals.

TABLE 4. The results of regression analysis for MODIS τ vs. AERONET τ during each season across the study area for the years (2000 – 2015).

Case	Dry season		Rainy season	
	Slope	R ²	Slope	R ²
Nairobi	0.499	0.878	0.703	0.751
Skukuza	0.818	0.774	0.828	0.948
Ilorin	1.072	0.951	1.134	0.876

Similarly, Table 4 shows the seasonal validation of the best retrievals of MODIS τ vs. AERONET τ . It could be seen that MODIS τ had better agreement with AERONET τ during the dry season for only Ilorin station (with overestimation of 7.20 %). On the other hand, Nairobi and Skukuza stations' MODIS τ had better agreement with their AERONET counterpart during the rainy season with an underestimation of 29.70 % and 17.20 %, respectively.

Aerosol Climatology of the Study Area

The monthly mean variations of τ_{550} in the atmosphere measured between February 2000 and July 2015 for the study area are shown in Figure 5. It is evident that the mean monthly τ of Nairobi presents roughly intermediate values with the same trend pattern which are the traits of all low-aerosol loading regions. Nevertheless, the atmosphere in this region is a polluted one

(i.e., $\tau > 0.05$). τ values start decreasing in one of the rainy seasons (September to November) and increases significantly during the dry season (January – February). This cycle starts in April, when aerosol concentration begins to build up in the atmosphere; it increases continuously, depicting its peaks in June (a transition month). The month with the highest mean τ is June with a value of 0.17. The month with the lowest mean monthly τ is December (0.047) with a high $\alpha_{470 - 660}$ value (1.42), indicating the presence of anthropogenic aerosol type. It may be any of biomass burning, urban and industrial aerosols or their combinations. These patterns of monthly cycle of τ (increase after rainy season and decrease after dry season) remain consistent during the 16 years of study. The other rainy season brings about an increase in aerosol load. This may be due to episodes of bush burning at the beginning of the rainy season.

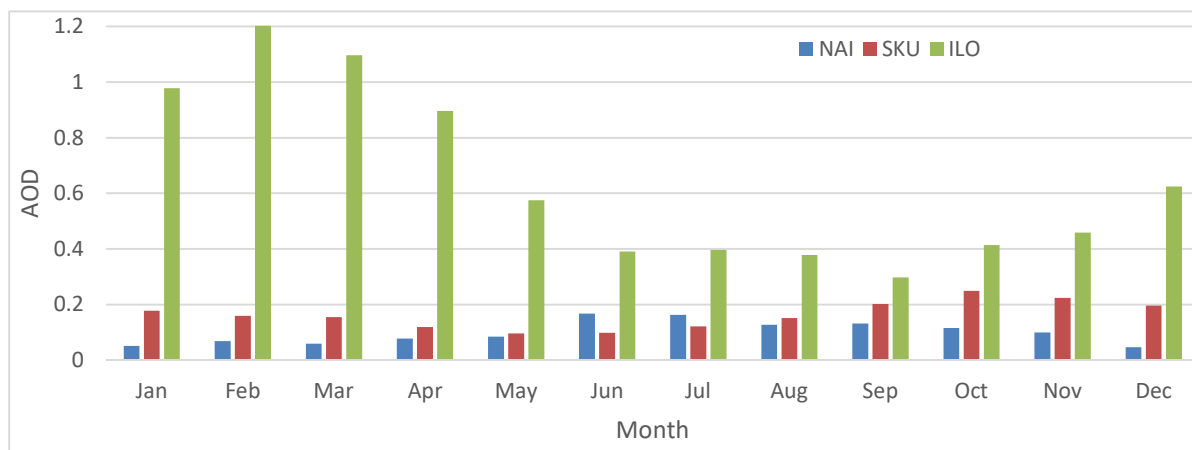
FIG. 5. Monthly mean variations of τ for Nairobi, Skukuza and Ilorin AERONET stations during the study period.

Fig. 5 also shows the variation of the monthly mean τ of Skukuza station and it presents higher values of pollution (though still intermediate). The atmosphere in this region is more polluted than that of Nairobi. The cleanest month is May (0.096). τ values start decreasing in the rainy season (October – May) and increase significantly during the dry season (June – October). The aerosols begin to build up in the

atmosphere in June; they increase substantially until reaching their peaks in September (a transition month). The month with the lowest mean monthly τ is May with a high $\alpha_{470 - 660}$ value, indicating the presence of aerosol types other than dust. It may be any of biomass burning, urban or industrial aerosols or their combinations. These patterns of monthly cycle of τ (increase after rainy season and decrease

after dry season) remain prominent throughout the study period.

Additionally, Fig. 5 indicates the monthly mean aerosol loading pattern in Ilorin station. This station is the most polluted among the three stations. Its cleanest month is September (0.30). τ values start decreasing in the rainy season (March – September) and increase significantly during the dry season (November – February). This cycle starts in October, when aerosol concentration begins to build up in the atmosphere; it increases continuously until reaching its peak in February. The month with the highest mean monthly τ is February with a low $\alpha_{470-660}$ value, indicating the presence of natural aerosol types. It may be any of maritime, biogenic, mineral dust or their combinations. This pattern of monthly cycle of τ (increase after rainy season and decrease after dry season) was observed throughout the study period.

The τ values in Ilorin may be explained by the fact that it is located in a region where dust aerosol is a regular phenomenon. Only Nairobi station, out of the three stations under study, can be said to have a fairly good air quality all year round for having the minimum monthly τ_{550} of 0.047. According to [39], the average τ values under clean background condition should be less than 0.05.

The mean monthly variations of $\alpha_{470-660}$ in the atmosphere measured between February 2000 and July 2015 for the study area are shown in Fig. 6. It is evident that the observed seasonal pattern in Nairobi can be associated with a high concentration of fine mode (anthropogenic) aerosols all through the seasons. The observed high $\alpha_{470-660}$ values, 1.36 (the least) in February to 1.51 (the highest) in June, are signatures of anthropogenic aerosols, which could be associated with biomass burning, urban and industrial aerosols, or a mixture of the aforementioned. The seasonal dependence of τ has resulted in the corresponding seasonal feature of α discussed below. The lowest value of mean $\alpha_{470-660}$ observed in February is a signature of fine-mode aerosols. It increases until its peak is reached in June. Due to frequent rainfall (September – November), a significant amount of the larger particles is washed down from the atmosphere. $\alpha_{470-660}$ remains considerably high in August and maintains a slight dip in values in September before another rise in October, followed by another dip in February. South-westerly trade wind comes with rain, a consequence of which a significant amount of aerosol is being removed from the atmosphere and deposited on the ground. This natural phenomenon causes the $\alpha_{470-660}$ to become large, even during rainy season.

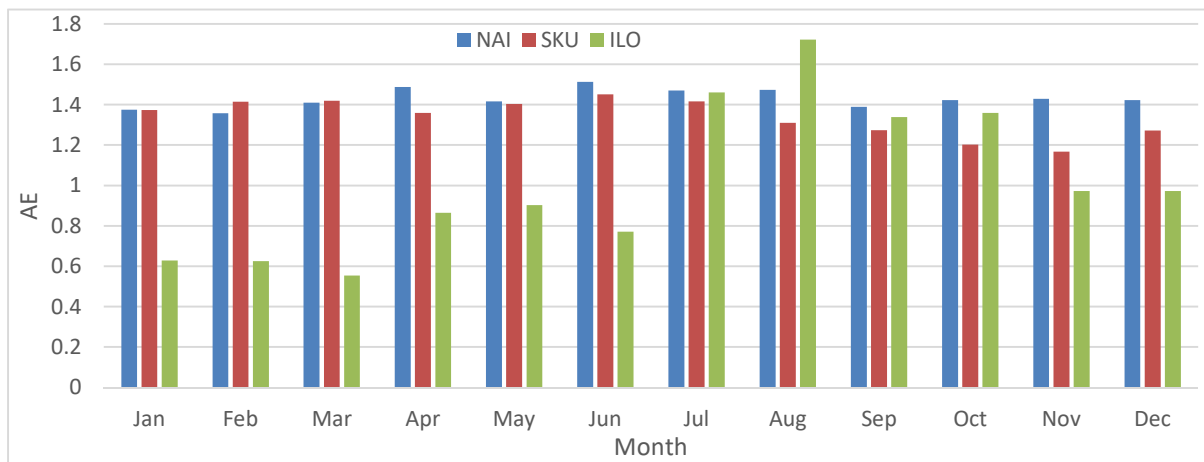


FIG. 6. Monthly mean variations of α for Nairobi, Skukuza and Ilorin AEERONET stations for the study period.

In addition, Fig. 6 shows that the observed seasonal pattern of $\alpha_{470-660}$ in Skukuza can be associated with fairly moderate concentrations of fine-mode aerosols during the dry season. Similar conclusion was drawn by [19] and is supported by our observed low $\alpha_{470-660}$ values, 1.17 in November to 1.45 in June. The values of the mean $\alpha_{470-660}$ observed in the station are signatures of fine-mode particles. It increases

from June until the peak is reached in November due to large and frequent rainfall as a result of which a significant amount of the larger particles is washed down from the atmosphere. $\alpha_{470-660}$ remains considerably high in July and maintains a slight dip in values between August and November before another rise in December. Precipitation brings about a significant reduction

in the amount of coarse-mode aerosols being removed from the atmosphere.

The observed seasonal pattern for Ilorin station (see Fig. (6)) can be associated with fairly moderate concentrations of coarse-mode aerosols during dry season and fine-mode aerosols during rainy season. Similar conclusion was drawn by [19] and is supported by our observed low $\alpha_{470-660}$ values, 0.56 in March to 1.72 in August. The transport of dust aerosol from the Sahara to the station by northeasterly dry wind during dry season has been reported by [40]. The lowest value of mean $\alpha_{470-660}$ observed in March is a signature of mineral dust [41]. It increases from June until the peak is reached in August due to large and frequent rainfall as a result of which a significant amount of larger particles is washed down from the atmosphere. $\alpha_{470-660}$ remains considerably high in September and maintains a slight dip in values in November, followed by an increment in April. A significant amount of coarse-mode aerosols is being removed from the atmosphere as a result of precipitation during rainy season.

Discrimination of Aerosol Types

This analytical discrimination of aerosol types usually requires knowledge about the optical and physical properties that depend on the wavelength. The parameters employed for this discrimination correspond to the descriptive properties of aerosol loading (τ_{550}) and aerosol size ($\alpha_{470-660}$) and this is the most used aerosol discrimination method [20,29,34,42,43,44,45]. To effectively characterize and classify different aerosol types in the sub-Saharan Africa, the threshold criteria provided by Kannemadugu *et al.*[20] were adopted for this work. A lot of literature discussed different aerosol classes, like desert dust (DD), continental aerosol (CA), Urban and Biomass burning aerosol (UB) and Mixed-type aerosol (MT). According to Kannemadugu *et al.*[20], the size distributions are dominated by CA when $\tau_{550} < 0.3$ and $\alpha_{470-660} < 0.9$. For UB, $\tau_{550} > 0.35$ with $\alpha_{470-660} > 1.0$, while DD is represented by a $\tau_{550} > 0.4$ and $\alpha_{470-660} < 0.7$. It should be noted that because of the overlap between the discrimination parameters of urban and industrial (UI) aerosol and biomass burning (BB), the combination of the two (UI +

BB) will be denoted by urban/industrial and biomass burning (UB) in some classifications.

The scatter plots of Figs. 7 (a – c) were analyzed. It was established that different types of aerosols are present in this station. It is obvious from the plots that α shows increasing values with increasing τ , which indicates the presence of fine-mode particles. Also observed is the wide range of values of α (between 0.75 and 1.70) at low τ (≤ 0.40) during rainy season, indicating the presence of different aerosol types under relatively clear atmospheric conditions. Also, the highest number of measurements in the scatter plots for this site is concentrated in the area corresponding to $\alpha_{470-660}$ (1.20 – 1.60) and τ between 0.00 and 0.15, indicating the presence of biomass burning, urban and industrial aerosols. Aerosols from CA and UB with large number of MT are observed in this cluster. Yet, the area corresponding to MT has a very large number of measurements compared to others. This is likely due to the mixing of CA and UB in the atmosphere [39], as well as the absorption of moisture by these aerosols. The CA noticed during rainy season could be as a result of sea salt transport from the Atlantic Ocean, while UB may be as a result of transport sector emissions, biomass burning or urban and industrial aerosol injection events. There are also large numbers of measurements concentrated at $\tau < 0.15$, which are characterized by $\alpha_{470-660} > 1.00$. This is also a case of strong transport sector emission, biomass burning or urban and industrial aerosol injection events. The study further notes similar patterns of aerosol distribution during dry and rainy seasons (Figs. 7 (b) and 7 (c)). MT and UB were noticed during dry season, while CA and MT were present during rainy season.

The relative frequencies of these aerosols are shown in Fig. 8. The MT class was determined as the highest frequency of occurrence (98.33%) in the overall data. This is likely due to the mixture of DD, CA and UB in the atmosphere. The next highest was the UB class (1.11%) and could be as a result of the injection of biomass burning aerosols and those from urban and industrial aerosol injection events. CA is the next most important in this region and it accounts for 0.56% of its aerosol loading. This may be a result of aerosol transport from the Atlantic Ocean. DD aerosol is not present in this station.

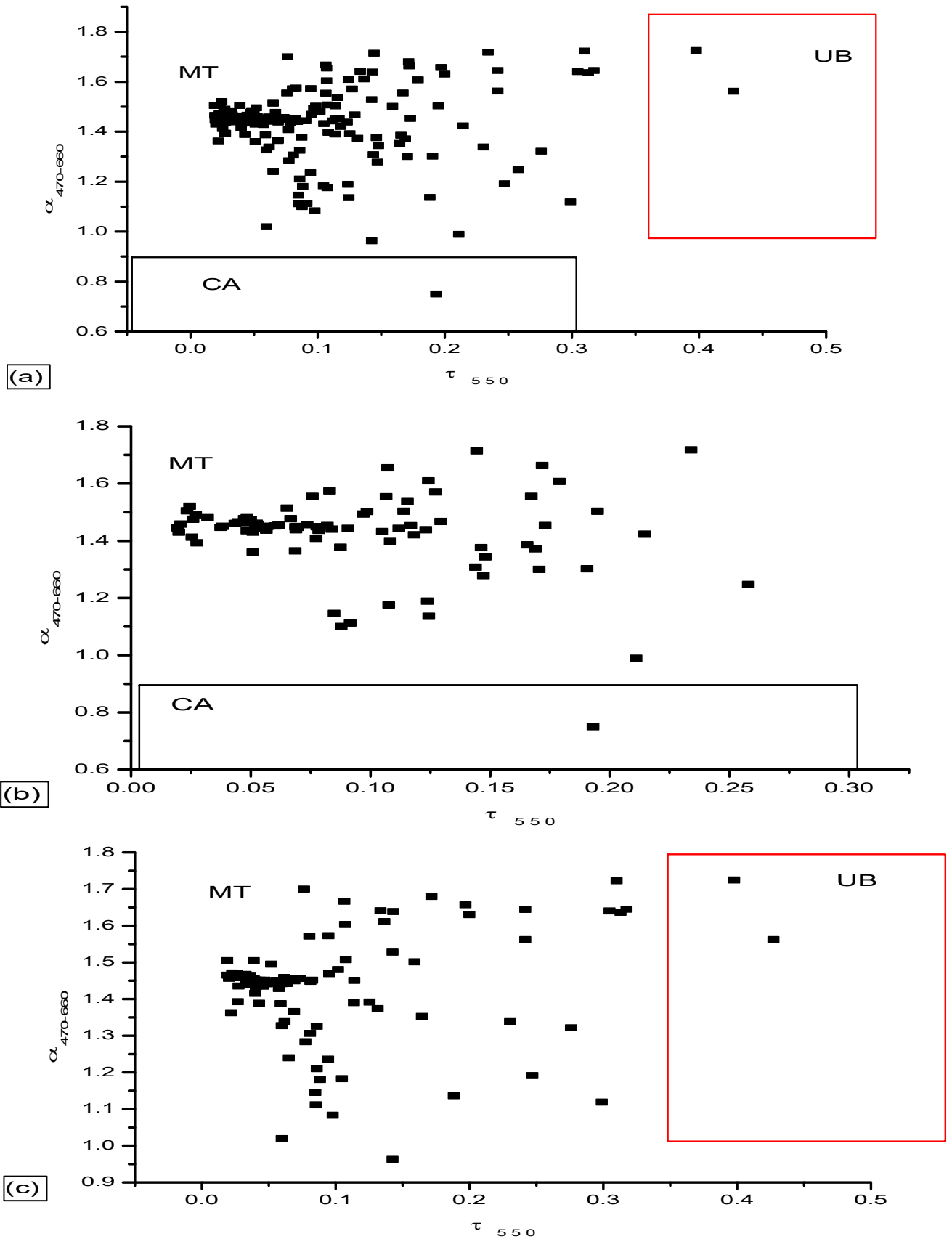


FIG. 7. Scatter plot between τ_{550} and $\alpha_{470-660}$ for determining the diverse aerosol types generally and for each season over Nairobi ((a) Overall; (b) Rainy season; (c) Dry season).

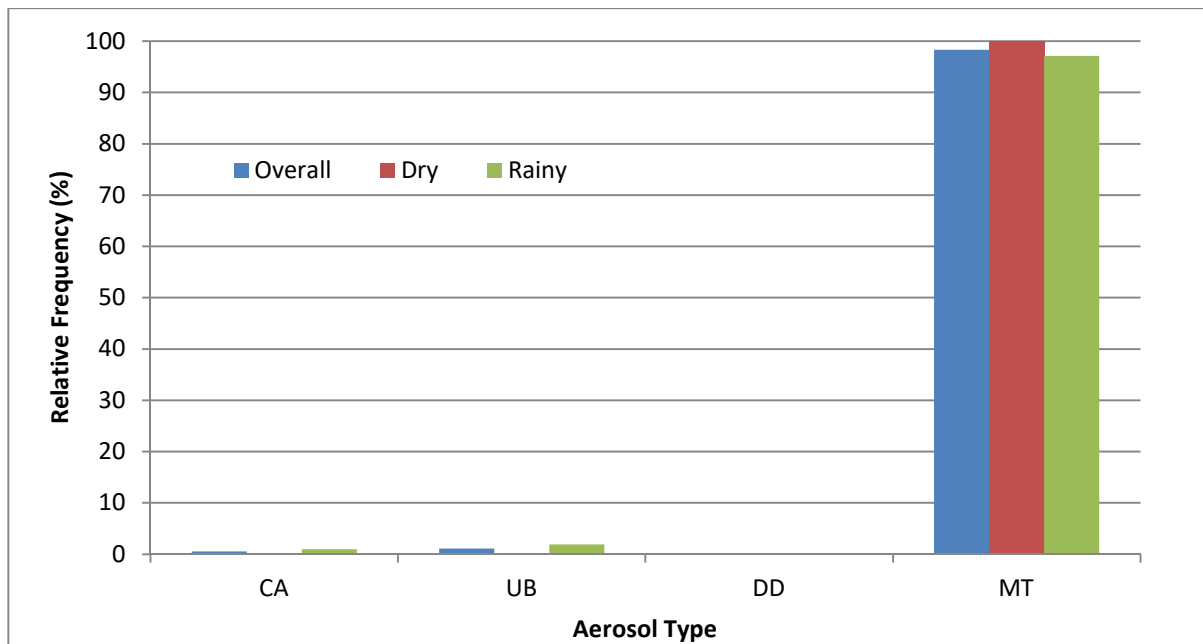


FIG. 8. Percentage contributions of various aerosol types derived from $\alpha_{470-660} - \tau_{550}$ scatter plots for Nairobi.

The same Figure shows that the frequency of aerosol distribution in the station is not dependent on seasonal change. MT aerosols were dominant (100.00% and 97.14%) in both seasons (dry and rainy seasons). Just like in Mbita station, this could be related to a large amount of aerosols that cannot be determined. The results also show that no other type of aerosol was captured during dry season. This is clearly a case of mixing of aerosols of different types to change their identity. During rainy season, different aerosol species were found related to the multiple peaks, which can also be clearly seen in Fig. 7 (c), where MT is the most dominant aerosol type. UB (1.91%) is the second most dominant aerosol type in the station and this may be a result of the use of biomass as fuel around the station. CA (0.95%) is the third most important aerosol in the region. This may be attributed to the south-westerly trade wind which transports the marine aerosol from Atlantic Ocean as well as the impact of rainy season. Lastly, DD aerosol type is not present in this station.

Figs. 9 (a – c) show the scatter plots of τ vs. α over Skukuza. It can be seen from the plots that α shows increasing values with increasing τ , which indicates the presence of fine-mode particles. Also observed is the wide range of values of α (between 1.00 and 1.70) at low τ (≤ 0.35) during rainy season, indicating the

presence of a single type of aerosol under relatively clear atmospheric conditions. Furthermore, the highest number of measurements in the scatter plots for this site is concentrated in the area corresponding to $\alpha_{470-660}$ (1.10 – 1.60) and τ between 0.05 and 0.25, indicating the presence of fine-mode particles. Aerosols from UB with large number of MT are observed in this cluster. However, the area corresponding to MT has a very large number of measurements compared to others. There are also large numbers of measurements concentrated at $\tau < 0.25$ which are characterized by $\alpha_{470-660} > 1.1$. This case corresponds to the occurrence of heavy pollution events of the fine-mode type. The study further notes similar patterns of aerosol distribution during dry and rainy seasons (Figs. 9 (b) and 9 (c)). Only MT was noticed during the rainy season, while UB and MT were present during the dry season.

The relative frequencies of these aerosols are shown in Fig. 10. The MT class was determined as the highest frequency of occurrence (99.36%) in the overall data. This is likely due to the mixture of CA and UB in the atmosphere, as well as the absorption of moisture by these aerosols. The only other aerosol type noticed was the UB class (0.64%), which could be a result of automobile emissions, as well as industrial and biomass burning emissions in the station.

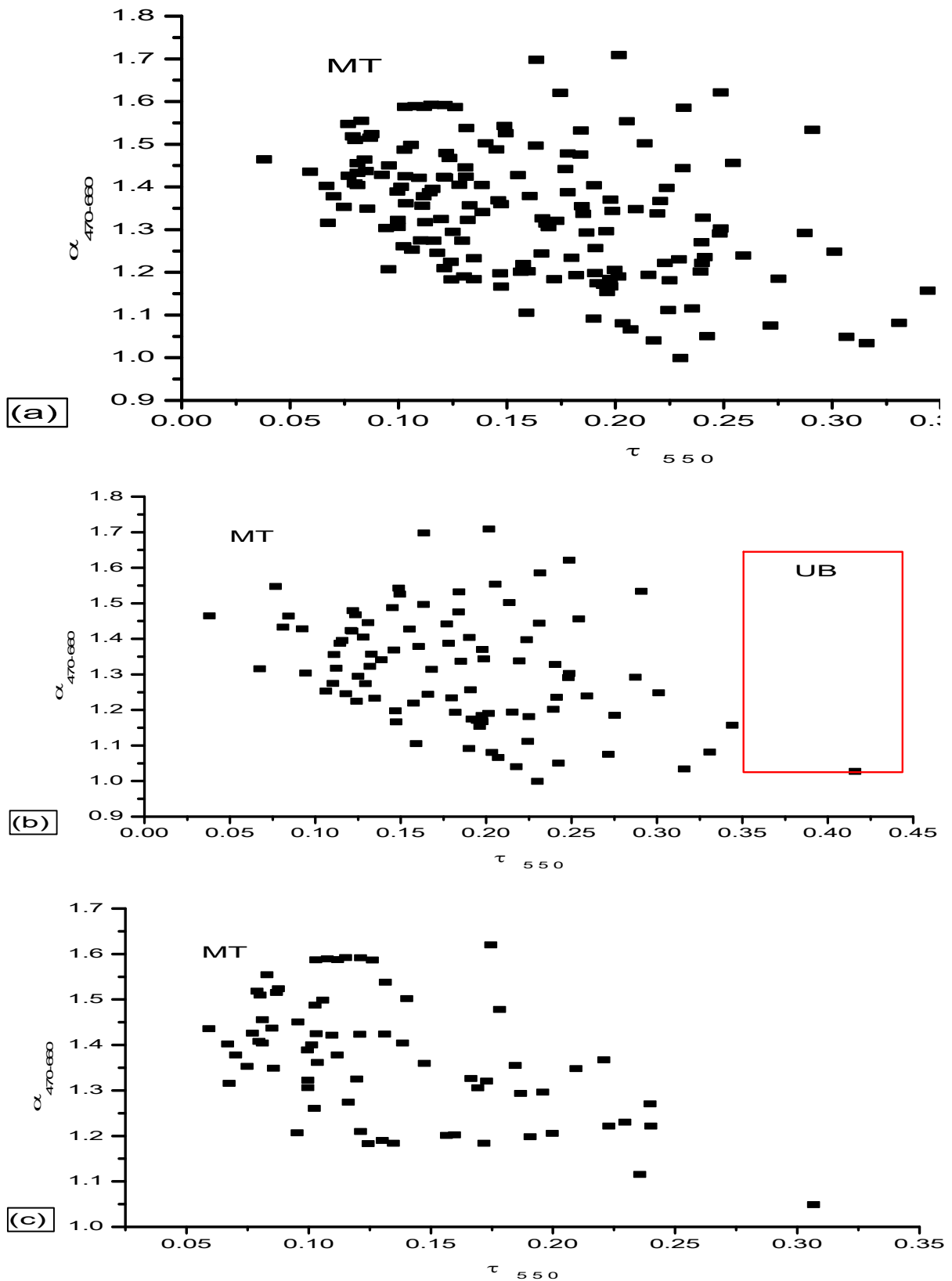


FIG. 9. Scatter plot between τ_{550} and $\alpha_{470-660}$ for determining the diverse aerosol types generally and for each season over Skukuza ((a) Overall; (b) Rainy season; (c) Dry season).

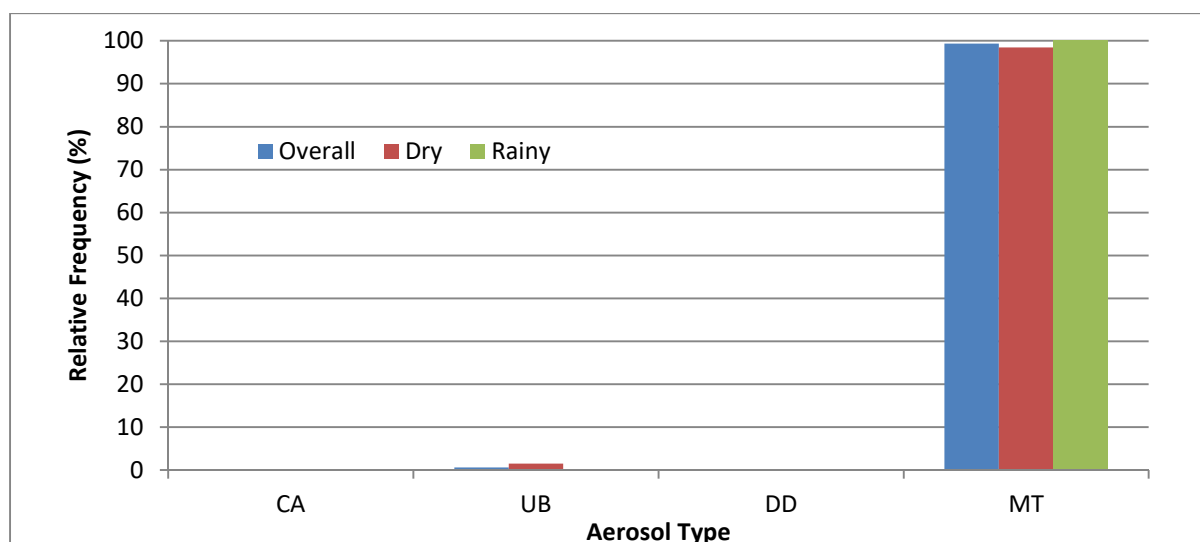


FIG. 10. Percentage contributions of various aerosol types derived from $\alpha_{470-660} - \tau_{550}$ scatter plots for Skukuza.

From the evidence in Figs. 9 (b) and 9 (c), the MT aerosol type is dominant (98.46% and 100.00%) in both seasons (dry and rainy seasons). This could be related to a large amount of aerosols that cannot be determined; i.e., mixed type (MT) which signifies the occurrence of different aerosol species. During both dry and rainy seasons, UB (1.54% and 0.64%) was the second and the last aerosol type discovered at the station.

Using the criteria, the scatter plots of Figs. 11 (a – c) were analyzed. It is clear from the plots that α shows decreasing values with increasing τ , which indicates the presence of coarse-mode particles, mostly dust [46]. This may be connected with the transportation of dust from construction sites and the Sahara desert into the station. Also observed was the wide range of values of α at low τ (≤ 0.8) during rainy season, indicating the presence of different aerosol types under relatively clear atmospheric conditions. Furthermore, the highest number of measurements in the scatter plots for this site is concentrated in the area corresponding to $\alpha_{470-660}$ (0.20 – 1.50) and τ between 0.20 and 1.00, indicating the presence of both anthropogenic and natural particles. Aerosols from CA, DD and UB with large number of MT are observed in this cluster. However, the area corresponding to MT has a slightly larger number of measurements compared to others. There are also large numbers of measurements concentrated at $\tau < 1.20$, which are characterized by $\alpha_{470-660} < 1.40$. This case corresponds to the occurrence of strong dust activities and heavy pollution events of biomass burning and urban

and industrial aerosols. The study further notes similar patterns of aerosol distribution during dry and rainy seasons (Figs. 11 (b) and 11 (c)). Only UB, DD and MT were noticed during the dry season, while CA, DD, UB and MT were present during the rainy season.

The relative frequencies of these aerosols are shown in Fig. 12. The MT class was determined as the highest frequency of occurrence (38.61%) in the overall data. The next highest was the DD class (33.54%) and could be a result of the geographic location of the station. UB is the next most important in this region and it accounts for 23.32% of its aerosol loading. The least important class of aerosol in terms of pollution in this station is UB (2.53%).

With respect to the adopted classification, DD (48.68%) was dominant in the dry season. This is followed by MT and UB with relative frequency values of 32.90% and 18.42%, respectively.

During rainy season, MT (44.44%) was the most dominant aerosol type. This may be attributed to a mix of all or some of the aerosol types in the station, as well as the absorption of water vapour by the aerosols. UB (32.10%) is the second most dominant aerosol type and this may be due to the increase in biomass burning for warming up homes and cooking during the coolness occasioned by the rainy season. DD (18.52%) is the third most important aerosol. This may be attributed to the washing away of dust by rain. Lastly, CA (4.94%) is the least dominant aerosol type.

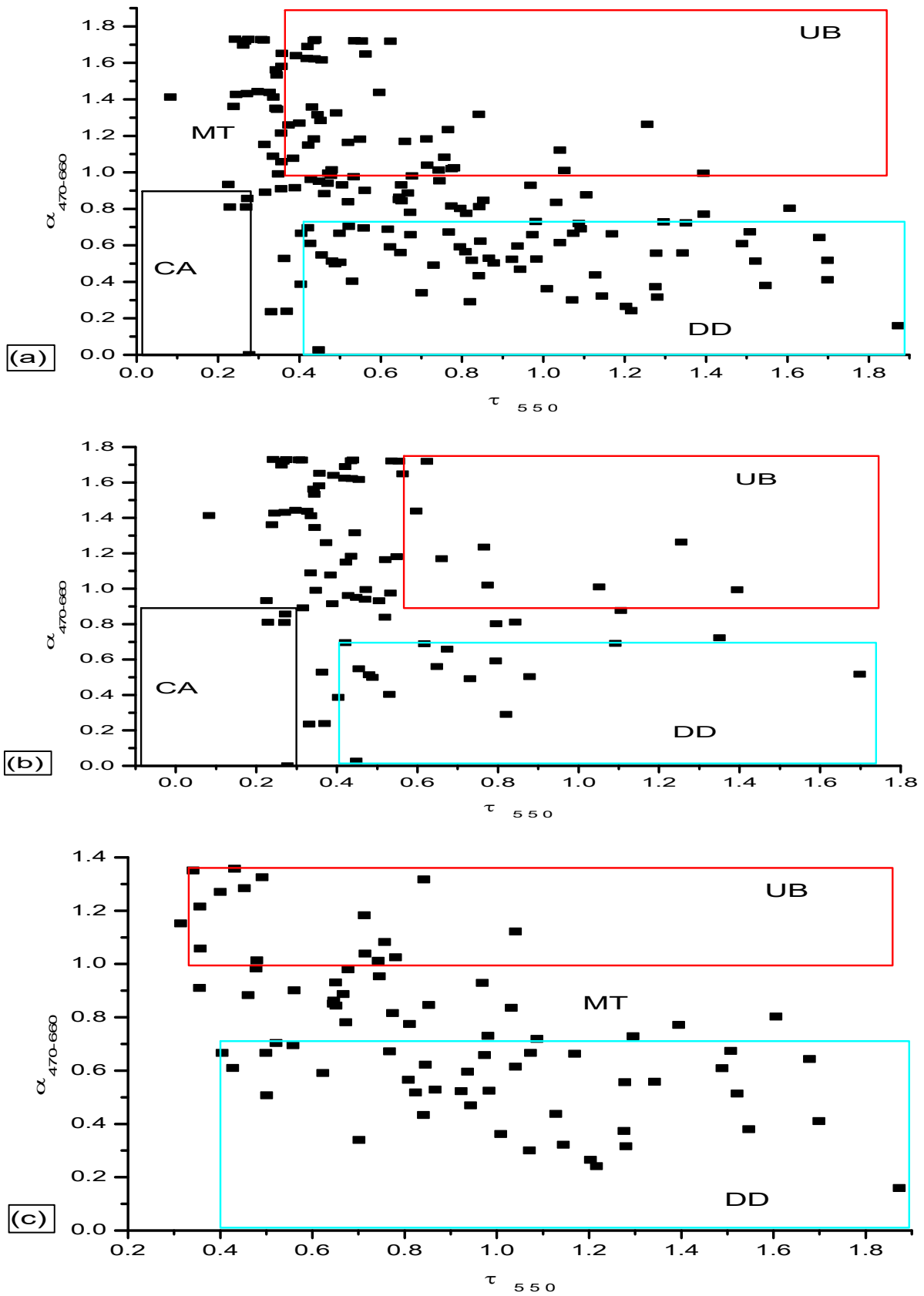


FIG. 11. Scatter plot between τ_{550} and $\alpha_{470-660}$ for determining the diverse aerosol types generally and for each season over Ilorin ((a) Overall; (b) Rainy season; (c) Dry season).

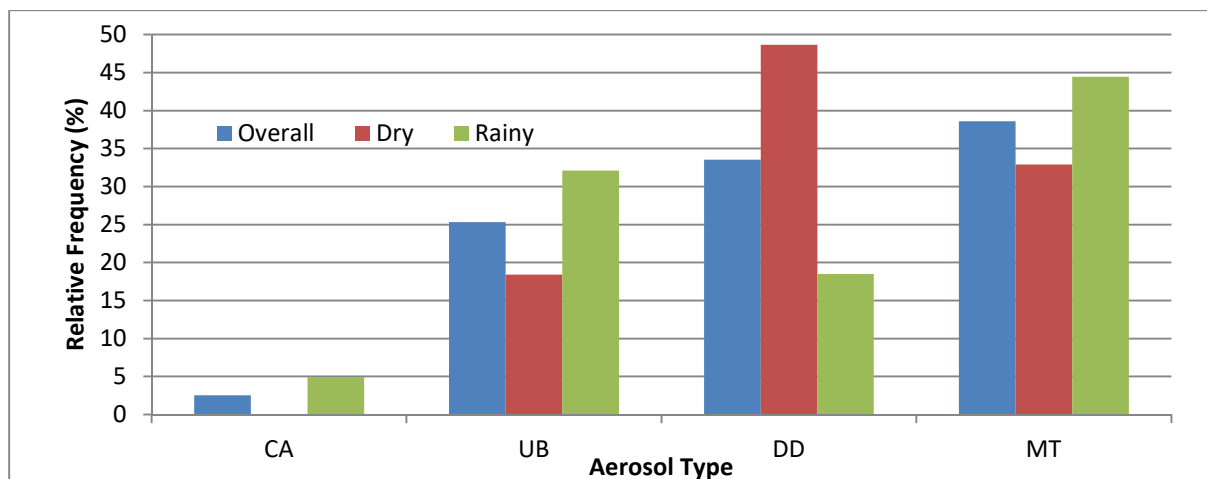


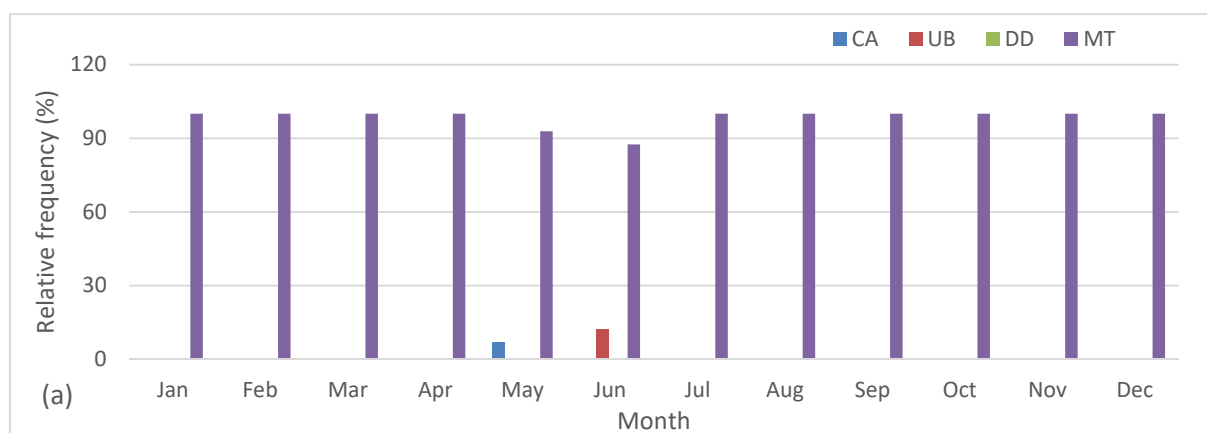
FIG. 12. Percentage contributions of various aerosol types derived from $\alpha_{470-660} - \tau_{550}$ scatter plots for Ilorin.

The result of the analysis of monthly distribution of aerosol types is presented in Fig. 13. The result obtained for Nairobi (Fig. 13 (a)) shows that the aerosols in the station are homogeneous (i.e., predominantly MT). The dominance of MT aerosols suggests that the atmospheric condition in Nairobi will be a blend of the characteristics of all the aggregate aerosols. There are 7.14% of CA in May and 12.50% of UB in June, while the rest are MT. May is expected to be cool because of the presence of CA (scattering atmosphere), while June is expected to be warm because of the presence of UB (heated atmosphere).

Yet again, the result obtained for Skukuza (Fig. 13 (b)) shows that the aerosol in the station is homogeneously MT aside 7.69% of UB in November. MT aerosols' predominance in Skukuza suggests that the atmospheric condition will also be a blend of the characteristics of all the aggregate aerosols. November is expected to

be warmer than other months because of the presence of UB.

In conclusion, results obtained in Ilorin (Fig. 13 (c)) shows that each month has a minimum of two aerosol types. The months of January through April are expected to be cool, because DD is the predominant type of the aerosols found in those months. May, July and November are expected to be warmer, while June, August, September, October and December are expected to be a blend of the characteristics of the predominant aerosols. It was noted that CA's presence was only during some rainy season months, UB and MT's presence cut across both seasons, while DD's presence was noted during the dry season and the early part of the rainy season. UB aerosols are associated with bush and refuse burning as well as exhaust from automobiles and factories. CA can be associated with smaller number of observations as a result of cloud interactions.



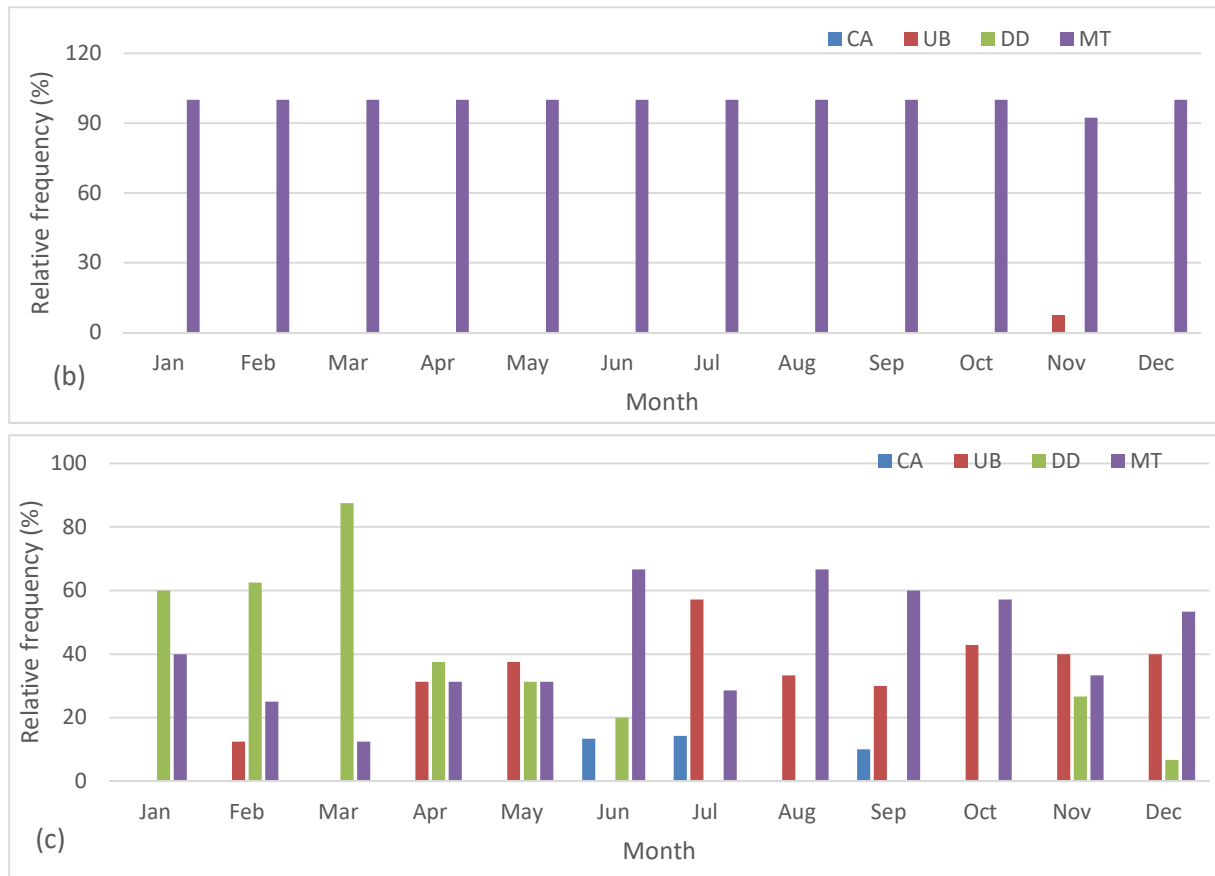


FIG. 13. Percentage contributions of various aerosol types derived from monthly $\alpha_{470-660} - \tau_{550}$ scatter plots over (a) Nairobi, (b) Skukuza and (c) Ilorin.

Conclusion

In this work, an attempt was made to analyze the temporal variation of aerosol optical depth (τ) and Angstrom exponent (α) for the period from February 2000 to July 2015 over Nairobi, Skukuza and Ilorin AERONET stations. Validation of aqua- and terra-MODIS τ with AERONET τ was carried out. The overall validation shows that terra-MODIS τ was better than the aqua-MODIS counterpart in Skukuza because of its lower underestimation when compared with aqua-MODIS. Similarly, aqua-MODIS τ was better than its terra-counterpart at Nairobi and Ilorin stations. The coefficient of determination (R^2) for both validations ranges from 0.690 to 0.935. On seasonal bases, the underestimation during rainy season was better at Nairobi and Skukuza stations, while Ilorin station shows a better overestimation during dry season. The R^2 value for both seasons was found to be between 0.751 and 0.951.

The τ vs. α method employed for the discrimination of aerosols showed an obvious domination of MT aerosols (98.33 %) overall in Nairobi station, while the next highest

contributor comes from the UB aerosol type (1.11 %) and CA (0.56 %) in Nairobi station. The result was similar during dry and rainy seasons. At Skukuza station, the dominant aerosol overall and throughout the dry and rainy seasons was MT aerosols (99.36 %, 98.46 % and 100.00 %, respectively), followed by an insignificant amount of UB aerosols (0.64 %). During dry season, UB aerosols (1.54 %) were the only other aerosol type present. At Ilorin station, MT aerosol type (38.61 %) was dominant overall and DD (33.54 %) was second highest followed by UB (25.32 %) and CA (2.53 %). During the dry season, DD (48.68 %) was the dominant aerosol type, followed by MT (32.90 %) and UB (18.42 %), whereas MT (44.44 %), UB (32.10 %), DD (18.52 %) and CA (4.94 %) were present during the rainy season.

Acknowledgement

The authors wish to thank the Principal Investigators (PIs) of AERONET sites and their staff for establishing and maintaining these sites. In addition, the authors would like to thank the Giovanni team for developing and hosting the MAPSS database and the Web MAPSS user interface.

References

- [1] Ghan, S.J. and Schwartz, S.E., "Aerosol Properties and Processes: A Path from Field and Laboratory Measurements to Global Climate Models", A report by The U.S. Department of Energy strategy for improving the treatment of aerosol properties and processes in global climate models, (2007).
- [2] Mogo, S., Cachorro, V.E., de Frutosa, A. and Rodrigues, A., *J. Environ. Monit.*, 14 (2012) 3174.
- [3] Zhang, J. and Reid, J.S., *J. Geophys. Res. Atmos.*, 111 (22) (2006) 1.
- [4] Li, Z. et al., *J. Geophys. Res. Atmos.*, 112 (2007) D22S07.
- [5] Misra, A., Jayaraman, A. and Ganguly, D., *Aerosol Air Qual. Res.*, 15 (2015) 252.
- [6] Chu, D.A., Kaufman, Y.J., Ichoku, C., Remer, L.A., Tanré, D. and Holben, B.N., *Geophys. Res. Lett.*, 29 (12) (2002) 1.
- [7] Ichoku, C. et al., *Geophys. Res. Lett.*, 29 (12) (2002) 1.
- [8] Levy, R.C. et al., *J. Atmos. Sci.*, 62 (2005) 974.
- [9] Kaufman, Y.J., Tanré, D., Remer, L.A., Vermote, E.F., Chu, A. and Holben, B.N., *J. Geophys. Res.*, 102 (D14) (1997) 17051.
- [10] Levy, R.C., Remer, L.A., Mattoo, S., Vermote, E.F. and Kaufman, Y.J., *J. Geophys. Res. Atmos.*, 112 (13) (2007) 1.
- [11] Hsu, N.C. et al., *IEEE Trans. Geosci. Remote Sens.*, 42 (3) (2004) 23.
- [12] Granados-Munoz, M.J. et al., *Proceedings of the Global Conference on Global Warming 2011, 11 - 14 July, Lisbon, Portugal*, (2011), pp. 1–10.
- [13] Kaufman, Y.J., Tanré, D. and Boucher, O., *Nature*, 419 (2002) 215.
- [14] Remer, L.A. et al., *J. Atmos. Sci.*, 62 (4) (2005) 947.
- [15] Yu, H. et al., *J. Geophys. Res. Atmos.*, 114 (10) (2009) 1.
- [16] Yu, H. et al., *Science (80-.)*, 337 (6094) (2012) 566.
- [17] Bibi, H., Alam, K. and Bibi, S., *Atmos. Res.*, 181 (4) (2016) 106.
- [18] Szkop, A., Pietruczuk, A. and Posyniak, M., *Acta Geophys.*, 64 (6) (2016) 2650.
- [19] Kaskaoutis, D.G., Kambezidis, H.D., Hatzianastassiou, N., Kosmopoulos, P.G. and Badarinath, K.V.S., *Atmos. Chem. Phys. Discuss.*, (2007) 6357.
- [20] Kannemadugu, H.B.S., Varghese, A.O., Mukkara, S.R., Joshi, A.K. and Moharil, S.V., *Aerosol Air Qual. Res.*, 15 (2) (2015) 682.
- [21] Xin, J. et al., *J. Geophys. Res. Atmos.*, 112 (5) (2007) D05203.
- [22] Mbourou, G.N., Bertrand, J.J. and Nicholson, S.E., *J. Appl. Meteorol.*, 36 (1997) 868.
- [23] Makokha, J.W., Angeyo, H.K. and Muthama, J.N., *Int. J. Sci. Technoledge*, 5 (3) (2017) 166.
- [24] Levy, R.C., Remer, L.A. and Dubovik, O., *J. Geophys. Res. Atmos.*, 112 (13) (2007).
- [25] Laakso, L. et al., *Atmos. Chem. Phys.*, 12 (2012) 1847.
- [26] Tiwari, S. and Singh, A.K., *Aerosol Air Qual. Res.*, 13 (2) (2013) 627.
- [27] Ichoku, L.R.C., Kaufman, Y.J. and Remer, L.A., *Adv. Sp. Res.*, 34 (2004) 820.
- [28] Holben, B.N., Eck, T.F., Slutsker, I., Tanre', D., Buis, J.P., Setzer, A., Vermote, E., Reagan, J.A., Kaufman, Y.J., Nakajima, T., Lavenu, F., Jankowiak, I. and Smirnov, A., *Remote Sens. Environ.*, 66 (1998) 1.
- [29] Al-Salihi, A.M., *Arab. J. Geosci.*, 11 (633) (2018) 1.
- [30] Petrenko, M., Ichoku, C. and Leptoukh, G., *Atmos. Meas. Tech.*, 5 (2012) 913.
- [31] Boersma, K.F. and de Vroom, J.P., *J. Geophys. Res. Atmos.*, 111 (20) (2006) 1.
- [32] Kumar, K.R. et al., *Atmos. Environ.*, 95 (2014) 400.
- [33] Tijjani, B.I., Aliyu, A. and Sha'aibu, F., *Open J. Appl. Sci.*, 4 (2014) 399.
- [34] Tan, F., Lim, H.S., Abdullah, K., Yoon, T.L. and Holben, B.N., *Atmos. Pollut. Res.*, 6 (2015) 682.

- [35] Eck, T.F. *et al.*, *J. Geophys. Res. D Atmos.*, 104 (1) (1999) 31, 333.
- [36] Tijjani, B.I. and Akpootu, D.O., *Int. J. Res. Rev. Pharm. Appl. Sci.*, 2 (6) (2012) 1128.
- [37] He, L., Wang, L., Lin, A., Zhang, M., Bilal, M. and Tao, M., *Remote Sens.*, 9 (746) (2017) 1.
- [38] Anuforom, A.C., Akeh, L.E., Okeke, P.N. and Opara, F.E., *Atmos. Environ.*, 41 (7) (2007) 1550.
- [39] Toledano, C. *et al.*, *Q. J. R. Meteorol. Soc.*, 133 (2007) 795.
- [40] Balarabe, M., Abdullah, K. and Nawawi, M., *Atmosphere (Basel)*, 6 (2015) 1462.
- [41] Ogunjobi, K., Ajayi, V., Balogun, I., Omotosho, J. and He, Z., *Theor. Appl. Climatol.*, 93 (1–2) (2008) 91.
- [42] Sharma, M., Kaskaoutis, D.G., Singh, R.P. and Singh, S., *Aerosol Air Qual. Res.*, 14 (2014) 608.
- [43] Kumar, K.R., Sivakumar, V., Reddy, R.R., Gopal, K.R. and Adesina, A.J., *Aerosol Air Qual. Res.*, 14 (2014) 108.
- [44] Verma, S., Prakash, D., Ricaud, P., Payra, S., Attié, J. and Soni, M., *Aerosol Air Qual. Res.*, 15 (2015) 985.
- [45] Tariq, S., Zia, U.-H. and Ali, M., *Asia-Pacific J. Atmos. Sci.*, 52 (1) (2016) 25.
- [46] Ogunjobi, K.O., He, Z., Kim, K.W. and Kim, Y.J., *Atmos. Environ.*, 38 (9) (2004) 1313.

Authors Index

A. A. Ajayi.....	191
A. A. Obeidat	201
A. B. Alabi.....	191
A. B. Ogunremi	237
A. Shaer.....	247
B. I. Tijjani.....	269
D. R. Adhikari.....	241
H. A. Abu-Ghazleh	201
H. P. Lamichhane	241
H. T. Sulu	269
I. S. Akinsola	191
K. A. Adewoyin	237
K. A. Khasawneh.....	201
K. S. Adedayo	191
Khalifeh AbuSaleem.....	255
M. Abu-Kharma	223
M. Ali.....	247
M. Al-Kofahi	209
M. Al-Shorman	209
M. Elsaid	247
M. M. Al-Ali.....	201
M. M. Bube.....	269
Mahmoud H. Saleh	223
O. A. Babalola.....	191
Q. I. Mohaidat	209
R. Aliyu.....	269
R. M. Al-Salman.	201
S. B. Sharafa	269
S. K. Adhikari	241
T. H. Darma	269
W. J. Kadhem.....	223
Z. M. Elimat.....	223

Subject Index

AERONET	269
Aerosol optical depth	269
Angstrom exponent	269
Annealing	191
Cadmium sulphide.....	191
CIA.....	223
Collision-induced spectroscopy	223
Consumption	237
Discrimination.....	269
Effective dose.....	237
Energy band gap.....	241
Environment mapping.....	209
Exact diagonalization method	247
Gaussian quantum dot	247
H ₂	223
Imported foodstuff.....	237
Infrared absorption	223
IR spectra	223
JRTR	255
Lattice parameter.....	241
Lead chalcogenides	241
Line shape functions.....	223
Liquid density.....	201
Magnetic field	247
Magnetic susceptibility	247
Magnetization.....	247
Molecular dynamics	201
Monitoring.....	237
Nanoparticle size	241
OPLS-AA	201
Optical properties	191
Radionuclides.....	237
Reactor commissioning.....	255
Reactor safety.....	255
Research reactor	255
Roto-vibrational state	223
Second overtone band	223
Simulation	209
Spray pyrolysis.....	191
Surface tension.....	201
Terra and Aqua MODIS	269
Thin film.....	191
TraPPE-UN	201
Unidirectional ultrasonic pulses	209
Validation.....	269

المراجع: يجب طباعة المراجع بأسطر مزدوجة ومرقمة حسب تسلسلها في النص. وتكتب المراجع في النص بين قوسين مربعين. ويتم اعتماد اختصارات الدوريات حسب نظام Wordlist of Scientific Reviewers.

الجدول: تعطى الجداول أرقاماً متسلسلة يشار إليها في النص. ويجب طباعة كل جدول على صفحة منفصلة مع عنوان فوق الجدول. أما الحواشي التفسيرية، التي يشار إليها بحرف فوقي، فتكتب أسفل الجدول.

الرسوم التوضيحية: يتم ترقيم الأشكال والرسومات والرسومات البيانية (المخططات) والصور، بصورة متسلسلة كما وردت في النص.

تقبل الرسوم التوضيحية المستخرجة من الحاسوب والصور الرقمية ذات النوعية الجيدة بالأبيض والأسود، على أن تكون أصيلة وليست نسخة عنها، وكل منها على ورقة منفصلة ومعرفة برقمها بالمقابل. ويجب تزويد المجلة بالرسومات بحجمها الأصلي بحيث لا تحتاج إلى معالجة لاحقة، وألا تقل الحروف عن الحجم 8 من نوع Times New Roman، وألا تقل سماكة الخطوط عن 0.5 وكتافة متجانسة. ويجب إزالة جميع الألوان من الرسومات ما عدا تلك التي ستنشر ملونة. وفي حالة إرسال الرسومات بصورة رقمية، يجب أن تتوافق مع متطلبات الحد الأدنى من التمايز (1200 dpi Resolution) لرسومات الأبيض والأسود الخطية، و 600 dpi للرسومات باللون الرمادي، و 300 dpi للرسومات الملونة. ويجب تخزين جميع ملفات الرسومات على شكل (jpg)، وأن ترسل الرسوم التوضيحية بالحجم الفعلي الذي سيظهر في المجلة. وسواء أرسل المخطوط بالبريد أو عن طريق الشبكة (Online)، يجب إرسال نسخة ورقية أصلية ذات نوعية جيدة للرسومات التوضيحية.

مواد إضافية: تشجع المجلة الباحثين على إرفاق جميع المواد الإضافية التي يمكن أن تسهل عملية التحكيم. وتشمل المواد الإضافية أي اشتقاقات رياضية مفصلة لا تظهر في المخطوط.

المخطوط المنقح (المعدل) والأقراص المدمجة: بعد قبول البحث للنشر وإجراء جميع التعديلات المطلوبة، فعلى الباحثين تقديم نسخة أصلية ونسخة أخرى مطابقة للأصلية مطبوعة بأسطر مزدوجة، وكذلك تقديم نسخة إلكترونية تحتوي على المخطوط كاملاً مكتوباً على Microsoft Word for Windows 2000 أو ما هو استجد منه. ويجب إرفاق الأشكال الأصلية مع المخطوط النهائي المعدل حتى لو تم تقديم الأشكال إلكترونياً. وتخزن جميع ملفات الرسومات على شكل (jpg)، وتقدم جميع الرسومات التوضيحية بالحجم الحقيقي الذي ستظهر به في المجلة. ويجب إرفاق قائمة ببرامج الحاسوب التي استعملت في كتابة النص، وأسماء الملفات على قرص مدمج، حيث يعلم القرص بالاسم الأخير للباحث، وبالرقم المرجعي للمخطوط للمراسلة، وعنوان المقالة، والتاريخ. ويحفظ في مغلف واقٍ.

حقوق الطبع

يُشكّل تقديم مخطوط البحث للمجلة اعترافاً صريحاً من الباحثين بأن مخطوط البحث لم يُنشر ولم يُقدّم للنشر لدى أي جهة أخرى كانت وبأي صيغة ورقية أو إلكترونية أو غيرها. ويُشترط على الباحثين ملء نموذج يُنصّ على نقل حقوق الطبع لتصبح ملكاً لجامعة اليرموك قبل الموافقة على نشر المخطوط. ويقوم رئيس التحرير بتزويد الباحثين بإنموذج نقل حقوق الطبع مع النسخة المُرسلة للتتقيح. كما ويُمنع إعادة إنتاج أي جزء من الأعمال المنشورة في المجلة من دون إذن خطّي مُسبق من رئيس التحرير.

إخلاء المسؤولية

إن ما ورد في هذه المجلة يعبر عن آراء المؤلفين، ولا يعكس بالضرورة آراء هيئة التحرير أو الجامعة أو سياسة اللجنة العليا للبحث العلمي أو وزارة التعليم العالي والبحث العلمي. ولا يتحمل ناشر المجلة أي تبعات مادية أو معنوية أو مسؤوليات عن استعمال المعلومات المنشورة في المجلة أو سوء استعمالها.

الفهرسة: المجلة مفهرسة في:

	Emerging Sources Citation Index (ESCI)	
---	---	---

المجلة الأردنية للفيزياء هي مجلة بحوث علمية عالمية متخصصة مُحكمة تصدر بدعم من صندوق دعم البحث العلمي، وزارة التعليم العالي والبحث العلمي، عمان، الأردن. وتقوم بنشر المجلة عمادة البحث العلمي والدراسات العليا في جامعة اليرموك، إربد، الأردن. وتنتشر البحوث العلمية الأصيلة، إضافة إلى المراسلات القصيرة Short Communications، والملاحظات الفنية Technical Notes، والمقالات الخاصة Feature Articles، ومقالات المراجعة Review Articles، في مجالات الفيزياء النظرية والتجريبية، باللغتين العربية والإنجليزية.

تقديم مخطوط البحث

تقدم البحوث عن طريق إرسالها إلى البريد الإلكتروني : jjp@yu.edu.jo

تقديم المخطوطات إلكترونياً: اتبع التعليمات في موقع المجلة على الشبكة العنكبوتية.

ويجري تحكيم البحوث الأصيلة والمراسلات القصيرة والملاحظات الفنية من جانب مُحكمين اثنين في الأقل من ذوي الاختصاص والخبرة. وتُشجّع المجلة الباحثين على اقتراح أسماء المحكمين. أما نشر المقالات الخاصة في المجالات الفيزيائية النشطة، فيتم بدعوة من هيئة التحرير، ويُشار إليها كذلك عند النشر. ويُطلب من كاتب المقال الخاص تقديم تقرير واضح يتسم بالدقة والإيجاز عن مجال البحث تمهيداً للمقال. وتنتشر المجلة أيضاً مقالات المراجعة في الحقول الفيزيائية النشطة سريعة التغير، وتشجّع كاتبي مقالات المراجعة أو مُستكثبيها على إرسال مقترح من صفحتين إلى رئيس التحرير. ويرفّق مع البحث المكتوب باللغة العربية ملخص (Abstract) وكلمات دالة (Keywords) باللغة الإنجليزية.

ترتيب مخطوط البحث

يجب أن تتم طباعة مخطوط البحث ببنت 12 نوعه Times New Roman، وبسطر مزدوج، على وجه واحد من ورق A4 (21.6 × 27.9 سم) مع حواشي 3.71 سم، باستخدام معالج كلمات ميكروسوفت وورد 2000 أو ما استُجد منه. ويجري تنظيم أجزاء المخطوط وفق الترتيب التالي: صفحة العنوان، الملخص، رموز التصنيف (PACS)، المقدمة، طرق البحث، النتائج، المناقشة، الخلاصة، الشكر والعرفان، المراجع، الجداول، قائمة بدليل الأشكال والصور والإيضاحات، ثم الأشكال والصور والإيضاحات. وتُكتب العناوين الرئيسية بخط غامق، بينما تُكتب العناوين الفرعية بخط مائل.

صفحة العنوان: وتشمل عنوان المقالة، أسماء الباحثين الكاملة وعناوين العمل كاملة. ويكتب الباحث المسؤول عن المراسلات اسمه مشاراً إليه بنجمة، والبريد الإلكتروني الخاص به. ويجب أن يكون عنوان المقالة موجزاً وواضحاً ومعبراً عن فحوى (محتوى) المخطوط، وذلك لأهمية هذا العنوان لأغراض استرجاع المعلومات.

الملخص: المطلوب كتابة فقرة واحدة لا تزيد على مائتي كلمة، موضحة هدف البحث، والمنهج المتبع فيه والنتائج وأهم ما توصل إليه الباحثون.

الكلمات الدالة: يجب أن يلي الملخص قائمة من 4-6 كلمات دالة تعبر عن المحتوى الدقيق للمخطوط لأغراض الفهرسة.

PACS: يجب إرفاق الرموز التصنيفية، وهي متوفرة في الموقع <http://www.aip.org/pacs/pacs06/pacs06-toc.html>.

المقدمة: يجب أن توضّح الهدف من الدراسة وعلاقتها بالأعمال السابقة في المجال، لا أن تكون مراجعة مكثفة لما نشر (لا تزيد المقدمة عن صفحة ونصف الصفحة مطبوعة).

طرائق البحث (التجريبية / النظرية): يجب أن تكون هذه الطرائق موضحة بتفصيل كاف لإتاحة إعادة إجرائها بكفاءة، ولكن باختصار مناسب، حتى لا تكون تكراراً للطرائق المنشورة سابقاً.

النتائج: يستحسن عرض النتائج على صورة جداول وأشكال حيثما أمكن، مع شرح قليل في النص ومن دون مناقشة تفصيلية.

المناقشة: يجب أن تكون موجزة وتركز على تفسير النتائج.

الاستنتاج: يجب أن يكون وصفاً موجزاً لأهم ما توصلت إليه الدراسة ولا يزيد عن صفحة مطبوعة واحدة.

الشكر والعرفان: الشكر والإشارة إلى مصدر المنح والدعم المالي يكتبان في فقرة واحدة تسبق المراجع مباشرة.

Jordan Journal of

PHYSICSAn International Peer-Reviewed Research Journal issued by the
Support of the Scientific Research Support Fund

Published by the Deanship of Research & Graduate Studies, Yarmouk University, Irbid, Jordan

Name: الأسم:
 Specialty: التخصص:
 Address: العنوان:
 P.O. Box: صندوق البريد:
 City & Postal Code: المدينة/الرمز البريدي:
 Country: الدولة:
 Phone: رقم الهاتف:
 Fax No: رقم الفاكس:
 E-mail: البريد الإلكتروني:
 No. of Subscription: عدد الاشتراكات:
 Method of Payment: طريقة الدفع:
 Amount Enclosed: المبلغ المرفق:
 Signature: التوقيع:

Cheques should be paid to Deanship of Research and Graduate Studies - Yarmouk University.

I would like to subscribe to the Journal
For

- One Year
 Two Years
 Three Years

One Year Subscription Rates

	Inside Jordan	Outside Jordan
Individuals	JD 8	€ 40
Students	JD 4	€ 20
Institutions	JD 12	€ 60

Correspondence**Subscriptions and Sales:**

Prof. Ibrahim O. Abu Al-Jarayesh
 Deanship of Research and Graduate Studies
 Yarmouk University
 Irbid – Jordan
Telephone: 00 962 2 711111 Ext. 2075
Fax No.: 00 962 2 7211121



جامعة اليرموك



المملكة الأردنية الهاشمية

المجلة الأردنية

للفيزياء

مجلة بحوث علمية عالمية متخصصة محكمة
تصدر بدعم من صندوق دعم البحث العلمي

المجلة الأردنية
للفيزياء
مجلة بحوث علمية عالمية محكمة

المجلد (12)، العدد (3)، كانون أول 2019م / جمادى الأولى 1441هـ

المجلة الأردنية للفيزياء: مجلة علمية عالمية متخصصة محكمة تصدر بدعم من صندوق دعم البحث العلمي، عمان، الأردن، وتصدر عن عمادة البحث العلمي والدراسات العليا، جامعة اليرموك، إربد، الأردن.

رئيس التحرير:

ابراهيم عثمان أبو الجرايش

قسم الفيزياء، جامعة اليرموك، إربد، الأردن.

ijaraysh@yu.edu.jo

هيئة التحرير:

نبيل يوسف أيوب

رئيس الجامعة الأمريكية في مادبا، مادبا، الأردن.

nabil.ayoub@gju.edu.jo

جميل محمود خليفة

قسم الفيزياء، الجامعة الأردنية، عمان، الأردن.

jkalifa@ju.edu.jo

سامي حسين محمود

قسم الفيزياء، الجامعة الأردنية، عمان، الأردن.

s.mahmood@ju.edu.jo

مرwan سليمان موسى

قسم الفيزياء، جامعة مؤتة، الكرك، الأردن.

mmousa@mutah.edu.jo

محمد خالد الصغير

قسم الفيزياء، الجامعة الهاشمية، الزرقاء، الأردن.

msugh@hu.edu.jo

عبد المجيد الياسين

قسم الفيزياء، جامعة اليرموك، إربد، الأردن.

alyassin@yu.edu.jo

محمد العمري

قسم الفيزياء، جامعة العلوم والتكنولوجيا، إربد، الأردن.

alakmoh@just.edu.jo

إبراهيم البصول

قسم الفيزياء، جامعة آل البيت، المفرق، الأردن.

Ibrahimbsoul@yahoo.com

سكرتير التحرير: مجدي الشناق

ترسل البحوث إلى العنوان التالي:

الأستاذ الدكتور إبراهيم عثمان أبو الجرايش
رئيس تحرير المجلة الأردنية للفيزياء
عمادة البحث العلمي والدراسات العليا، جامعة اليرموك
إربد، الأردن

هاتف 00 962 2 7211111 فرعي 2075

E-mail: jjp@yu.edu.jo Website: <http://Journals.yu.edu.jo/jjp>